Development of Benzodithiophene (BDT)-Based Wide Bandgap Donor-Acceptor (D-A) Polymers Containing Novel Thiophene and Benzene Acceptor Building Blocks for Organic Solar Cells

by

Scott Flynn

A thesis

presented to the University of Waterloo

in fulfillment of the

thesis requirement for the degree of

Master of Applied Science

in

Chemical Engineering (Nanotechnology)

Waterloo Ontario, Canada, 2023

© Scott Flynn 2023

Author's Declaration

I hereby declare that I am the sole author of this thesis. This is a true copy of the thesis, including any required final revisions, as accepted by my examiners.

I understand that my thesis may be made electronically available to the public.

Abstract

Organic solar cells (OSCs) are an emerging renewable energy technology with advantages of low cost, flexibility, lightweight, and easy processability. High performing OSCs often consist of a wide bandgap polymer donor and a small molecule non-fullerene acceptor (NFA) for complementary absorption. These materials are usually mixed in solution to form a bulk heterojunction (BHJ) structure to achieve efficient charge transfer. Currently, leading materials can reach a power conversion efficiency (PCE) greater than 18 %. However, several challenges remain before OSCs can be commercially viable including further enhancement of the PCE, long-term stability, large area device fabrication, low-cost materials development, and environmentally friendly synthesis. It is critical to target solution-processable polymer donors, with well-matched opto-electronic properties and morphological compatibility with NFAs through effective side chain engineering for further progress in this field.

This thesis work targets low-cost polymer donor materials through relatively easy synthesis routes and low-cost starting materials. Side chains will be selected to target good solubility, low E_{HOMO} levels (to match with high performance NFAs like Y6), and good morphology to achieve high performing polymer donor materials. In this work, several novel donor polymers are developed, which have a donor-acceptor (D-A) structure. D-A polymer building blocks have become increasingly important as donor materials in OSCs since the energy levels and bandgaps are easily tunable via intramolecular charge transfer. Four novel series of polymers: ethynyl thiophene-benzodithiophene (BDT), triazole thiophene-BDT, tetrafluorobenzene-BDT, and acetal thiophene-BDT, with a variety of electron withdrawing group (EWG) side chains were designed, synthesized, and characterized as wide bandgap polymer donors for OSC applications.

An ethynyl series of polymers were designed with the goal of extending the conjugation into the side chain. This can effectively polarize the polymers and increase the exciton lifetime, resulting in improved performance. The ethynyl series included the following side chains: a trimethyl silyl group (PSETBDT), an unsubstituted benzene ring (PBETBDT), and an alkyloxime-substituted benzene ring (POBETBDT). The solar cell devices based on PSETBDT:Y6 and PSETBDT:IT-4F had a PCE of 1.44 and 0.77 %, respectively. The poor performance was attributed to low, unbalanced mobility, and a high polydispersity index (PDI), indicating that cross-linking occurred. Solubility issues and low molecular weight were experienced with polymer

PBETBDT; therefore, this polymer was only preliminarily tested for opto-electrochemical measurements. POBETBDT had a PCE of 3.65 % with Y6, while only achieving an open circuit voltage (V_{oc}) of 0.71 and a fill factor (FF) of 0.33. Low mobility and the bulky side chain are potential issues with this material. Future work will look to assess the surface roughness and domain size of these polymers using atomic force microscopy (AFM) to further assess morphological issues.

Similarly, a triazole series of polymers were designed with the goal of extending the conjugation into the side chain. The triazole series involved converting an aldehyde to a triazole ring, which was then substituted at the middle nitrogen with an alkyl chain (PTTBDT), and a carbamate chain (PCTBDT). Polymer PTTBDT achieved a PCE of 5.00 % with Y6, while PCTBDT only achieved 3.29 % due to lower short circuit current density (J_{sc}), V_{oc}, and FF. Both polymers suffered from low mobility, while PCTBDT had exceptionally low hole mobility (10^{-7} $cm^2V^{-1}s^{-1}$). DFT calculations indicated these polymers suffer from backbone and side chain twisting, which can negatively affect the charge transfer. Additionally, PCTBDT has a thermally removable side chain that could result in extensive hole trapping, which would limit charge extraction. Future work will look to assess the surface roughness via AFM and further optimize PTTBDT:Y6 devices by altering the donor:acceptor (D:A) ratio to improve the charge mobility.

A tetrafluorobenzene-BDT (PFBBDT) polymer was designed to improve upon the E_{HOMO} and co-planarity characteristics of an unsubstituted benzene-BDT polymer by adding fluorine atoms as an electron withdrawing group (EWG). This can help energy level matching with NFAs such as Y6 and allow for good charge transfer. PFBBDT achieved a PCE of 5.14 %; however, the performance was limited by low molecular weight and strong lamellar stacking interactions. The latter is thought to cause potential aggregation in the active layer and contribute to the low and unbalanced mobility observed. The lamellar stacking indicates this material has potential for future transistor applications.

Previously, synthesis of a polymer based on BDT and a formaldehyde-substituted thiophene was attempted by our group but was unsuccessful. A polymer (PATBDT) was designed with an acetal side chain substituted thiophene to facilitate an acid-catalyzed post polymerization modification to obtain a soluble formaldehyde-substituted thiophene-BDT polymer (PXTBDT).

DFT calculations indicated that both these materials had potential for good organic photovoltaic performance (OPV). When PATBDT was paired with Y6, a PCE of 8.20 % was achieved. Low electron mobility resulted in unbalanced charge transfer and low FF for this material. PXTBDT had a quite low E_{HOMO} of -5.67 eV but still worked well with Y6, achieving a better PCE of 9.97 %, mainly due to higher V_{oc} and FF. The low FF of these materials leaves room for process optimization to improve performance. Furthermore, future work will explore other D units, such as bithiophene and thienothiophene, to pair with acetal-protected aldehyde A units to investigate if this simple chemistry can produce any other high performing materials.

Acknowledgements

I would like to thank my supervisor, Dr. Yuning Li, for providing me with the opportunity to pursue my M.A.Sc. at the University of Waterloo in the Printable Electronic Materials Laboratory. His experience and knowledge have been very helpful throughout my research project. His guidance and advice have allowed me to develop my research skills and has provided me with a foundation for problem solving that I will be able to apply in my future career. I am incredibly grateful for his support throughout my degree.

I would also like to thank my colleague, Yi Yuan, for his support and guidance in synthesis, characterization, and testing of my organic solar cell materials. He provided my initial training and continual support throughout my degree. I also want to thank Yi for his assistance with material testing including PL and XRD.

Furthermore, I would like to acknowledge my other colleagues including Zhe, Ravinder, Daniel, Andrew, Haoyu, Samala, Naixin, Jenner, Dr. Jeon, John, Yonglin, Dr. Ali Reza, Yaoyao, Belle, Merlan, Zhaoyi, Xiguang, Yvonne, Guoliang, and Fengqing. They have assisted with my research experiments and analysis and have also provided friendship and support throughout my time at the University of Waterloo.

I would like to thank my committee members, Dr. Xianshe Feng and Dr. Eric Croiset , for taking the time to review this work and participate in my oral defence.

I would also like to acknowledge that the Natural Sciences and Engineering Research Council (NSERC) supported this research, and the NSERC Green Electronics Network (GreEN). Furthermore, I have received financial support from the NSERC CGS M award, the Queen Elizabeth II Graduate Scholarship in Science and Technology (QEII-GSST) award, Dr. Li, and the University of Waterloo, to which I am very grateful.

Finally, I would like to thank my friends and family who have provided me with the support and motivation I needed to complete my degree. I would especially like to thank my parents, Mary and Dave Flynn, for their continued emotional and financial support throughout my education.

Table of Contents

Author's Declaration ... ii
Abstract ... iii
Acknowledgements ... vi
List of Figures ... x
List of Tables ... xiii
List of Schemes ... xv
List of Abbreviations ... xvi
List of Symbols ... xviii
Chapter 1: Introduction ... 1
1.1 Overview of Organic Solar Cells ... 1
1.2 The Development of the Bulk Heterojunction Solar Cell ... 3
1.2.1 Conventional and Inverted BHJ Structures ... 4
1.2.2 Working Principal of BHJ Active Layer ... 4
1.3 OSC Performance Metrics ... 6
1.4 Brief History of Acceptor and Donor Materials for OSCs ... 8
1.4.1 Acceptor Materials ... 8
1.4.2 Donor Materials ... 10
1.5 Design Principles of Polymer Donors ... 12
1.5.1 Light Absorption ... 12
1.5.2 Charge Mobility ... 12
1.5.3 Energy Levels ... 12
1.5.4 Solubility ... 13
1.5.5 Morphology ... 13
1.6 Characterization Methods for OSC Materials and Devices ... 14
1.6.1 Chemical Structure ... 14
1.6.2 Physical Properties ... 15
1.6.3 Opto-Electrochemical Properties ... 16
1.6.4 Morphological Properties ... 17
1.7 Thesis Structure and Objectives ... 20
Chapter 2: Development of BDT-Based Donor Polymers Containing Novel Thiophene Comonomers with Ethynyl Side Chains ... 22
2.1 Introduction ... 22
2.2 Polymer Structure Design ... 24
2.2.1 Density Functional Theory (DFT) Simulations ... 24

2.2.2 Synthesis Scheme 27
2.3 Physical Properties 28
2.4 Opto-Electrochemical Properties 31
2.5 OPV Performance and Charge Mobility 38
2.6 Crystallinity 45
2.7 Summary and Future Direction 48
2.8 Experimental Section 50
2.8.1 Materials Characterization 50
2.8.2 OSC Device Fabrication and Characterization 51
2.8.3 Synthesis Routes 52
Chapter 3: Development of BDT-Based Donor Polymers Containing Novel Thiophene Comonomers with Triazole Side Chains 60
3.1 Introduction 60
3.2 Polymer Structure Design 61
3.2.1 Density Functional Theory (DFT) Simulations 61
3.2.2 Synthesis Scheme 63
3.3 Physical Properties 64
3.4 Opto-Electrochemical Properties 67
3.5 OPV Performance and Charge Mobility 70
3.6 Crystallinity 77
3.7 Summary and Future Direction 80
3.8 Experimental Section 82
3.8.1 Materials Characterization 82
3.8.2 OSC Device Fabrication and Characterization 82
3.8.3 Synthesis Routes 83
Chapter 4: Synthesis, Characterization, and Performance of a Wide Bandgap Tetrafluorobenzene-BDT D-A Polymer 90
4.1 Introduction 90
4.2 Polymer Structure Design 91
4.2.1 Density Functional Theory (DFT) Simulations 91
4.2.2 Synthesis Scheme 93
4.3 Physical Properties 94
4.4 Opto-Electrochemical Properties 97
4.5 OPV Performance and Charge Mobility 100
4.6 Crystallinity 104

4.7 Summary and Future Direction 106
4.8 Experimental Section 107
4.8.1 Materials Characterization 107
4.8.2 OSC Device Fabrication and Characterization 107
4.8.3 Synthesis Routes 108
Chapter 5: Study of an Acid-Catalyzed Post Polymerization Modification on an Acetal to Yield a Simple, Low-Cost Aldehyde-Substituted BDT-Based Polymer 109
5.1 Introduction 109
5.2 Polymer Structure Design 111
5.2.1 Density Functional Theory (DFT) Simulations 111
5.2.2 Synthesis Scheme 113
5.3 Physical Properties 115
5.4 Opto-Electrochemical Properties 117
5.5 OPV Performance and Charge Mobility 120
5.6 Crystallinity 126
5.7 Summary and Future Direction 128
5.8 Experimental Section 130
5.8.1 Materials Characterization 130
5.8.2 OSC Device Fabrication and Characterization 130
5.8.3 Synthesis Routes 130
Chapter 6: Summary and Future Direction 133
References 137

List of Figures

Figure 1-1: Timeline of solar cell efficiency improvements of various types of materials and cell structures.[2] Reproduced from ref. 2 with permission from NREL. 2
Figure 1-2: BHJ organic solar cell structure.[8] Reproduced from ref. 8 with permission from Springer Nature, copyright 2020..... 3
Figure 1-3: (a) Conventional device structure; (b) Inverted device structure.[11] Reproduced from ref. 11 with permission from John Wiley and Sons, copyright 2018. 4
Figure 1-4: Working principal of a BHJ OSC device.[12] Reproduced from ref. 12, Dracula Technologies' website. 5
Figure 1-5: Solar cell I-V curve, indicating key parameter's locations.[15] Reproduced from ref. 15 with permission from author Stuart Bowden. 7
Figure 1-6: Timeline for efficiency improvements of fullerene and non-fullerene based OSC devices (1986-2020).[17] Reproduced from ref. 17 with permission from John Wiley and Sons, copyright 2021. 8
Figure 1-7: ^{1}H NMR chemical shifts based on the functionality of the atoms involved.[38] Reproduced from ref. 38 with permission from Chemistry Steps. 14
Figure 1-8: a) Edge-on orientation vs. b) Face-on orientation with P3HT as model compound.[47] Reproduced from ref. 47 with permission from author Youngmin Lee, copyright 2021. 18
Figure 1-9: Basic operating principle of AFM.[50] Reproduced from ref. 50, Wikipedia. 19
Figure 2-10: Structures of reference polymer (PTBDT), and polymers containing thiophene comonomers with ethynyl side chains (PSETBDT, PBETBDT, and POBETBDT). 24
Figure 2-11: DFT calculation results showing overall structure, HOMO, LUMO, and dihedral angle for polymers: a) reference PTBDT; b) PSETBDT; c) PBETBDT; d) POBETBDT. 26
Figure 2-12: HT-GPC molecular weight distribution of polymers: a) PSETBDT; b) PBETBDT; c) POBETBDT. 28
Figure 2-13: TGA curves for polymers: PSETBDT, PBETBDT, and POBETBDT. 29
Figure 2-14: DSC curves for polymers: a) PSETBDT; b) PBETBDT; c) POBETBDT. 30
Figure 2-15: Energy diagrams for ITIC, IT-4F, and Y6.[1] 32
Figure 2-16: UV-vis absorption spectra of as-cast thin film, annealed thin film, and chloroform solution for polymers: a) PSETBDT; b) PBETBDT; c) POBETBDT. 33
Figure 2-17: CV profiles of polymers: a) PSETBDT; b) PBETBDT; c) POBETBDT. 34
Figure 2-18: Comparison of DFT predicted HOMO and LUMO levels with CV obtained HOMO and LUMO levels for polymers PSETBDT, PBETBDT, and POBETBDT..... 35
Figure 2-19: PL spectra of a) PSETBDT with IT-4F; b) PSETBDT with Y6; c) PBETBDT with Y6; d) POBETBDT with Y6; e) POBETBDT with IT-4F. 37
Figure 2-20: J-V curve of PSETBDT:Y6 (100 ^{o}C), PSETBDT:IT-4F (50 ^{o}C), and POBETBDT:Y6 (100 ^{o}C). 42
Figure 2-21: EQE of best performing OSCs based on a) PSETBDT:Y6; b) POBETBDT:Y6. .. 42
Figure 2-22: a) electron mobility I-V curves for PSETBDT:Y6, PSETBDT:IT-4F, and POBETBDT:Y6; b) hole mobility I-V curves for PSETBDT, PSETBDT:Y6, PSETBDT:IT-4F, POBETBDT, and POBETBDT:Y6. 44
Figure 2-23: GIXD patterns of films at different annealing temperatures: a) in-plane neat PSETBDT; b) out-of-plane neat PSETBDT; c) in-plane PSETBDT:IT-4F blend; d) out-of-plane PSETBDT:IT-4F blend; e) 2D images of the best performing material (annealed at 50 ^{o}C), where the left is neat PSETBDT and the right is PSETBDT:IT-4F. 46

Figure 2-24: GIXD patterns of films at different annealing temperatures: a) in-plane neat POBETBDT; b) out-of-plane neat POBETBDT; c) in-plane POBETBDT:Y6 blend; d) out-of-plane POBETBDT:Y6 blend; e) 2D images of the best performing material (annealed at 100 ^{o}C), where the left is neat POBETBDT and the right is POBETBDT:Y6. 47
Figure 3-25: Reference polymer (PTBDT) and proposed triazole-substituted thiophene-BDT polymer structures (PTTBDT and PCTBDT). 61
Figure 3-26: DFT calculation results showing overall structure, HOMO, LUMO, and dihedral angle for polymers: a) PTTBDT; b) PCTBDT. 62
Figure 3-27: HT-GPC molecular weight distribution of polymer: a) PTTBDT; b) PCTBDT. ... 64
Figure 3-28: TGA curves for polymers PTTBDT, and PCTBDT. 65
Figure 3-29: DSC curves for polymers: a) PTTBDT; and b) PCTBDT. 66
Figure 3-30: UV-vis absorption spectra of as-cast thin film, annealed thin film, and chloroform solution for polymers: a) PTTBDT; and b) PCTBDT. 67
Figure 3-31: CV profiles of polymers: a) PTTBDT; and b) PCTBDT. 68
Figure 3-32: Comparison of DFT predicted HOMO and LUMO energy levels with CV obtained HOMO and LUMO levels for polymers PTTBDT, and PCTBDT. 68
Figure 3-33: PL spectra of a) PTTBDT with Y6; and b) PCTBDT with Y6. 69
Figure 3-34: J-V curve of best performing OPV devices: PTTBDT:Y6 (RT), PCTBDT:Y6 (RT). 74
Figure 3-35: EQE of best performing OSCs based on a) PTTBDT:Y6; and b) PCTBDT:Y6. ... 74
Figure 3-36: a) electron mobility I-V curves for PTTBDT:Y6, and PCTBDT:Y6; b) hole mobility I-V curves of neat PTTBDT, PTTBDT:Y6, neat PCTBDT, and PCTBDT:Y6. 76
Figure 3-37: GIXD patterns of films at different annealing temperatures: a) in-plane neat PTTBDT; b) out-of-plane neat PTTBDT; c) in-plane PTTBDT:Y6 blend; d) out-of-plane PTTBDT:Y6 blend; e) 2D images of the best performing material (no annealing), where the left is neat PTTBDT and the right is PTTBDT:Y6. 78
Figure 3-38: GIXD patterns of films at different annealing temperatures: a) in-plane neat PCTBDT; b) out-of-plane neat PCTBDT; c) in-plane PCTBDT:Y6 blend; d) out-of-plane PCTBDT:Y6 blend; e) 2D images of the best performing material (no annealing), where the left is neat PCTBDT and the right is PCTBDT:Y6. 79
Figure 4-39: Reference polymer (PBBDT) and proposed fluorinated BDT-benzene polymer (PFBBDT) structures. 91
Figure 4-40: DFT calculation results showing overall structure, HOMO, LUMO, and dihedral angle for polymers: a) reference PBBDT; b) PFBBDT. 92
Figure 4-41: HT-GPC molecular weight distribution of polymer PFBBDT. 94
Figure 4-42: TGA curve for polymer PFBBDT. 95
Figure 4-43: DSC curve for polymer PFBBDT. 96
Figure 4-44: UV-vis absorption spectra of as-cast thin film, annealed thin film, and chloroform solution for polymer PFBBDT. 97
Figure 4-45: CV profile of polymer PFBBDT. 98
Figure 4-46: Comparison of DFT predicted HOMO and LUMO energy levels with CV obtained HOMO and LUMO levels for PFBBDT. 98
Figure 4-47: Photoluminescence spectrum of PFBBDT with Y6. 99
Figure 4-48: J-V curve for PFBBDT:Y6 (50 ^{o}C). 102
Figure 4-49: EQE of best performing OSC based on PFBBDT:Y6. 102

Figure 4-50: Left: electron mobility I-V curve of PFBBDT:Y6; Right: hole mobility I-V curves of PFBBDT and PFBBDT:Y6. 103
Figure 4-51: GIXD patterns of films at different annealing temperatures: a) in-plane neat PFBBDT; b) out-of-plane neat PFBBDT; c) in-plane PFBBDT:Y6 blend; d) out-of-plane PFBBDT:Y6 blend; e) 2D images of the best performing material (annealed at 50 ^{o}C), where the left is neat PFBBDT and the right is PFBBDT:Y6. 105
Figure 5-52: Polymer structures of a reference polymer (PTBDT) and two proposed polymers: an acetal-substituted (PATBDT) and a formaldehyde-substituted (PXTBDT) thiophene-BDT, where the "X" indicates the acetal has been cleaved and converted to an aldehyde. 111
Figure 5-53: DFT calculation results showing overall structure, HOMO, LUMO, and dihedral angle for polymers: a) PATBDT; b) PXTBDT. 112
Figure 5-54: a) ^{1}H NMR of PATBDT; b) ^{1}H NMR of PXTBDT. 113
Figure 5-55: HT-GPC molecular weight distribution of polymer: a) PATBDT; b) PXTBDT.. 115
Figure 5-56: TGA curves for polymers: PATBDT, and PXTBDT. 116
Figure 5-57: DSC curves for polymers: PATBDT, and PXTBDT. 116
Figure 5-58: UV-vis absorption spectra of as-cast thin film, annealed thin film, and chloroform solution for polymers: a) PATBDT, and b) PXTBDT. 118
Figure 5-59: CV profiles of polymers: a) PATBDT, and b) PXTBDT. 118
Figure 5-60: Comparison of DFT predicted HOMO and LUMO energy levels with CV obtained HOMO and LUMO levels for polymers PATBDT, and PXTBDT. 119
Figure 5-61: Photoluminescence spectra of PATBDT with Y6, and PXTBDT with Y6. 119
Figure 5-62: J-V curves for PATBDT:Y6 (100 ^{o}C), and PXTBDT:Y6 (RT) 123
Figure 5-63: EQE of best performing OSCS based on PATBDT:Y6, and PXTBDT:Y6. 124
Figure 5-64: Left: electron mobility I-V curves for PATBDT:Y6, and PXTBDT:Y6; Right: hole mobility I-V curves of neat PATBDT, PATBDT:Y6, neat PXTBDT, and PXTBDT:Y6. 125
Figure 5-65: GIXD patterns of films at different annealing temperatures: a) in-plane neat PATBDT; b) out-of-plane neat PATBDT; c) in-plane PATBDT:Y6 blend; d) out-of-plane PATBDT:Y6 blend; e) 2D images of the best performing material (annealed at 100 ^{o}C), where the left is neat PATBDT and the right is PATBDT:Y6. 126
Figure 5-66: GIXD patterns of films at different annealing temperatures: a) in-plane neat PXTBDT; b) out-of-plane neat PXTBDT; c) in-plane PXTBDT:Y6 blend; d) out-of-plane PXTBDT:Y6 blend; e) 2D images of the best performing material (no annealing), where the left is neat PXTBDT and the right is PXTBDT:Y6. 127

List of Tables

Table 2-1: DFT results for reference polymer, PTBDT, and proposed polymers PSETBDT, PBETBDT, and POBETBDT. 27
Table 2-2: HT-GPC molecular weight and polydispersity data summary. 29
Table 2-3: Optical and electrochemical properties of polymers: PSETBDT, PBETBDT, and POBETBDT. 34
Table 2-4: Summary of OSC device parameters for PSETBDT:Y6. 40
Table 2-5: Summary of OSC performance for PSETBDT:Y6. 40
Table 2-6: Summary of OSC device parameters for PSETBDT:IT-4F. Note: the thickness of these devices was not tested (aside from device 1) and the values listed are estimates based on the other results obtained. 41
Table 2-7: Summary of OSC performance for PSETBDT:IT-4F. 41
Table 2-8: Summary of OSC device parameters for POBETBDT:Y6. 41
Table 2-9: Summary of OSC performance for POBETBDT:Y6. 42
Table 2-10: Comparison of Jsc obtained from OPV and EQE measurements for PSETBDT:Y6, and POBETBDT:Y6. 43
Table 2-11: SCLC hole and electron mobilities for neat polymers and D:A blend films of PSETBDT, and POBETBDT. 44
Table 3-12: DFT results for reference polymer, PTBDT, and proposed polymers PTTBDT, and PCTBDT. 62
Table 3-13: HT-GPC molecular weight and PDI data summary for PTTBDT and PCTBDT. 64
Table 3-14: Optical and electrochemical properties of polymers PTTBDT, and PCTBDT. 68
Table 3-15: Summary of OSC device parameters for PTTBDT:Y6. 72
Table 3-16: Summary of OSC performance for PTTBDT:Y6. 72
Table 3-17: Summary of OSC device parameters for PCTBDT:Y6. 73
Table 3-18: Summary of OSC performance for PCTBDT:Y6. 73
Table 3-19: Comparison of Jsc obtained from OPV and EQE measurements for PTTBDT:Y6, and PCTBDT:Y6. 74
Table 3-20: SCLC hole and electron mobilities for neat polymers and D:A blend films of PTTBDT, and PCTBDT with Y6. 75
Table 4-21: DFT results for the reference polymer (PBBDT) and the proposed benzene-BDT polymer (PFBBDT). 93
Table 4-22: HT-GPC molecular weight and PDI data summary for PFBBDT. 94
Table 4-23: Optical and electrochemical properties of polymer PFBBDT. 98
Table 4-24: Summary of OSC device parameters for PFBBDT:Y6. 101
Table 4-25: Summary of OSC performance for PFBBDT:Y6. 101
Table 4-26: Comparison of Jsc values obtained from OPV and EQE measurements for PFBBDT. 102
Table 4-27: SCLC hole and electron mobilities for the neat polymer and D:A blend film of PFBBDT and Y6. 103
Table 5-28: DFT results for the reference polymer, PTBDT, and proposed polymers, PATBDT and PXTBDT. 112
Table 5-29: HT-GPC molecular weight and PDI data summary for PATBDT and PXTBDT. 115
Table 5-30: Optical and electrochemical properties of polymers PATBDT, and PXTBDT. 118
Table 5-31: Summary of OSC device parameters for PATBDT:Y6. 121
Table 5-32: Summary of OSC performance for PATBDT:Y6. 122

Table 5-33: Summary of OSC device parameters for PXTBDT:Y6. 122
Table 5-34: Summary of OSC performance for PXTBDT:Y6. 123
Table 5-35: Comparison of Jsc values obtained from OPV and EQE measurements for PATBDT, and PXTBDT..... 124
Table 5-36: SCLC hole and electron mobilities for neat polymers and D:A blend films of PATBDT, and PXTBDT with Y6..... 125

List of Schemes

Scheme 2-1: Synthesis scheme for ethynyl polymers: PSETBDT, PBETBDT, and POBETBDT. 27
Scheme 3-2: Synthesis scheme for triazole polymers: PTTBDT, and PCTBDT. 63
Scheme 4-3: Synthesis scheme for polymer PFBBDT..... 93
Scheme 5-4: Synthesis scheme for polymers PATBDT, and PXTBDT. 114

List of Abbreviations

1D: One-dimensional
2D: Two-dimensional
AFM: Atomic Force Microscopy
BDT: Benzodithiophene
BFI: tetraazabenzodifluoranthene diimide
BHJ: Bulk Heterojunction
CV: Cyclic Voltammetry
D-A: Donor-Acceptor
DCM: Dichloromethane
DMF: N,N-Dimethylformamide
DSC: Differential Scanning Calorimetry
EDOT: 3,4-Ethylenedioxythiophene
EWG: Electron-Withdrawing Group
FF: Fill Factor
GPC: Gel Permeation Chromatography
HOMO: Highest Occupied Molecular Orbital
IPA: Isopropanol
IT-4F: 3,9-bis(2-methylene-((3-(1,1dicyanomethylene)-6,7-difluoro)-indanone))-5,5,11,11-tetrakis(4-hexylphenyl)-dithieno[2,3-d:2',3'-d']-s-indaceno[1,2-b:5,6-b']dithiophene
ITIC: 3,9-bis(2-methylene-(3-(1,1dicyanomethylene)-indanone))-5,5,11,11-tetrakis(4-hexylphenyl)-dithieno[2,3-d:2',3'-d']-s-indaceno[1,2-b:5,6-b']dithiophene
ITO: Indium Tin Oxide
LiF: Lithium Fluoride
LUMO: Lowest Unoccupied Molecular Orbital
NFA: Non-Fullerene Acceptor
NMR: Nuclear Magnetic Resonance
OPV: Organic Photovoltaics
OSC: Organic Solar Cell
P3HT: Poly(3-hexylthiophene-2,5-diyl)
PCBM: Phenyl-C61-Butyric acid Methyl ester
PCE: Power Conversion Efficiency
PDI: Perylenediimide
PDI: Polydispersity Index
PEDOT:PSS: Poly(3,4-Ethylene dioxythiophene) Polystyrene Sulfonate
PL: Photoluminescence
PLQE: Photoluminescence Quenching Efficiency
PTSA: p-Toluenesulfonic Acid

PV: Photovoltaic
Rms: Root Mean Square
SCLC: Space-charge-limited Current
TGA: Thermogravimetric Analysis
UFF: Universal Force Field
UV-vis: Ultraviolet-visible
XRD: X-ray Diffraction
Y6: 2,2'-((2Z,2'Z)-((12,13-bis(2-ethylhexyl)-3,9-diundecyl-12,13-dihydro-[1,2,5]thiadiazole[3,4-e]thieno[2",3":4',5']thieno[2',3':4,5]pyrrolo[3,2-g]thieno[2',3':4,5]thieno[3,2-b]indole-2,10-diyl)bis(methanylylidene))bis(5,6-difluoro-3-oxo-2,3-dihydro-1H-indene-2,1-diylidene))dimalononitrile
ZnO: Zinc Oxide

List of Symbols

ε: Molar absorptivity
ε_0: Vacuum permittivity
$\lambda_{max,100}$: Maximum absorbance of thin film annealed at 100 ^oC
$\lambda_{max,RT}$: Maximum absorbance of as-cast thin film
$\lambda_{max,s}$: Maximum absorbance in solution
λ_{onset}: Onset absorption wavelength
μ: mobility
A: Absorbance
Ag: Silver
Al: Aluminum
c: concentration
E_{HOMO}: HOMO Energy Level
E_{LUMO}: LUMO Energy Level
J_{sc}: Short Circuit Current Density
ℓ: Path Length of Light
l: Thin Film Thickness
M_i: Mass of i, where i is the polymer being measured
M_n: Number-average Molecular Weight
M_w: Weight-average Molecular Weight
N_i: Number of molecules of i, where i is the polymer being measured
P_{in}: Input Power
R_s: Series Resistance
R_{sh}: Shunt Resistance
T_c: Crystallization Temperature
T_g: Glass Transition Temperature
T_m: Melting Temperature
V_{loss}: Voltage losses
V_{oc}: Open Circuit Voltage
W_i: Weight of i, where i is the polymer being measured

Chapter 1: Introduction

1.1 Overview of Organic Solar Cells

The exponential increase in global population and economic development has put stress on the world's current energy production systems. The use of fossil fuels for energy production is unsustainable and detrimental to the environment, which has led to an increase in research of renewable energy sources.[1] Among these, solar energy is a prime candidate for significant growth due to low cost and an abundance of the energy source, sunlight.[2] A comparison between the environmental footprint of different technologies (carbon dioxide and other greenhouse gas emissions over the lifespan of each technology) shows that natural gas accounts for 400-500 g/kWh and coal accounts for 900-1000 g/kWh, whereas silicon solar cells account for 50 g/kWh.[3] Additionally, policy surrounding solar energy is beginning to be implemented; for example, beginning in 2020 as part of their building code, California introduced a mandate for the installation of solar panels onto new homes.[4] These positive movements are encouraging early signs for the implementation of solar energy on a significantly larger scale.

Historically, inorganic silicon has been the industry leader in solar cell technology due to low cost, long-term stability, and good performance. However, the rigidity of these materials can lead to potential problems for mass production due to the requirement of large amounts of space.[5,6] Organic solar cells (OSCs) have emerged as an intriguing alternative due to their low cost, flexibility, lightweight, and easy processability.[1] Flexibility will allow for applications where silicon solar cells are not possible including curved surfaces and wearable electronics. The lightweight, thin film structure of OSCs allows for potential applications in portable electronics. Furthermore, OSCs show potential for indoor and semitransparent applications.[5] These applications provide an avenue for OSCs to enter the current photovoltaic (PV) market, which will establish demand for OSCs without direct competition with silicon PV. OSCs also account for a significantly lower environmental footprint, with an estimate of 5-9 g/kWh compared to 50 g/kWh for silicon-based solar cells, making them competitive with other renewables including wind and hydro.[3] Finally, one of the most intriguing advantages from a manufacturing perspective is the solution processability, which will allow for fast, large-scale roll-to-roll printing.

Over the past three decades, considerable progress has been made, leading to recent rapid performance improvements in OSCs.[1] These improvements are largely attributable to the design of new acceptor and donor materials, and the optimization of the solar cell structures.[7] Currently, the best power conversion efficiency (PCE) for OSCs is greater than 18 % (as seen in ***Figure 1-1***), which still trails the industry leading single crystal silicon solar cells (26.1 %).[2] Commercialization will require improvements to the performance, cost, and stability for the development of economically viable OSC products that rival traditional silicon photovoltaics.[1]

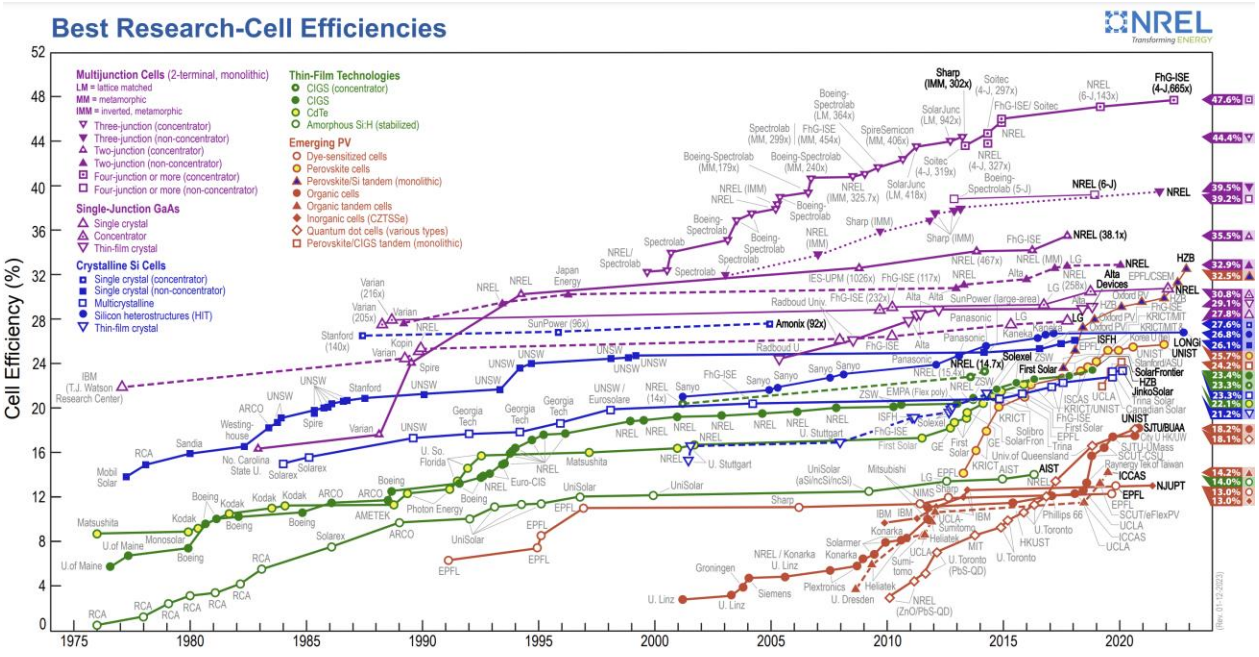

Figure 1-1: Timeline of solar cell efficiency improvements of various types of materials and cell structures.[2] Reproduced from ref. 2 with permission from NREL.

1.2 The Development of the Bulk Heterojunction Solar Cell

The first OSCs, called monolayer devices, consisted of a thin organic active layer between two electrodes.[6] Due to the low performance of these devices, Tang et al. developed a bilayer device in 1986.[6] The concept of this device was to pair an electron donor material and an electron acceptor material as two separate layers, where the charges would travel to their respective electrodes due to differences in the electron affinity and ionization potential of the two materials.[6] However, there was a significant issue with these OSC devices: in traditional inorganic silicon devices, free charge carriers are generated, whereas in OSC devices, electron-hole pairs, also known as excitons, which are bound together by Coulomb forces, are generated due to low dielectric constants.[3,6] Therefore, the high binding energy limits the ability of these excitons to dissociate and results in small diffusion lengths, leading to recombination and low efficiency.[6]

To address these issues, the bulk heterojunction (BHJ) cell was developed by Heeger and Holmes' groups simultaneously in 1995.[6] The basic concept of the BHJ is to mix the acceptor and donor material, creating a bi-continuous, interpenetrating network of electron acceptor and donor phases.[6] **Figure 1-2** shows the morphology, where the donor and acceptor are separated by a distance smaller than the exciton diffusion length, allowing charge dissociation at the interface.[6] Despite this structure resulting in better efficiencies, the morphology and phase separation are difficult to control during lab-scale deposition methods like spin coating.

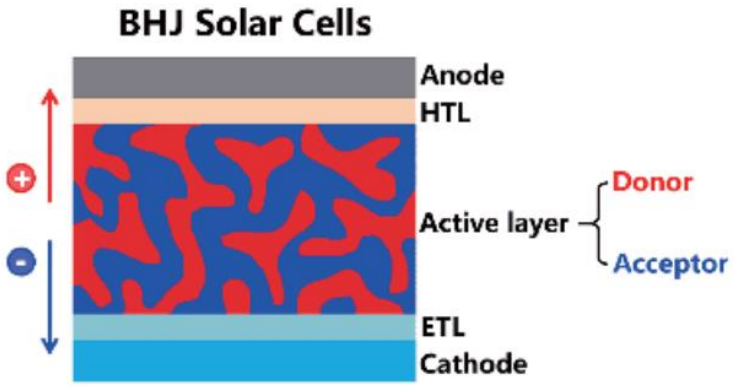

Figure 1-2: BHJ organic solar cell structure.[8] Reproduced from ref. 8 with permission from Springer Nature, copyright 2020.

1.2.1 Conventional and Inverted BHJ Structures

OSCs have been tested in two configurations, conventional and inverted, with the difference being the direction of charge transport. Conventional devices have holes collected at the indium tin oxide (ITO) electrode and electrons collected at the aluminum (Al) electrode, whereas inverted devices collect electrons at ITO and holes at silver (Ag). An example of a conventional structure for OSCs is ITO/PEDOT:PSS/acceptor:donor/LiF/Al where the slash denotes a change in the layer and colons indicate a two component layer.[9] An example of an inverted structure is: ITO/ZnO/donor:acceptor/PEDOT:PSS/Ag.[9] Inverted structures are often preferred due to better stability from a reduction in degradation effects caused by oxygen and moisture.[10] The conventional and inverted structures can be seen in **Figure 1-3**.

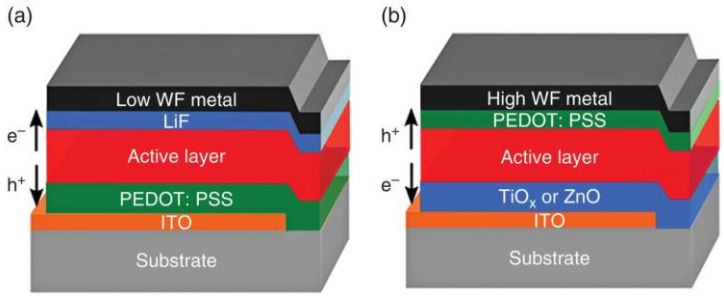

Figure 1-3: (a) Conventional device structure; (b) Inverted device structure.[11] Reproduced from ref. 11 with permission from John Wiley and Sons, copyright 2018.

1.2.2 Working Principal of BHJ Active Layer

As seen in **Figure 1-4**, the process of generating electricity from OSCs can be broken down into five simple steps.[1,12] Initially, the light is absorbed by the active layer materials (step 1). Light absorption results in exciton formation (step 2). The excitons then travel to the interface between the acceptor and donor material, which must be closer than the diffusion length to avoid recombination (step 3). At the interface, the excitons can dissociate into free electrons and holes (step 4). Finally, the electrons and holes can move through the acceptor and donor phases until they reach the cathode and anode, respectively (step 5). In a normal BHJ device there are thin hole and electron blocking layers, which assist with the direction of charge migration.[12] Once the charges reach the electrodes, the process is complete and energy is produced by the OSC device.[1,6]

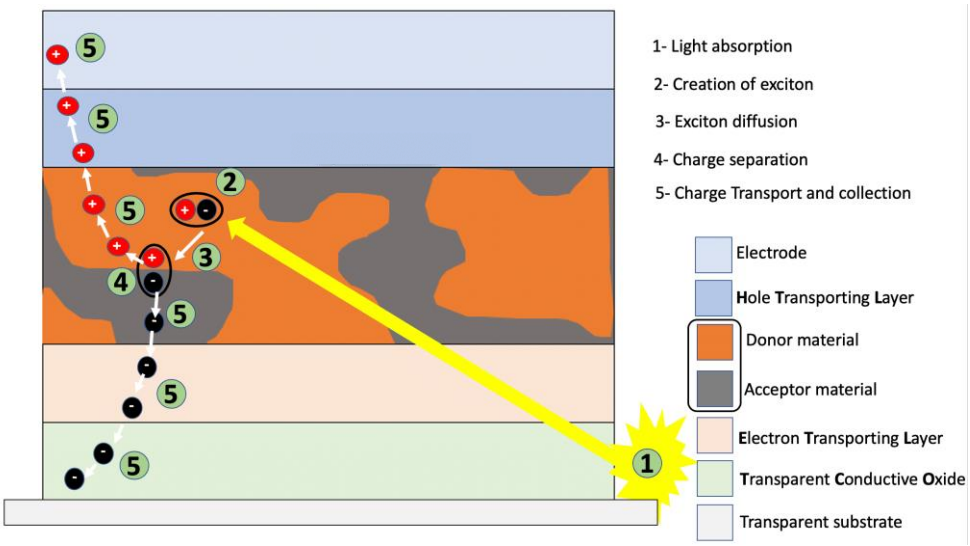

Figure 1-4: Working principal of a BHJ OSC device.[12] Reproduced from ref. 12, Dracula Technologies' website.

1.3 OSC Performance Metrics

In terms of design requirements, **Eq. 1** can be used to calculate the power conversion efficiency (PCE) of OSCs, which describes the performance of the donor and acceptor materials:[7]

$$PCE = \frac{J_{SC}V_{OC}FF}{P_{in}} \qquad \textbf{Eq. 1}$$

where J_{SC} is the short circuit current density, V_{OC} is the open circuit voltage, FF is the fill factor, and P_{in} is the input power.[7]

J_{SC} is a measure of the current when the voltage is zero. Several factors affect Jsc including the light source spectrum and intensity, and the cell area. However, if the light source is calibrated to represent one sun, the Jsc is affected by the absorption characteristics of the active material, as well as exciton diffusion, dissociation, and collection.[1,13,14]

V_{OC} is the maximum voltage from the cell when the current is zero. This characteristic is determined by the difference between the highest occupied molecular orbital (HOMO) of the donor and lowest unoccupied molecular orbital (LUMO) of the acceptor, where a lower HOMO level of the donor corresponds to higher V_{oc}.[1] Furthermore, large dielectric constants increase the occurrence of exciton dissociation, resulting in high V_{oc} with a smaller energy level difference.[1]

As seen in **Figure 1-5**, FF is a measure of how square the J-V curve is for a solar cell.[15,16] Ideally, the FF value would be 100 %; however, in practice inorganic solar cells have a FF of around 90 % and OSCs are in the range of 50-70 %.[16] Since FF is determined by the relative ease of charge extraction, it will be lower than 42 % if space charge limited current (SCLC) dominates.[16] There are three main factors that affect the FF: series resistance (R_s), shunt resistance (R_{sh}), and the diode. Series resistance is a measure of the bulk and contact resistances of the active layer and electrode materials.[16] This value should be as low as possible. In contrast, shunt resistance is ideally infinite because it measures current leakage through a pinhole or edge of a device.[16] The diode is where the excitons are first created. Therefore, high mobility helps maximize FF because it limits the opportunity for recombination. In some devices, an “S-kink” is seen, which means there is a carrier accumulation on the interior of the device. This indicates that some factor is limiting charge extraction, which inherently decreases the FF.[16] Overall, FF is the most complicated factor to understand but focus should be on ensuring the interface between

materials is smooth and charges can be effectively removed from the system by having high mobility active layer materials and effective blocking layers.

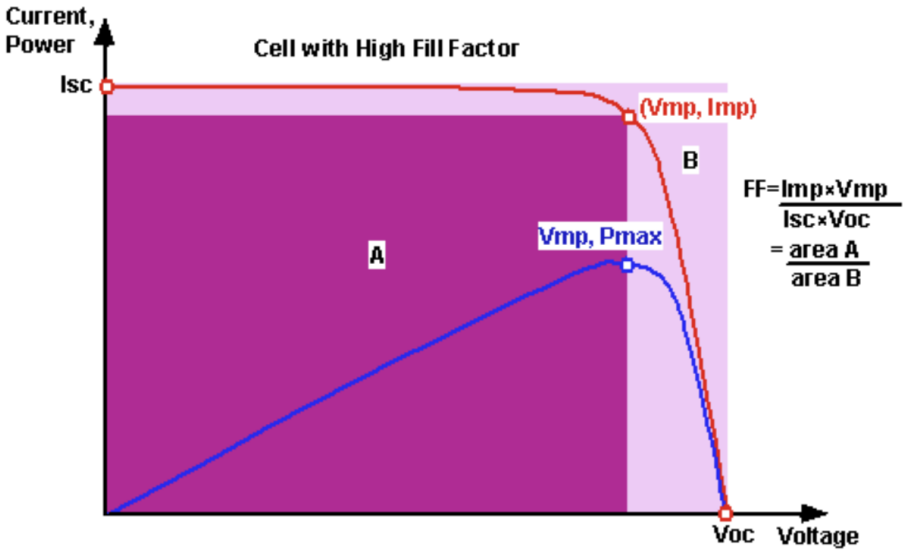

Figure 1-5: Solar cell I-V curve, indicating key parameter's locations.[15] Reproduced from ref. 15 with permission from author Stuart Bowden.

1.4 Brief History of Acceptor and Donor Materials for OSCs

The active layer of OSCs consists of an electron acceptor and an electron donor. Although research on all-polymer OSC devices is also ongoing, these devices suffer from poor morphology due to difficulties in preventing overly crystalline films.[6] Thus, historically, research has focused on pairing small molecule acceptors with polymer donors.[1,6] The following sections will introduce the breakthrough materials for acceptors and donors, respectively.

1.4.1 Acceptor Materials

Historically, fullerene-based acceptors were used due to their fast electron transfer, highly organized three-dimensional shape, good phase separation, small reorganization energy, high electron affinity, and slow back transfer of electrons.[17] The best fullerene-based OSCs achieved a PCE of 12.1% in 2017.[17] However, due to the limited absorption of fullerene materials, non-fullerene acceptors (NFAs) have become an important area of research since their performance has significantly exceeded the performance of fullerenes (see **Figure 1-6**).[17]

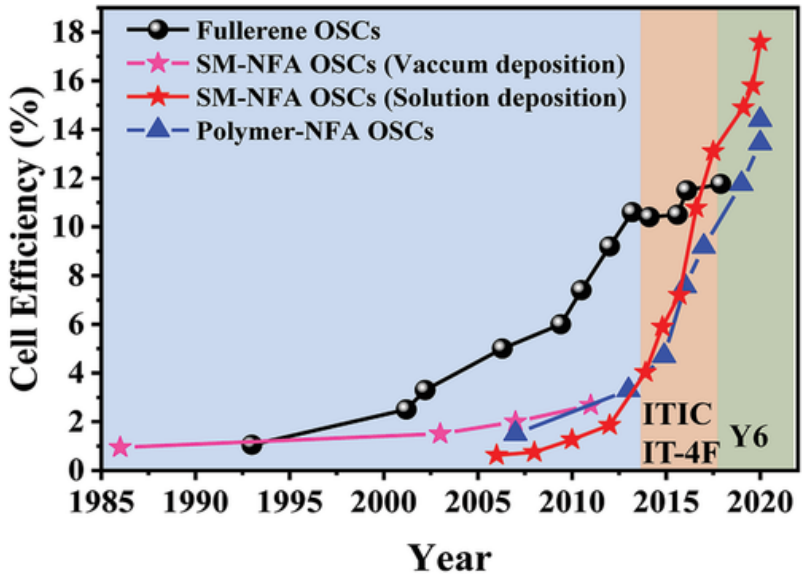

Figure 1-6: Timeline for efficiency improvements of fullerene and non-fullerene based OSC devices (1986-2020).[17] Reproduced from ref. 17 with permission from John Wiley and Sons, copyright 2021.

NFA materials are of interest because they can be designed with better electrochemical properties.[17] Unlike fullerene acceptors, NFAs are the component of the active layer with the narrower bandgap and are generally planar instead of spherical.[17] However, NFAs often have

problems with crystallization that must be addressed to maximize the performance.[18] In 2015, relatively high-efficiency NFA OSCs were developed and in 2017, the performance of solar cells based on NFAs surpassed the best fullerene-based devices.[17]

Research regarding NFAs started to gain popularity between 2000 to 2012. The first NFAs were based on perylene tetracarboxydiimide (PDI). PDI's have a low lying LUMO, strong absorption, strong π-π intermolecular interactions, and decent charge mobility.[17,19,20] However, the planarity of these NFA molecules resulted in poor morphology due to excessive aggregation, and inherently, poor efficiency.[17] Thus, between 2013 to 2016, research focused on adapting the NFA planar materials into three-dimensional-like molecules.[17] For example, Zhao et al. used a spirobifluorene to connect two PDI molecules (SF-PDI_2), which limited aggregation.[17] In 2014, thiophene was used as a π-bridge to connect two fused-ring tetraazabenzodifluoranthene tetracarboxydiimides (BFI), which resulted in an impressive performance of 5% PCE.[17] This was further improved to 8.52% by using 3,4-ethylenedioxythiophene (EDOT) as the connecting π-bridge molecule and increasing the backbone twisting.[17] Other discoveries during this period include $SF(DPPB)_4$, which included a spirobifluorene with 4 diketopyrrolopyrrole (DPP) units, providing efficiency of 9.5% when blended with SF-PDI_2, and a selenium annulated triperylene hexamide (TPH-Se).[17] The most important discovery during these four years was in 2015 when ITIC was synthesized by Zhan et al..[17] ITIC has strong light absorption, bulky side chains that led to good morphology and solubility, and a narrow bandgap, leading to a PCE of 6.8% when paired with PTB7-Th.[17] The synthesis of ITIC provided PCEs around 11%, which met a key milestone where NFA materials were performing as well as the top fullerene acceptors.[17]

From 2017 to 2020, the focus shifted to A-D-A systems, with molecular engineering becoming important.[17,19] For example, Hou et al. made the first OSC system that exceeded 13% PCE by adding difluorinated end units to ITIC to create the acceptor IT-4F.[17] This modification allowed for a smaller bandgap and better light absorption.[17] Ding et al. synthesized a new type of carbon-oxygen bridged ladder units that have strong electron-donating cores, which resulted in better light absorption and electron mobility than carbon-bridged options (IDT, IDTT).[17] The first example, CO5IC, had a PCE of 7.5%; however, this has been improved to over 17% by modifying the structure.[17] In 2019, Yuan et al. developed a high performance material, Y6, which had high electron affinity and low E_g^{opt}, resulting in a record performance of 15.7 % when

blended with a commercial donor, PM6.[21] The advantages of Y6 include an electron-deficient centre (benzothiadiazole), with two alkyl chains attached at the outside thiophene, and two alkyl chains attached at the inner pyrrole rings.[21] Recently, a record PCE of 18.22 % was achieved by Ding et al. by blending Y6 with a polymer donor, D18.[17]

Currently, star-shaped molecules are the most promising acceptor materials.[17] These include Y6 and IT-4F.[17] The advantageous properties that have allowed for high PCEs include efficient packing, high charge transport, narrow bandgaps, good visible to near-infrared light absorption, and compatibility with many donors.[17] However, these materials have complex synthesis routes, which limits their potential for commercial applications due to long and expensive processes.[17]

In search of better acceptor materials with easier synthesis methods, research on simple fused-ring A-D-A systems has increased.[17] There are several examples including MO-IDIC-2F acceptor and PTQ10 low-cost donor, and BTzO-4F acceptor with PBDB-T donor, which have shown PCEs greater than 13%.[17] This is a promising development; however, the PCE is 5% lower than the star-shaped molecules so further research is required to find ways of modifying the structures to get better performance.[17]

1.4.2 Donor Materials

Donor materials have advanced through several stages over the past few decades. Originally, polyphenylene vinylenes were the focus in the 1990s, with alkoxy group additions allowing for solubility; however, low J_{sc} and large bandgaps limited the performance to 3.3%.[22–24] Thiophene-containing materials became a promising donor due to good stability, good electron-donating properties, and low steric hindrance to allow for good morphology.[1] Research began to focus on poly(3-hexylthiophene) (P3HT) because of higher J_{sc} and hole mobility, low bandgap, and better morphology, which led to higher PCEs of 5%.[22] P3HT is still one of the leaders for large-area OSCs because of low fabrication costs; however, the performance is relatively poor compared to other donor materials due to a high HOMO level limiting the V_{oc}, and poor light absorption.[22,25,26] This has led to an increase in research for other options that can potentially provide a similar low cost of P3HT, with significantly better performance.

Since NFAs are designed with small bandgaps, it is beneficial to have wide-bandgap donor materials for complementary light absorption.[1] Donor-acceptor (D-A) polymer building blocks have become increasingly important as donor materials in OSCs since the energy levels and bandgaps are easily tunable via intramolecular charge transfer.[1] Benzodithiophene (BDT) derivatives are a well established D unit for donor polymers due to the planar structure, stability, and good electron donating effect.[1] The highest PCE (13.91%) for an OSC with ITIC as the acceptor was achieved for a system using a BDT-FBTA D-A setup.[1] BDT based donors have also been examined with IT-4F as the acceptor material. BDT with an ester substituted thiophene as the A unit achieved a PCE of 14.2%.[1] This OSC system had high and balanced mobility, and high exciton dissociation; however, the backbone is twisted due to steric effects and would benefit from increased planarity.[1]

Y6 was also used to evaluate the performance of various BDT-based donor materials. Among BDT-based D-A donor polymers, PM6 developed by Zhang et al., was a break through material, which achieved high performance (15.7 %) with Y6.[27] The advantageous structure of PM6, with a fluorine atom on the BDT structure at the top and bottom thiophene units, lowers the E_{HOMO} and allows for face-on packing, while maintaining a wide bandgap.[27] BDT with imide derivatives as the A unit displayed a wider light absorption range, face-on orientation, and good morphology, resulting in a PCE of 16.02%.[1] Furthermore, systems with diketone as the A unit had high FF, V_{oc}, external quantum efficiency (EQE), and J_{sc}, resulting in a high PCE of 16.42%.[1] Finally, Y6 with a BDT (D unit) and Qx derivative (A unit) resulted in a PCE of 15.4%.[1] All these combinations are achieving high performance and with continual improvements, the 20% PCE barrier could be broken shortly.

To improve the performance of BDT, continued substituent manipulation and testing are required. The A unit should continue to be researched to improve the D-A system for the BDT-based donor materials, which is what this thesis will target.

1.5 Design Principles of Polymer Donors

To design effective donor materials, five essential factors must be considered: light absorption, exciton mobility, energy level difference, solubility, and morphology.[7] Balanced maximization of these design principles will allow for high performance.[28] It is also critical to ensure the synthesis route is simple and inexpensive.

1.5.1 Light Absorption

The absorption spectrum of OSCs is a very important area of research because the narrow absorption range of polymer materials is limiting the PCE since the J_{SC} value is generally lower than desired.[7] Therefore, the absorption spectrum of newly designed polymer donor and acceptor materials needs to align with the solar irradiation spectrum in the visible and near-infrared wavelengths.[7,28] This can be achieved by developing donor materials with high absorption coefficients ($>10^5$ cm^{-1}) to allow for broad and intense absorption of sunlight.[7] Increasing the degree of conjugation is one of the main strategies employed to improve absorption.[29] Furthermore, optimal matching of acceptor and donor materials can increase the absorption spectrum range and intensity.[30] Achieving good, complementary absorption will allow for high J_{sc}, which will contribute to improved PCE.

1.5.2 Charge Mobility

The ratio of hole-to-electron mobility has a direct impact on the FF and V_{oc}.[7] Thus, having polymers with balanced mobility results in better performance.[7] To match hole mobility with typical electron mobility, the hole mobility should be $\geq 10^{-4}$ ($cm^2V^{-1}s^{-1}$), with higher mobility resulting in better J_{sc}, V_{oc}, and FF.[7,28,30]

1.5.3 Energy Levels

The energy level difference affects the V_{OC}, which is shown in **Eq. 2**:

$$V_{OC} = \frac{(E_{HOMO} - E_{LUMO} - 0.3\ eV)}{e} \qquad \textbf{Eq. 2}$$

where E_{HOMO} is the energy of the HOMO for the donor material, E_{LUMO} is the energy of the LUMO for the acceptor material, and e is the elementary charge.[7] For efficient charge separation,

0.3 eV is an empirical value for exciton binding energy.[7] Therefore, the difference between the donor HOMO energy and the acceptor LUMO energy must be larger than the exciton binding energy for efficient charge separation to occur.[7] However, NFAs have made it possible to have smaller energy gaps (0.1 to 0.3 eV) while still achieving good performance.[6] The higher V_{oc} allows for excitons to dissociate to charge carriers.[28] This is an important parameter since the electrodes are in competition with bulk and surface recombination for the electrons and holes.[31] To maximize the energy difference, the donor HOMO and acceptor LUMO should be as far apart as possible.[20] However, a balance is required to avoid energy loss issues.[32]

1.5.4 Solubility

Good solubility of polymer donors in common organic solvents allows for solution processability, which can bring down the manufacturing costs of OSCs.[7,28] Furthermore, solubility affects the film formation and interconnectivity of the charge transport network within the nanoscale polymers.[7] A highly penetrable network allows for high J_{SC} and FF, which contribute to high PCE. The solubility of polymer materials can be altered by manipulating the intermolecular interactions, backbone rigidity, degree of polymerization, the polarity of the attached substituents, structure perturbation, and length of aromatic groups.[7,33] Likewise, the side group type, length, and branch point can improve or decrease solubility.[17]

1.5.5 Morphology

The morphology of the polymer active layer in OSCs strongly impacts the charge transfer, transport, and collection.[7] This can have a substantial affect on the FF. Crystallinity, domain purity, and size all play a role in the morphology of the polymer materials. Donor and acceptor nano-scale phase separation and morphology control allow for a charge transport network that is bicontinuous.[28] Annealing (solvent or thermal) allows for morphology control.[7] Furthermore, for certain types of polymers, mixing solvents can improve the morphology, and subsequently the PCE of the OSCs. The advantage of the BHJ structure for OSCs is it allows for an interpenetrating network, which promotes charge dissociation at the interface between donor and acceptor domains.[6] However, the morphology and phase separation remain difficult to control due to methods such as spin coating, making this an area where optimization is necessary.

1.6 Characterization Methods for OSC Materials and Devices

The following sections will detail the characterization techniques used to obtain the chemical, physical, opto-electrochemical, and morphological properties of the materials in this thesis.

1.6.1 Chemical Structure

Nuclear magnetic resonance (NMR) is the main tool used for structural characterization of organic molecules. The benefits of NMR include identification of atom position, isomerization, and conformation.[34–37] As seen in **Figure 1-7**, peaks will appear in different locations depending on the functional groups. Using the peak positions, splitting, and integration in a spectrum, the product structure and purity can be verified. For this thesis, ^{1}H NMR was used to confirm the structures of intermediate materials, and two polymers involved in a post polymerisation modification.

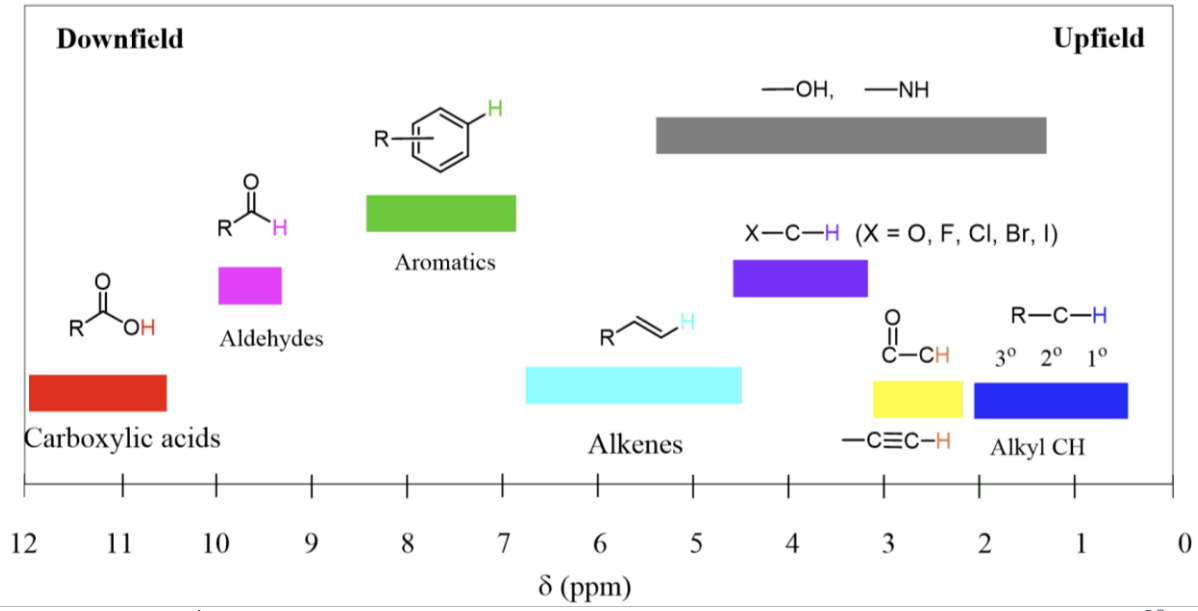

Figure 1-7: ^{1}H NMR chemical shifts based on the functionality of the atoms involved.[38] Reproduced from ref. 38 with permission from Chemistry Steps.

1.6.2 Physical Properties

Gel permeation chromatography (GPC) is important for the determination of a polymer's molecular weight and distribution, which can have an effect on solubility, morphology, and optical properties.[36,39] The basic function of GPC is a column filled with a porous material of various pore sizes, which allows for the separation of molecules. A dilute solution of a polymer is eluted by a constant flow of a solvent. The retention time of the polymer is proportional to the molecular weight, and the polymer is detected via light scattering.[40] For optimal results, this process can be calibrated to a flexible polymer standard; however, for the purpose of this thesis, polystyrene was used as a reference, with 1,2,4-trichlorobenzene as the eluent at an operation temperature of 150°.[39] There are several important values obtained from GPC measurements including weight-average molecular weight (M_w), number-average molecular weight (M_n), and polydispersity index (PDI). If the PDI is equal to one, the polymer is considered uniform; however, it is more likely that the PDI is greater than one, although it is usually preferential to have a relatively low PDI.[36] The mathematical definitions of these three metrics are shown in **Eq. 3**, **Eq. 4**, and **Eq. 5**:

$$M_n = \frac{\Sigma N_i M_i}{\Sigma N_i} \qquad \boldsymbol{Eq.3}$$

$$M_w = \frac{\Sigma W_i M_i}{\Sigma W_i} \qquad \boldsymbol{Eq.4}$$

$$PDI = \frac{M_w}{M_n} \qquad \boldsymbol{Eq.5}$$

where N is the number of molecules with M weight, whereas W is the weight fraction of molecules in a polymer sample.

Thermogravimetric analysis (TGA) measures the sample mass versus temperature, providing an indication of the thermal stability of the polymer.[36,37] Typically, the system is programmed to continually increase the temperature at a constant rate over time, with a scale measuring any changes in mass. The mass loss is usually stepwise where a significant portion is lost within a small range of temperature. Information on chemical and physical events can be interpreted including volatile component loss, thermal degradation, oxidation, and desorption.[36,37] For this thesis, a heating rate of 10 °C/min under nitrogen was used over a range of 50 to 600 °C.

Differential scanning calorimetry (DSC) is another thermal analysis technique, which is used to plot heat flux versus temperature.[36] The operation of DSC includes having the sample and a blank reference sample under the same conditions with a programmable temperature cycle. The advantage of DSC is the polymer is subjected to a broad dynamic range of heating and cooling instead of methods that have fast thermal scans that result in changes to the polymer.[37,41] From DSC, the glass transition temperature (T_g), cold crystallization temperature (T_c), and melting temperature (T_m), along with enthalpy and entropy changes can be observed.[36,41,42] However, due to the rigid backbone and semicrystalline nature of D-A polymers, often the T_g is not clear.[42] For this thesis, a scanning rate of 10 °C/min under nitrogen was used, where the first cycle went until 50 °C lower than the second cycle, and the second cycle went until 0.5% polymer weight was lost in TGA.

1.6.3 Opto-Electrochemical Properties

Ultraviolet-visible spectroscopy (UV-vis) refers to absorption of wavelengths in part of the UV range (200-400 nm) and the visible spectrum (400-800 nm), as well as usually including some near infrared radiation (800-1100 nm).[36] When a photon is absorbed by a molecule, an electron is excited from the ground state. Conjugated polymers allow for electron transition from $\pi \rightarrow \pi^*$ and $n \rightarrow \pi^*$ due to their double bonds.[36] From UV-vis, a relationship between the concentration of the polymer in solution and the absorbance can be described by Beer's Law shown in **Eq. 6** below:[43]

$$A = \varepsilon \ell c \qquad \boldsymbol{Eq.6}$$

where ε is the molar absorptivity coefficient, ℓ is the optical path length, and c is the concentration. UV-vis can also be taken for thin films and due to different orientations in solution versus in film, the spectrum may have different features present. An important data point from UV-vis is the optical bandgap, which can be obtained using **Eq. 7**.

$$E_g(eV) = hf = h\frac{c}{\lambda_{onset}} \approx \frac{1240}{\lambda_{onset}} \qquad \boldsymbol{Eq.7}$$

For this thesis, the range of 350 to 1100 nm was measured for UV-vis due to excessive noise below 350 nm. Samples of both thin films on glass substrates and solutions in chloroform were measured.

Cyclic voltammetry (CV) is an electrochemical technique used to measure current (I) versus voltage (V), which can provide the HOMO and LUMO energy levels with respect to a reference. CV is measured using a thin film of polymer on a working electrode, with a reference such as ferrocene, in a moderately polar solvent (e.g., acetonitrile) with an organic salt electrolyte.[44] Using **Eq. 8** and **Eq.9**, the E_{HOMO} and E_{LUMO} can be calculated, respectively.

$$E_{HOMO}(eV) = -e(E_{ox}^{onset}) - 4.8\ eV \qquad \boldsymbol{Eq.8}$$

$$E_{LUMO}(eV) = -e(E_{red}^{onset}) - 4.8\ eV \qquad \boldsymbol{Eq.9}$$

For this thesis, an I-V curve from -1.2 eV to 1.2 eV was obtained to see both the oxidation and reduction regions.

Photoluminescence (PL) spectroscopy uses light energy to measure the emission of photons. For OSCs, it is important to measure the PL quenching efficiency (PLQE) to determine if the excitons are effectively dissociated in the active layer.[45] If effective results are obtained, the peaks of the donor and acceptor will become flat lines when the mixed active layer is measured. The PLQE can be calculated with **Eq. 10**, where it is a measure of the number of photons emitted versus the number absorbed.

$$PLQE = 1 - \frac{PL_{blend}}{PL_{neat}} \qquad \boldsymbol{Eq.10}$$

This method involved preparing thin film samples of pristine polymer, pristine acceptor, and a blend film to observe quenching.

1.6.4 Morphological Properties

X-ray diffraction (XRD) uses x-ray radiation to investigate the crystal structure of the polymer and polymer:acceptor films. Both one-dimensional (1D) and two-dimensional (2D) setups can be used for XRD.[46] From this technique the crystal form, degree of crystallinity, and interplanar spacing can be obtained.[36,46] Bragg's law (**Eq. 11**) can be used to calculate the interplanar spacing (d-spacing):[36]

$$d = \frac{\lambda}{2sin\theta} \qquad \boldsymbol{Eq.11}$$

This technique allows for the observation of π-π stacking peaks, lamellar peaks, and backbone stacking.[46] This is particularly important for OSCs since the orientation of the polymer chains

effects the charge mobility and separation. If peaks are observed, the polymer either has a face-on or edge-on orientation depending on where the peak is located in the data; however, if there are no peaks the polymer adopts an amorphous orientation (see **Figure 1-8**).[1] For this thesis, samples were prepared by spin coating solutions of pristine polymer donor and a blend of donor and acceptor onto silicon substrates. For each polymer and blend film, five samples were prepared and were annealed at the following temperatures: not annealed, 50, 100, 150, and 200 ^{o}C to see the affect of annealing on the morphology of the polymers.

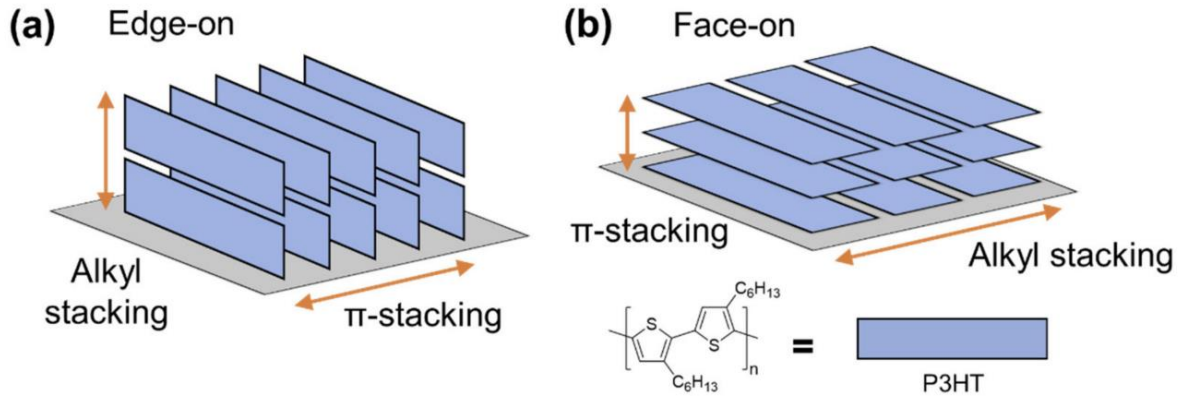

Figure 1-8: a) Edge-on orientation vs. b) Face-on orientation with P3HT as model compound.[47] Reproduced from ref. 47 with permission from author Youngmin Lee, copyright 2021.

Atomic force microscopy (AFM) is a scanning probe method, where attractive forces between the sample and probe tip result in contact between the two surfaces.[48] As seen in **Figure 1-9**, based on the surface influence on the deflection of the probe tip, a topographic image of the surface at the nanoscale is obtained. AFM is an effective method for measuring surface roughness, as well as domain size and phase segregation of the acceptor and donor in OSCs. Surface roughness is quite important in OSCs since there are several layers in contact with each other; smooth films result in better interfaces, which positively effects charge transfer.[49] One important metric obtained from AFM is the rough mean square surface roughness (rms). AFM was not measured for the materials in this thesis but remains a key area of future work.

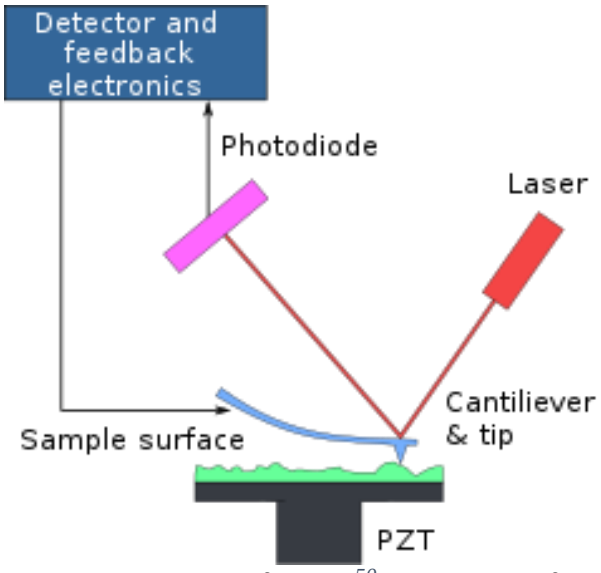

Figure 1-9: Basic operating principle of AFM.[50] Reproduced from ref. 50, Wikipedia.

1.7 Thesis Structure and Objectives

To achieve high performance with NFAs, polymer donor design has targeted D-A donor polymers with low E_{HOMO} levels and wide bandgaps for good energy level matching and complementary absorption. BDT is a commonly used D unit in polymer donor backbones due to its stability, planarity, and electron-donating ability. Therefore, the work detailed in this thesis aimed to synthesize simple thiophene and benzene-based A units to co-polymerise with BDT for novel wide bandgap D-A polymer donor materials with low cost, and relatively low synthetic complexity. These polymers were paired with high performing NFAs including Y6 and IT-4F to assess their performance.

In Chapter 2, a series of polymers were designed and synthesized, with the goal of extending the conjugation into the side chain to effectively polarize the polymers and allow for extended exciton lifetimes. This series used ethynyl bonds to link the side chain to a thiophene, which is co-polymerized with BDT, forming polymers PSETBDT, PBETBDT, and POBETBDT. The thermal, optical, and electrochemical properties were characterized using GPC, TGA, DSC, UV-vis, CV, and PL quenching. PSETBDT was tested with Y6 and IT-4F for OPV performance, while POBETBDT was tested with Y6 for OPV performance. PBETBDT was not tested further due to solubility issues during synthesis. The charge mobilities and film morphology of the neat polymers and blend films were studied using SCLC mobility and XRD, respectively.

In Chapter 3, a second series of polymers was developed with a similar goal of extending the conjugation into the side chain. This series incorporated a triazole ring side chain into the thiophene-BDT structure, with different functionalization to form an alkyl-substituted triazole ring (PTTBDT) and a carbamate-substituted triazole ring (PCTBDT). Both PTTBDT and PCTBDT were blended with Y6 for OPV testing and were characterized similarly to Chapter 2.

In Chapter 4, the focus was on synthesizing a wide bandgap D-A polymer with a simple synthetic route, which effectively lowered the E_{HOMO} level of a benzene-BDT polymer by introducing fluorine groups on the benzene ring. This chapter includes a tetrafluorobenzene-BDT polymer (PFBBDT). This polymer was tested with Y6 as the NFA material in OPV devices and characterized with the same methods as Chapter 2.

In Chapter 5, the focus was on easy synthesis and low-cost materials, where the functionalization could be easily changed via a post polymerization modification. This chapter includes two polymers: an acetal-substituted thiophene-BDT polymer (PATBDT), and a formaldehyde-substituted thiophene-BDT polymer (PXTBDT). The acetal group is easily cleaved by adding a drop of hydrochloric acid (HCl) to a solution of PATBDT in chloroform, forming PXTBDT. Both polymers were tested with Y6 for OPV performance and were characterized using the same techniques as Chapter 2.

Finally, Chapter 6 summarizes the work detailed in this thesis and provides future directions for improving the performance of these polymers.

Chapter 2: Development of BDT-Based Donor Polymers Containing Novel Thiophene Comonomers with Ethynyl Side Chains

2.1 Introduction

For OSCs, considerable research has been conducted developing novel polymer donor materials to pair with commercial NFAs. For good performance, it is critical to have good energy level matching between the polymer donor and NFA, as well as good morphology when in a blended film.[1] The best performing NFA materials, including ITIC, IT-4F, and Y6, have narrow bandgaps; therefore, to achieve complementary absorption a wide bandgap donor is required.[1]

P3HT is a polymer donor that has been extensively studied in this field; however, the high E_{HOMO} results in low V_{oc} and low PCE. Recent research has focused on D-A polymer donors, allowing for tuning of the energy levels and optical bandgaps through monomer design and effective D-A unit pairing.[1] Thiophene moieties are extensively implemented as the D unit due to their good planarity, stability, and electron-donating effect.[1] Specifically, BDT is of interest as a D unit since the fused ring structure provides good hole transport and induces the preferred face-on orientation.[1] Since the inclusion of BDT has resulted in high-performing polymers, the research in this thesis will focus on developing novel A units, which can be co-polymerized with BDT to provide polymers with effective energy level matching with IT-4F and Y6.

There are several important parameters to target when designing effective D-A polymers for OSCs. Overall, it is important to target inexpensive, wide bandgap materials with a low lying E_{HOMO}. To achieve an acceptable E_{HOMO} while minimizing cost, thiophene has been used as the base A unit. Although thiophene on its own is a D unit, the addition of a moderately electron withdrawing group (EWG) can produce an effective A unit.[51] Examples of common EWGs include fluorine, chlorine, esters, trifluoromethyl, and alkoxy groups.[1] However, although the addition of side chains is necessary for lowering the E_{HOMO} and solubility, they inherently increase the amount of twisting in the polymer backbone, which can negatively effect charge carrier mobility.[1] Therefore, side chain engineering is important for minimizing twisting while maintaining good energy levels and solubility.

Our group has previously synthesized polymers: poly(3-(([2,2′:5′,2″-terthiophen]-3-yl-5,5“-diyl)methylene)-1-(2-octyldodecyl)indolin-2-one) (PTIBT)[51] and poly{(4,8-bis(5-(2-ethylhexyl)thiophen-3-yl)benzo[1,2-b:4,5-b']dithiophen-2,6-diyl)-co-[methyl(E)-thiophene-3-acrylate-2,5-diyl] (PBDT-TA)[52], which have incorporated a double bond spacer connecting the EWG side chain to the base unit. The advantage of this double bond connection is the π-conjugation is extended perpendicular to the backbone, resulting in effective polarization of the polymer.[52] Our group has shown that this can increase the dielectric constant, which reduces the exciton binding energy, allowing for longer exciton lifetimes, and ultimately, better performance.[51,52] For example, PBDT-TA with an acrylate (double bond) side chain outperformed a carboxylate equivalent with a PCE of 10.47 % compared with 9.68 %, mainly due to higher J_{sc}.[52] Therefore, this chapter will focus on side chains that extend the π-conjugation to assess the impact on the polymer's properties and performance.

Specifically, in this chapter, a series of ethynyl-substituted thiophene-BDT polymers was investigated. This series of polymers uses triple bonds instead of the previously mentioned double bonds as a π-extender into the side chain to determine if it is an effective design method for D-A polymers. The ethynyl side chain is rigid and should allow for good charge mobility due to good co-planarity, while also increasing the polarization, which could result in high performance materials.

2.2 Polymer Structure Design

To evaluate the effectiveness of the ethynyl series of polymers, different functional groups substituted on a thiophene unit were explored, which were paired with a commercial BDT for co-polymerisation. Initially, a trimethyl silyl side chain was proposed due to its low cost; however, this was a new side chain structure for OSCs, so the performance was unknown. To provide a comparison, two other polymers were proposed with more common side chains in OSC applications: one with a benzene ring and another with a benzene ring and an alkyloxime chain substituted at the para-position. The benzene ring was thought to provide good co-planarity with BDT. The alkyloxime chain was proposed due to solubility concerns with the unsubstituted benzene ring and because in the past our group has demonstrated that the alkyloxime side chain can contribute to high performance.[53] The ethynyl series of polymers are shown in **Figure 2-10** below.

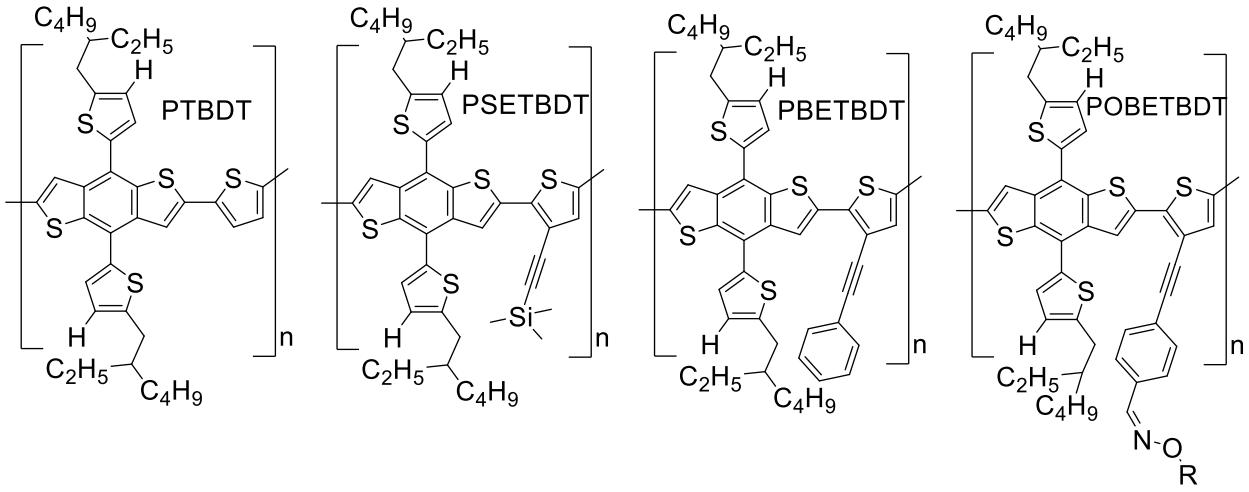

Figure 2-10: Structures of reference polymer (PTBDT), and polymers containing thiophene comonomers with ethynyl side chains (PSETBDT, PBETBDT, and POBETBDT).

2.2.1 Density Functional Theory (DFT) Simulations

To evaluate the proposed polymer structures, DFT was used to provide computational analysis. To assist with the DFT calculations, Avogadro software was used to calculate an initial energy minimization; however, the computation time for this is minutes compared to days for the more sophisticated and accurate DFT software. In Avogadro, the Universal Force Field (UFF) approach was used with the algorithm set as ‘steepest descent’. These files were then input into

Gaussview 6.0.16, which in partnership with Gaussian 09, was used to calculate the DFT outputs. The input into Gaussview to govern the calculation was opt freq b3lyp/6-31g(d) geom=connectivity. Any long alkyl side chains were replaced with a methyl group to minimize the computation time.

DFT is useful for a comparison of the E_{HOMO}, E_{LUMO}, and bandgaps. Since a dimer is being used to represent a polymer, the values obtained from DFT calculations are not quantitatively accurate, rather they provide a basis for comparison between different materials. Therefore, to make a good comparison, a reference structure was simulated, which contained a dimer consisting of BDT and an unsubstituted thiophene (PTBDT). Based on the results, a relative sequence of HOMO energy levels provides insight into the materials that will be best suited for OSCs with Y6 (or IT-4F). Furthermore, from DFT the dihedral angle can be obtained. In comparison with the unsubstituted thiophene dimer, the amount of twisting caused by each side chain can be determined. This information provides insight into whether the polymer can be expected to have good charge transport and morphology. For the purpose of this thesis, DFT is used to provide justification for the potential of these materials but does not guarantee good performance or morphology. The results for each polymer structure can be seen in **Figure 2-11**.

Figure 2-11a shows a dimer of the reference polymer, PTBDT. For the ethynyl polymers, the triple bond EWG side chains show lower E_{HOMO} levels than the reference PTBDT, indicating these polymers could be well suited for pairing with Y6. Particularly, PSETBDT is predicted to have the lowest lying E_{HOMO}, which indicates it could have a high V_{oc}. Furthermore, for PSETBDT, PBETBDT, and POBETBDT, the electrons appear to be evenly delocalized, indicating there could be good charge carrier transfer. Compared with PTBDT, PSETBDT has a 10 degrees larger dihedral angle; however, this angle still provides quite good co-planarity. POBETBDT has a slightly larger dihedral angle of 25 degrees which should be acceptable. PBETBDT is approaching 30 degrees, which means the twisting could have negative effects on the polymerization degree and performance since it limits the ability for π-π stacking.[54] The reference material, PTBDT, has previously been synthesized with a reported E_{HOMO} of -5.27 eV.[55] These polymers, should have lower lying E_{HOMO} levels than this, which is beneficial for energy level matching with NFAs like Y6 for high performance. The results of the DFT calculations are summarized in **Table 2-1** below.

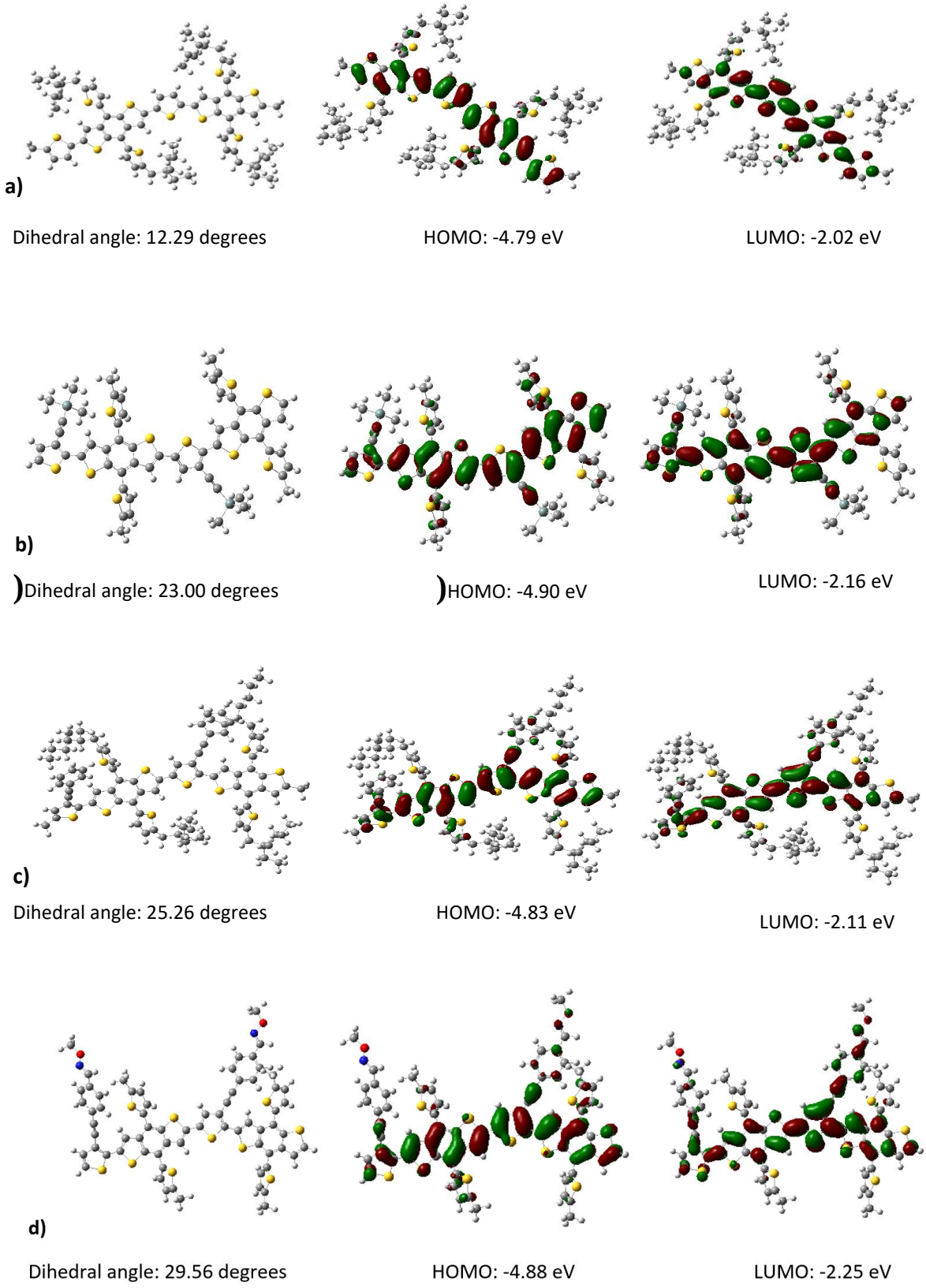

Figure 2-11: DFT calculation results showing overall structure, HOMO, LUMO, and dihedral angle for polymers: a) reference PTBDT; b) PSETBDT; c) PBETBDT; d) POBETBDT.

Table 2-1: DFT results for reference polymer, PTBDT, and proposed polymers PSETBDT, PBETBDT, and POBETBDT.

Polymer	DFT E_{HOMO} (eV)	DFT E_{LUMO} (eV)	DFT Bandgap (eV)	DFT Dihedral Angle (degrees)
PTBDT	-4.79	-2.02	2.77	12.29
PSETBDT	-4.90	-2.16	2.74	23.00
PBETBDT	-4.83	-2.11	2.72	25.26
POBETBDT	-4.88	-2.25	2.63	29.56

2.2.2 Synthesis Scheme

Polymer PSETBDT was synthesized using a 3-step scheme. First, 2,5-dibromothiophene was iodized at the 3-position. Next, a Sonogashira coupling reaction was used to add the trimethyl silyl ethynyl side chain at the 3-position, replacing the iodine.[56] After confirming purity via NMR, a Stille coupling polymerization was performed with a commercial BDT derivative using anhydrous chlorobenzene as the solvent, a catalytic amount of DMF, temperature of 130 ^{o}C, and a catalyst/ligand system of $Pd(PPh_3)_4$. Similarly, PBETBDT was synthesized using the 2,5-dibromo-3-iodothiophene reagent under the same Sonogashira coupling conditions to add phenylacetylene. Less harsh Stille coupling conditions using $Pd_2(dba_3)/P(tol)_3$ at 90 ^{o}C were used to co-polymerize with BDT. POBETBDT followed a similar reaction scheme to PBETBDT, with one additional step before polymerization, which converted an aldehyde chain attached to the benzene ring to an alkyloxime chain. The synthesis overview of these three polymers can be seen in **Scheme 2-1** below and further synthesis details can be found in Section 2.8.3.

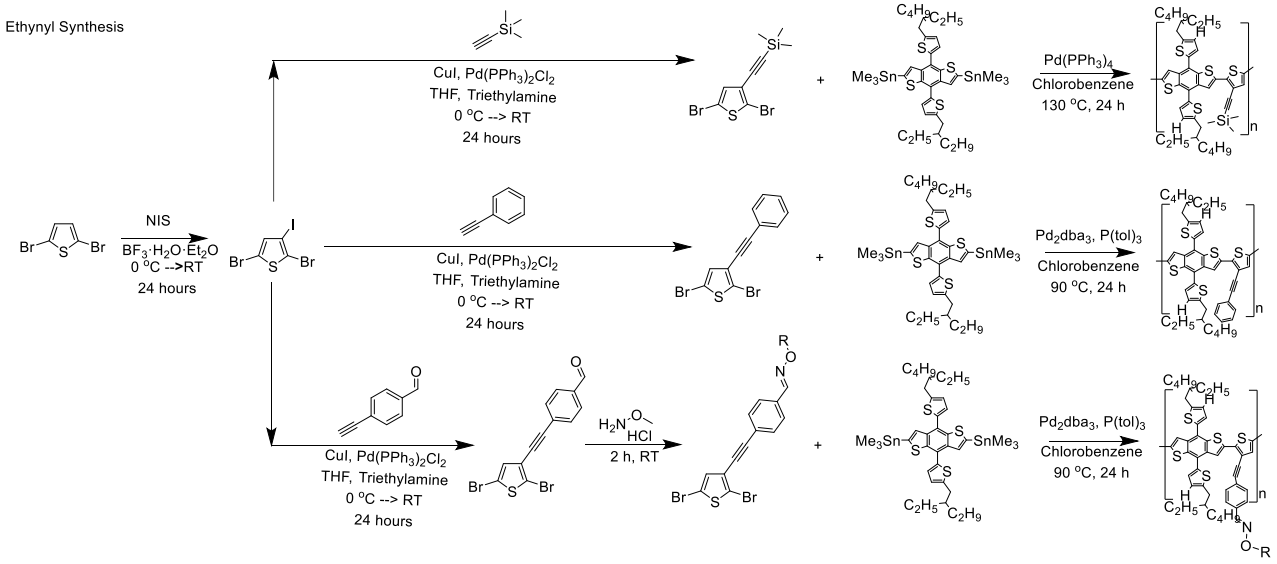

Scheme 2-1: Synthesis scheme for ethynyl polymers: PSETBDT, PBETBDT, and POBETBDT.

2.3 Physical Properties

The molecular weights of the polymers were measured using HT-GPC. Polystyrene was used as a reference, with 1,2,4-trichlorobenzene as the eluent at an operation temperature of 150°. The M_n values were 32.1, 11.2, and 18.1 kDa, whereas the M_w values were 269.6, 30.0, and 49.2 kDa for polymers PSETBDT, PBETBDT, and POBETBDT, respectively. The PDIs were determined to be 8.41, 2.68, and 2.71, respectively. In **Figure 2-12a**, a long tail can be seen at the right edge of the distribution for PSETBDT. The shape of the curve, along with the high M_w and PDI values indicate there is cross-linking.[57,58] Trimethylsilyl is a common protection group for alkynes and can be cleaved with an acid or base. Additionally, a study used a titanium catalyst to selectively cross-couple trimethylsilyl-protected alkynes to form pyrrole derivatives.[59] Potentially, the palladium catalyst can initiate cross-coupling between the ethynyl side chains of subsequent polymer chains through removal of the trimethylsilyl group. Extensive cross-linking is detrimental to organic photovoltaic (OPV) performance due to its effects on charge transport and morphology.[60] Furthermore, many studies show that there is an optimal molecular weight for each polymer, where exceeding this point results in worse performance.[61–63] Some polymers are quite susceptible to significant performance losses if this optimal molecular weight is exceeded.[61] Therefore, the high molecular weight and PDI both could contribute to poor performance for PSETBDT. The low molecular weight of PBETBDT could be detrimental to performance due to negative effects on the active layer morphology and charge transfer. A summary of the GPC data is in ***Table 2-2*** below.

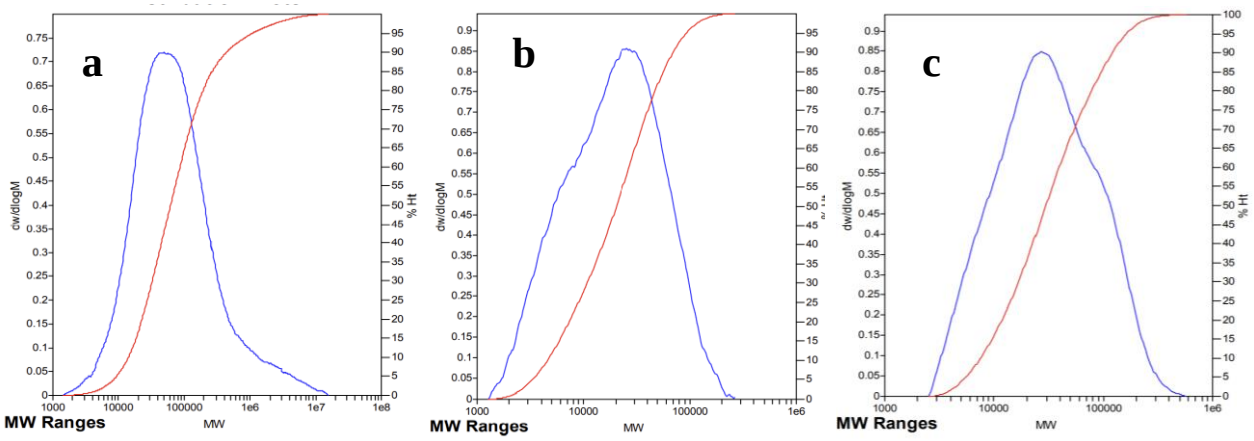

Figure 2-12: HT-GPC molecular weight distribution of polymers: a) PSETBDT; b) PBETBDT; c) POBETBDT.

Table 2-2: HT-GPC molecular weight and polydispersity data summary.

Polymer	M_n (kDa)	M_w (kDa)	PDI
PSETBDT	32.1	269.6	8.41
PBETBDT	11.2	30.0	2.68
POBETBDT	18.1	49.2	2.71

Thermal analysis was conducted using TGA and DSC for thermal stability and information on crystalline transitions, respectively. TGA was acquired using a heating rate of 10 °C/min under nitrogen (see **Figure 2-13**). The ethynyl polymers showed 1 % weight loss at 228, 182, and 270 °C for PSETBDT, PBETBDT, and POBETBDT, respectively. Additionally, the first decomposition step occurred at 356, 231, and 330 °C, respectively. It is suspected that the lower temperatures for PBETBDT are caused by low molecular weight. A second step decomposition for PBETBDT occurs at 335 °C. PSETBDT and POBETBDT show good thermal stability, making them candidates for applications where exposure to high temperatures is possible.

DSC was acquired using a scanning rate of 10 °C/min under nitrogen, where the first cycle went 50 °C lower than the second cycle and the second cycle went until the polymer lost 0.5 % of its weight in TGA (see **Figure 2-14**). All the polymers have a glass transition around 36 °C. Polymers PSETBDT and POBETBDT did not display any additional significant peaks. PBETBDT had a first melting point at 63 °C and a second at 81 °C, which is most likely a result of lower molecular weight. A crystallization peak was observed at 54 °C in the cooling cycle.

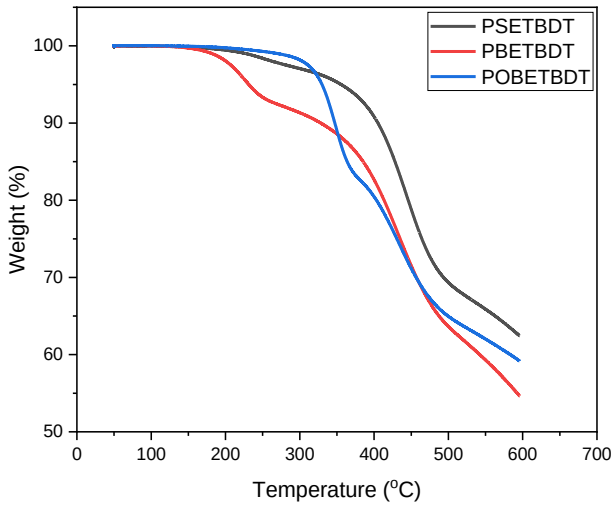

Figure 2-13: TGA curves for polymers: PSETBDT, PBETBDT, and POBETBDT.

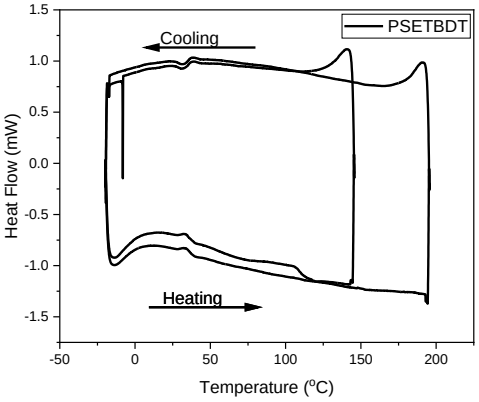

a

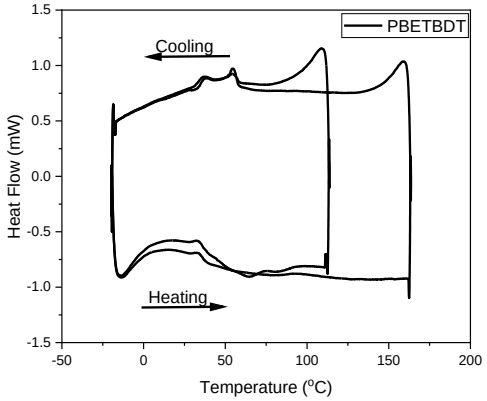

b

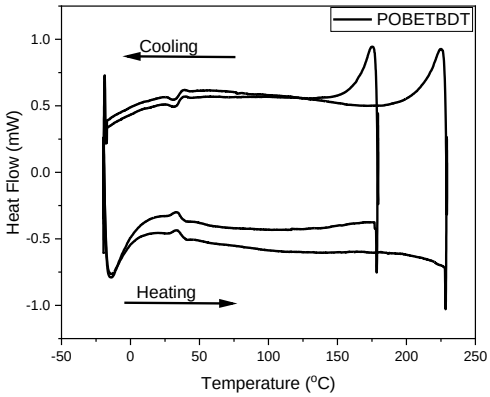

c

Figure 2-14: DSC curves for polymers: a) PSETBDT; b) PBETBDT; c) POBETBDT.

2.4 Opto-Electrochemical Properties

UV-vis absorption spectra were taken for the ethynyl polymers, in both solution and thin film phases (see **Figure 2-16**). A solution of each polymer in chloroform with a concentration of 5 mg/mL was prepared. For the solution spectra, 15 μL of the 5 mg/mL solution was added to 3 mL of chloroform in a cuvette to ensure a maximum absorbance intensity of approximately one was obtained. The thin film samples were prepared by spin coating 50 μL of polymer solution at a speed of 1000 rpm for 60 s. For each polymer, one sample was left at room temperature, and another was annealed at 100 ^{o}C for 20 minutes.

Polymer PSETBDT had a maximum wavelength in solution ($\lambda_{max,s}$) of 508 nm. A red shift to 516 nm was observed from solution to thin film, which indicated more ordered packing of the polymer in solid state. Similarly, polymers PBETBDT and POBETBDT had $\lambda_{max,s}$ values of 531 and 537 nm, which were redshifted to 542 and 549 nm, respectively, for thin films. PBETBDT and POBETBDT showed more clear shoulder peaks than PSETBDT, especially when cast as thin films. The broad shoulder peaks and longer maximum absorbance wavelength for the thin films indicated these polymers have extended backbone conjugation and better planarity than PSETBDT. For all three polymers, there is a slight redshift when the thin film is annealed, indicating a slight improvement on the polymer morphology. From the UV-vis spectra the optical bandgap was obtained by substituting the onset wavelength (λ_{onset}) into **Eq. 7**. The optical bandgaps obtained were 2.05, 1.97, and 1.95 eV, for PSETBDT, PBETBDT, and POBETBDT, respectively. The overall range of absorption makes these polymers ideal candidates to pair with NFAs for complementary absorption.

CV was obtained for each polymer using a solution of acetonitrile with 0.1 M $[n\text{-}Bu_4N]^+[PF_6]^-$ and a scan rate of 0.1 V/s. The solution was bubbled with nitrogen for 2 minutes to deoxygenate. A three-electrode system was used to obtain the measurement with a silver electrode as a reference, a working platinum electrode, and an auxiliary platinum electrode. Using the same 5 mg/mL solution of polymer in chloroform as UV-vis, a polymer thin film was cast on the working electrode by depositing ~5 μL and allowing the chloroform to evaporate.

CV was used to obtain the E_{HOMO} of each polymer by substituting the onset potential into **Eq. 8** (see **Figure 2-17**). The polymers had E_{HOMO} levels of -5.63, -5.55, and -5.51 eV for PSETBDT,

PBETBDT, and POBETBDT, respectively. Interestingly, the low lying E_{HOMO} of PSETBDT indicated that this silicon-based side chain is a relatively strong EWG; however, the high molecular weight of the polymer could also have an effect.[64] The E_{LUMO} level of the polymers was calculated by adding the optical bandgap obtained from UV-vis to the E_{HOMO} obtained from CV since there are no reduction peaks in the CV curves. All the opto-electrochemical information is summarized in **Table 2-3**.

Figure 2-18 shows a comparison between the energy levels obtained from CV and DFT. DFT correctly predicted that PSETBDT would have the lowest lying E_{HOMO} level. However, POBETBDT had a higher E_{HOMO} from CV than PBETBDT, which was opposite of DFT.

Due to the low lying E_{HOMO} of the ethynyl polymers, **Figure 2-15** shows that ITIC does not have well matched energy levels. IT-4F and Y6 are candidates for pairing with these polymers; however, PSETBDT has a similar E_{HOMO} level to these commercial acceptors. Although some polymers have worked well with minimal energy gap with NFAs, further investigation is required.

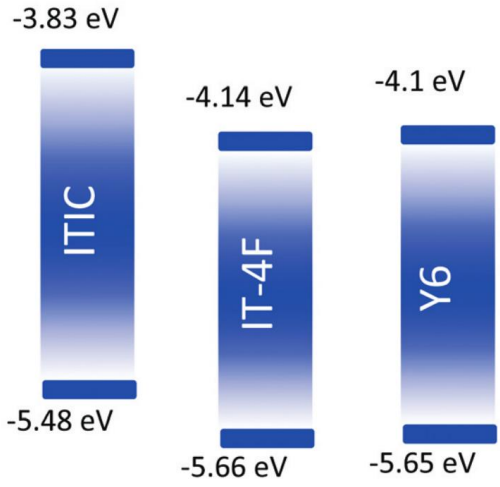

Figure 2-15: Energy diagrams for ITIC, IT-4F, and Y6.[1]

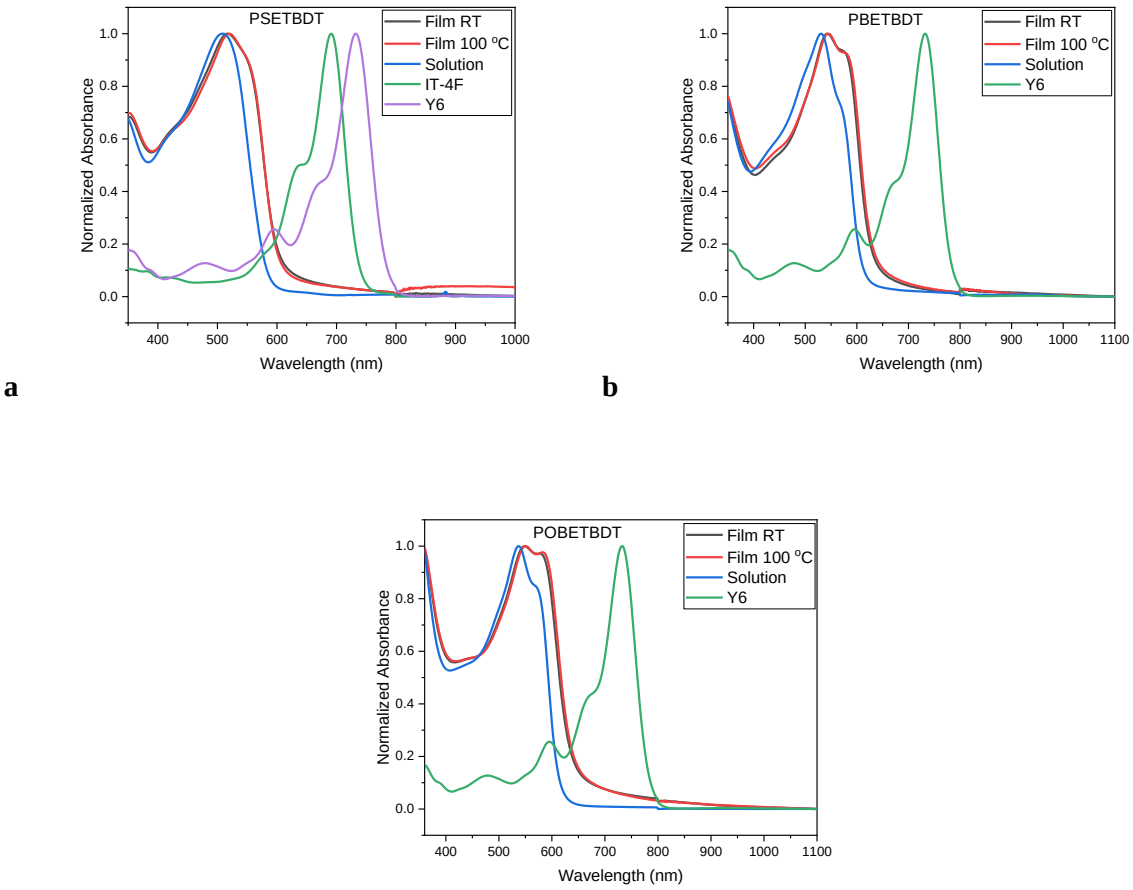

Figure 2-16: UV-vis absorption spectra of as-cast thin film, annealed thin film, and chloroform solution for polymers: a) PSETBDT; b) PBETBDT; c) POBETBDT.

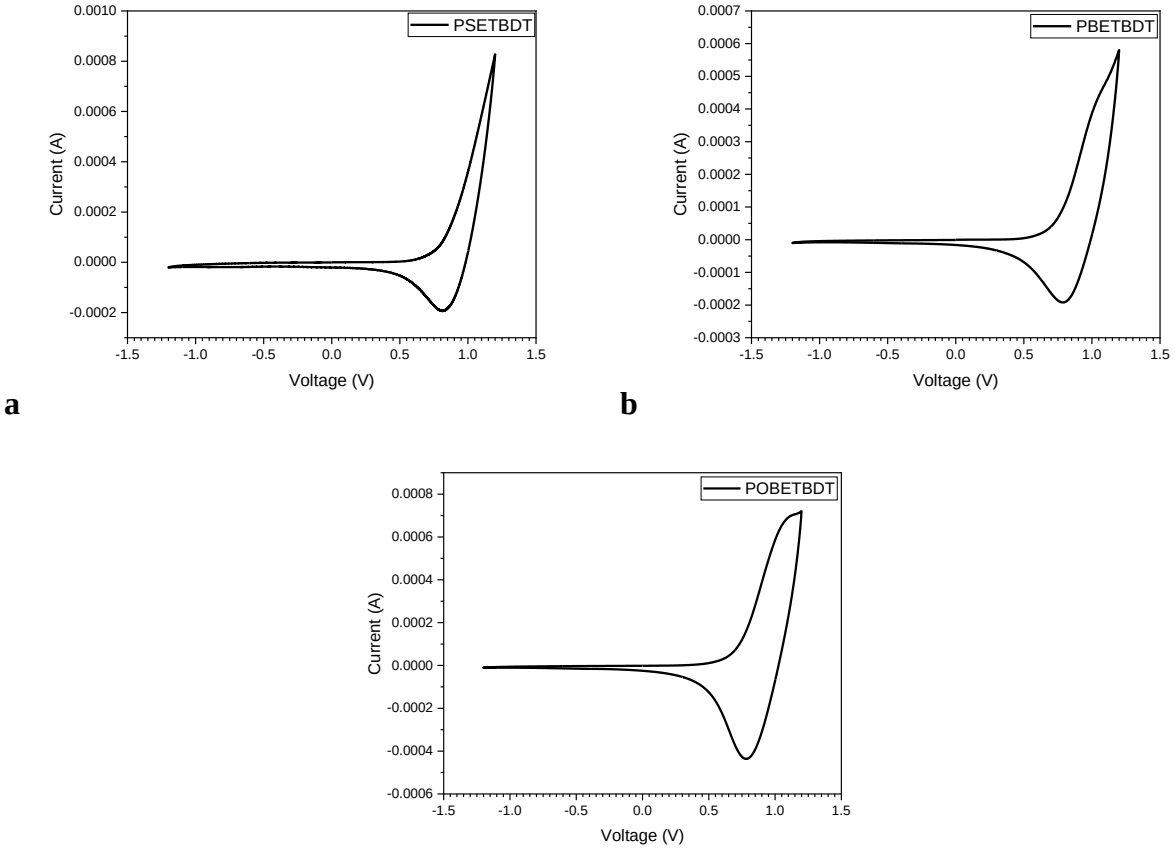

Figure 2-17: CV profiles of polymers: a) PSETBDT; b) PBETBDT; c) POBETBDT.

Table 2-3: Optical and electrochemical properties of polymers: PSETBDT, PBETBDT, and POBETBDT.

Polymer	$\lambda_{max,s}$ (nm)	$\lambda_{max,fRT}$ (nm)	$\lambda_{max,f100C}$ (nm)	λ_{onset} (nm)	E_g^{opt} (eV)	E_{HOMO} (eV)	E_{LUMO} (eV)
PSETBDT	508	516	519	605	2.05	-5.63	-3.58
PBETBDT	531	542	546	630	1.97	-5.55	-3.58
POBETBDT	537	549	550	635	1.95	-5.51	-3.56

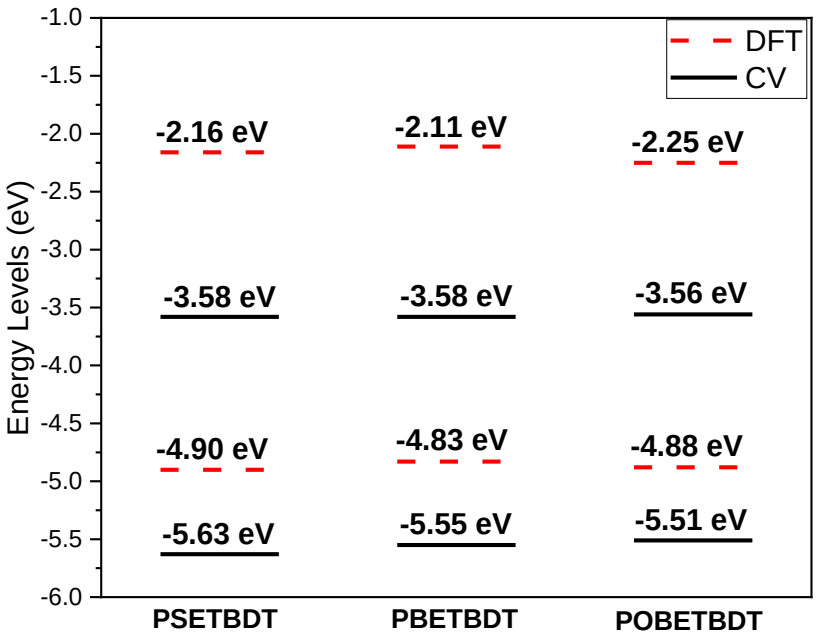

Figure 2-18: Comparison of DFT predicted HOMO and LUMO levels with CV obtained HOMO and LUMO levels for polymers PSETBDT, PBETBDT, and POBETBDT.

There are three extensively studied NFA candidates: ITIC, IT-4F, and Y6, which have achieved high performance OSCs when paired with polymer donor materials. In particular, Y6 has a higher maximum absorption coefficient and narrower bandgap than ITIC and IT-4F.[1] According to the Shockley-Queisser limit, the bandgap of Y6 (1.33 eV) is nearly the ideal value (1.34 eV) for maximizing the PCE of single junction OSCs.[1] These factors have made Y6 a promising acceptor material, which has achieved a PCE of 18.22 % in an OSC BHJ device.[1] For this reason, Y6 was selected as the NFA material to pair with the polymers in this thesis for OPV testing, except for PSETBDT, which was tested with IT-4F and Y6 due to better PL quenching with IT-4F.

PL measurements were used to investigate exciton diffusion and dissociation in the acceptor and donor phases of the blend films (see **Figure 2-19**). To acquire the PL signals, a neat polymer film was excited from its respective $\lambda_{max,RT}$ to 1000 nm. Likewise, a neat Y6 (or IT-4F) film was excited at its respective $\lambda_{max,RT}$ until 1000 nm. Blend films containing equal parts donor and acceptor by weight were prepared and excited at both the polymer $\lambda_{max,RT}$ until 1000 nm and the acceptor $\lambda_{max,RT}$ until 1000 nm. Through integration of the curves and substituting values into **Eq. 10**, the PLQE was calculated. For the blend film, ideally all light is quenched.

For PSETBDT:Y6, in the donor phase excellent quenching occurred (99.8 %); however, 86.9 % was quenched in the acceptor region. Although 86.9 % is not poor, there is room for improvement. For PSETBDT, IT-4F resulted in 99.9 % quenching in both the acceptor and donor regions. For this reason, IT-4F was also selected for OPV testing as an ideal candidate for PSETBDT due to excellent exciton dissociation. PBETBDT showed good quenching with Y6, with 99.9 % in the donor region and 94 % in the acceptor. However, due to the poor synthetic yield of this polymer and the low molecular weight, caused by an insufficient side chain, PBETBDT was not evaluated for OPV performance. PL for POBETBDT and Y6 resulted in good quenching in the acceptor region (96.9 %); however, quite poor quenching in the donor region was observed (71.1 %). Thus, POBETBDT was tested with IT-4F. Although the same quenching (96.9 %) occurred in the acceptor region, worse quenching was observed in the donor region (63.3 %). It is worth noting that POBETBDT had a maximum PL intensity that was one to two magnitudes smaller than the other polymers. This indicated that it may not perform well as an OSC material. The PL results showed that PSETBDT has good exciton dissociation performance with IT-4F and Y6, whereas POBETBDT displays poor exciton dissociation in the donor phase. PBETBDT also shows good quenching with Y6; however, the synthesis must be improved before OPV measurements can be obtained, which is difficult due to the side chain limiting the solubility of the polymer.

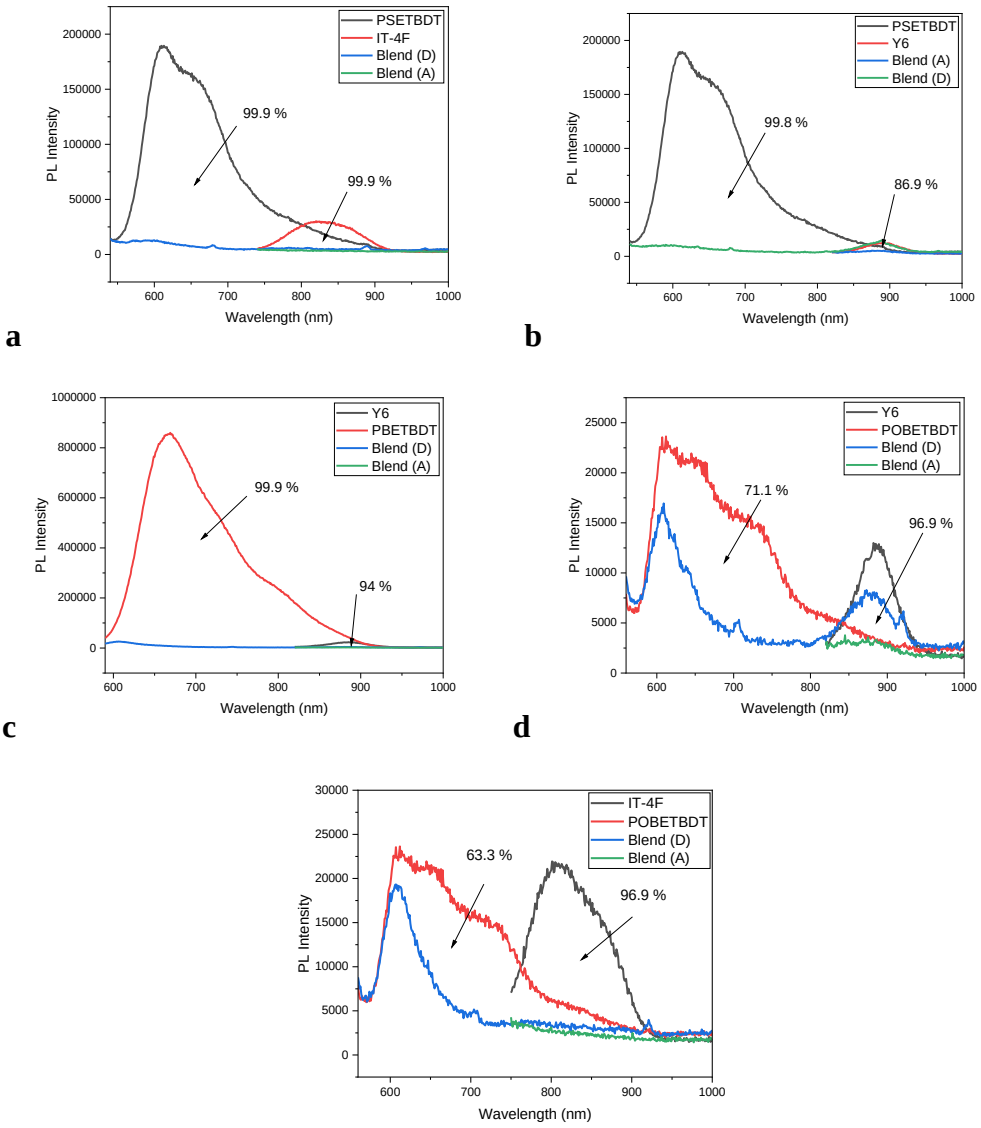

Figure 2-19: PL spectra of a) PSETBDT with IT-4F; b) PSETBDT with Y6; c) PBETBDT with Y6; d) POBETBDT with Y6; e) POBETBDT with IT-4F.

2.5 OPV Performance and Charge Mobility

An inverted structure consisting of the following layers was used for the polymers in this thesis: ITO/ZnO/Active layer/MoO_3/Ag, where the active layer was a BHJ structure, containing a 1:1 donor:acceptor ratio by mass. The electron transport layer, ZnO is deposited via spin coating. The active layer materials are placed in a glovebox under nitrogen, dissolved in chloroform, and mixed, before depositing via spin coating. The hole transport layer and metal electrode are deposited using physical vapour deposition under high vacuum. The OSC devices were characterized under 1 sun illumination (AM 1.5G, 100 mW/cm^2). Further details for sample preparation can be found in Section 2.8.2.

Important note: *Polymer PSETBDT was tested with our previous system. All other polymers were tested with a new ITO pattern and testing system. In the past devices have achieved a FF of 0.56 by Yuan et al. and as high as 0.71 by Jiang et al. in our lab*[52,53]*. Furthermore, a shunt resistance of 883 ohm•cm^2 and a series resistance of 2.84 ohm•cm^2 have been reported by our group*[53]*. However, after switching to the new system, the FF is lower than previously achieved (~0.51 is best achieved currently), which is related to issues with low shunt resistance and high series resistance. This indicates that there is a problem with one or more of the layers and/or interfaces between layers, which is still being investigated by our group. Therefore, the data presented below might not represent the best data possible for these polymers.*

Summaries of the performance of each polymer can be found in **Table 2-4** to **Table 2-9** and a comparison of the best J-V curves for each polymer is shown in **Figure 2-20**. Since PSETBDT was tested with the previous system, the data can be compared to previous standards. PSETBDT was tested with both Y6 and IT-4F because IT-4F showed exceptional PL quenching. With Y6, PSETBDT achieved a highest PCE of 1.44 % (J_{sc} = 6.47 mA/cm^2, V_{oc} = 0.72 V, and FF = 0.31) when annealed at 100 ^oC. Low J_{sc}, V_{oc}, and FF all contribute to the low PCE. The performance improved slightly when the annealing temperature was increased due to increased J_{sc}. As mentioned previously, the high MW and large PDI measured by GPC indicates the polymer is crosslinked, which can negatively affect the charge carrier mobility and morphology of the active layer. This could contribute to the low J_{sc}, FF, and V_{oc}. The high R_s and low R_{sh} indicate there are problems with layer interfaces, which could potentially be due to a rough active layer. When paired with IT-4F, the best cell achieved a PCE of 0.77 % (J_{sc} = 3.67 mA/cm^2, V_{oc} = 0.72 V, and

FF = 0.29) when annealed at 50 °C. Although the PL quenching was better with IT-4F, the PCE was only around half of what was achieved with Y6. The cause of this was a nearly 50 % reduction in J_{sc} and a small reduction in FF as compared with the Y6 devices. The potential cause of this is the superior properties of Y6 (absorption coefficient and slightly smaller bandgap) overcoming the relatively lower PL quenching with PSETBDT compared with IT-4F. Furthermore, lamellar packing ("edge-on") is shown in the XRD with IT-4F (explained later), which is opposite of the desired π-π, "face-on" orientation for OSCs.

POBETBDT was also tested with Y6 and achieved a best performance of 3.65 % (J_{sc} = 15.55 mA/cm^2, V_{oc} = 0.71 V, and FF = 0.33) when annealed at 100 °C. Annealing this polymer resulted in improved J_{sc} and a minor improvement in FF. For POBETBDT, the Jsc is acceptable; however, the V_{oc} and FF are still quite low. Although the E_{HOMO} of POBETBDT is at a good level for matching with Y6 (-5.51 eV), there could be higher voltage losses than the normally assumed 0.5 V empirical losses.[65] Using **Eq. 12**:

$$V_{loss} = \left(E_{LUMO,A} - E_{HOMO,D}\right) - V_{oc} \qquad \boldsymbol{Eq.12}$$

a voltage loss of 0.7 V is calculated for POBETBDT. The additional losses might be due to nongeminate recombination at the D:A interface due to structural defects.[65] From PL, the quenching in the donor phase is relatively low compared to other polymers, reiterating potential recombination issues. Although an alkyloxime side chain has worked well as an EWG by our group in the past, the benzene ring between the backbone and alkyloxime functionalization could negatively affect exciton lifetimes. Voltage losses can also be a result of aggregates or impure domains, and this can also negatively affect the FF, which could contribute to the low performance in this polymer. Overall, the ethynyl polymers did not perform well as OSC devices, indicating the ethynyl side chain structure is not ideal for high OPV performance.

EQE was also measured for the polymers paired with Y6, which provides a ratio of the electrons in the circuit compared to photons in the incident light. This also provides a visual representation of the photocurrent generation efficiency under a range of different wavelengths. PSETBDT achieved a highest EQE at 380 nm and displayed extremely low EQE values at the maximum absorbance wavelengths of PSETBDT and Y6. Polymer POBETBDT achieved a highest EQE of 48 % at 810 nm. **Table 2-10** compares the J_{sc} obtained from OPV and EQE. The values for

PSETBDT have high agreeance (1.33 %). However, POBETBDT had 16.31 % error, which is quite high. This indicates that OPV overestimates J_{sc} and/or EQE underestimates. This error also might relate to the new devices and measurement system. Optimization of this system could reduce the error to an acceptable amount (<10 %), considering with the previous system the percent error was consistently less than 10 %.

Table 2-4: Summary of OSC device parameters for PSETBDT:Y6.

Device	Annealing Temperature (^oC)	RPM	Thickness (nm)
1	No annealing	1000	113.73 (±2.36)
2	No annealing	1500	98.43 (±1.23)
3	No annealing	2000	92.45 (±0.85)
4	50	1000	112.97 (±6.34)
5	50	1500	96.87 (±1.44)
6	50	2000	91.73 (±1.27)
7	100	1000	111.00 (±1.40)
8	100	1500	103.67 (±1.62)
9	100	2000	91.13 (±5.31)

Table 2-5: Summary of OSC performance for PSETBDT:Y6.

Device	Jsc (mA/cm^2)	Voc (V)	FF	PCE (%)	Avg. Rsh ($ohm•cm^2$)	Avg. Rs ($ohm•cm^2$)
1	5.60 (5.42±0.16)	0.71 (0.70±0.01)	0.31 (0.31±0.01)	1.23 (1.15±0.05)	169 (±5)	24.00 (±2.32)
2	5.22 (5.43±0.17)	0.70 (0.66±0.05)	0.32 (0.31±0.01)	1.17 (1.10±0.09)	163 (±20)	16.54 (±3.25)
3	5.92 (5.93±0.01)	0.69 (0.69±0.01)	0.31 (0.31±0)	1.27 (1.26±0.01)	173 (±12)	15.10 (±0.30)
4	5.29 (5.13±0.14)	0.70 (0.70±0.01)	0.32 (0.32±0.01)	1.17 (1.13±0.03)	187 (±6)	19.00 (±0.54)
5	5.99 (5.99±0)	0.70 (0.70±0)	0.31 (0.31±0)	1.29 (1.29±0)	161 (±0)	15.68 (±0)
6	5.88 (5.96±0.14)	0.70 (0.69±0.01)	0.32 (0.31±0.01)	1.31 (1.28±0.04)	160 (±10)	13.00 (±1.05)
7	5.18 (5.05±0.15)	0.70 (0.70±0)	0.32 (0.32±0)	1.16 (1.13±0.03)	191 (±4)	18.35 (±0.70)
8	6.11 (5.83±0.24)	0.70 (0.70±0.01)	0.32 (0.31±0.01)	1.34 (1.27±0.06)	163 (±5)	15.76 (±1.94)
9	6.47 (6.25±0.18)	0.72 (0.69±0.03)	0.31 (0.31±0)	1.44 (1.35±0.07)	156 (±3)	13.86 (±0.91)

Table 2-6: Summary of OSC device parameters for PSETBDT:IT-4F. Note: the thickness of these devices was not tested (aside from device 1) and the values listed are estimates based on the other results obtained.

Device	Annealing Temperature (°C)	RPM	Thickness (nm)
1	No annealing	1000	112.2 (±2.06)
2	No annealing	1500	~100
3	No annealing	2000	~90
4	50	1000	~110
5	50	1500	~100
6	50	2000	~90
7	100	1000	~110
8	100	1500	~100
9	100	2000	~90

Table 2-7: Summary of OSC performance for PSETBDT:IT-4F.

Device	Jsc (mA/cm^2)	Voc (V)	FF	PCE (%)	Avg. Rsh ($ohm \cdot cm^2$)	Avg. Rs ($ohm \cdot cm^2$)
1	3.01 (3.04±0.20)	0.69 (0.66±0.04)	0.29 (0.29±0)	0.59 (0.57±0.03)	112 (±14)	40.69 (±5.21)
2	3.05 (2.90±0.21)	0.73 (0.67±0.06)	0.29 (0.29±0)	0.64 (0.55±0.06)	115 (±14)	45.58 (±11.20)
3	3.78 (3.78±0)	0.68 (0.68±0)	0.29 (0.29±0)	0.75 (0.75±0)	97 (±0)	21.82 (±0)
4	3.20 (3.01±0.13)	0.72 (0.73±0.01)	0.29 (0.29±0)	0.67 (0.64±0.03)	127 (±6)	40.42 (±4.42)
5	3.67 (3.51±0.12)	0.72 (0.70±0.02)	0.29 (0.29±0)	0.77 (0.71±0.05)	106 (±3)	32.09 (±2.79)
6	3.59 (3.26±0.32)	0.70 (0.70±0)	0.29 (0.29±0)	0.73 (0.66±0.08)	128 (±30)	32.41 (±7.24)
7	2.41 (2.17±0.27)	0.74 (0.72±0.01)	0.28 (0.28±0.01)	0.51 (0.44±0.07)	167 (±14)	81.10 (±24.58)
8	3.47 (3.43±0.04)	0.70 (0.70±0)	0.29 (0.30±0.01)	0.70 (0.70±0)	109 (±1)	27.45 (±2.42)
9	3.73 (3.71±0.07)	0.69 (0.64±0.07)	0.29 (0.29±0)	0.75 (0.70±0.06)	92 (±10)	21.48 (±2.62)

Table 2-8: Summary of OSC device parameters for POBETBDT:Y6.

Device	Annealing Temperature (°C)	RPM	Thickness (nm)
1	No annealing	1000	75.65 (±0.45)
2	No annealing	1500	66.55 (±0.35)
3	100	1000	75.75 (±0.85)
4	100	1500	65.55 (±0.45)

Table 2-9: Summary of OSC performance for POBETBDT:Y6.

Device	Jsc (mA/cm^2)	Voc (V)	FF	PCE (%)	Avg. Rsh ($ohm•cm^2$)	Avg. Rs ($ohm•cm^2$)
1	14.43 (14.25±0.36)	0.71 (0.71±0.01)	0.32 (0.32±0.01)	3.27 (3.17±0.08)	100 (±4)	15.98 (±1.20)
2	13.92 (13.87±0.37)	0.71 (0.71±0.02)	0.32 (0.31±0.01)	3.19 (3.08±0.14)	98 (±12)	17.00 (±2.84)
3	15.26 (14.52±0.47)	0.70 (0.68±0.02)	0.33 (0.33±0)	3.51 (3.23±0.17)	112 (±6)	14.58 (±4.41)
4	15.55 (14.70±0.43)	0.71 (0.70±0.03)	0.33 (0.33±0)	3.65 (3.37±0.22)	106 (±18)	15.64 (±2.81)

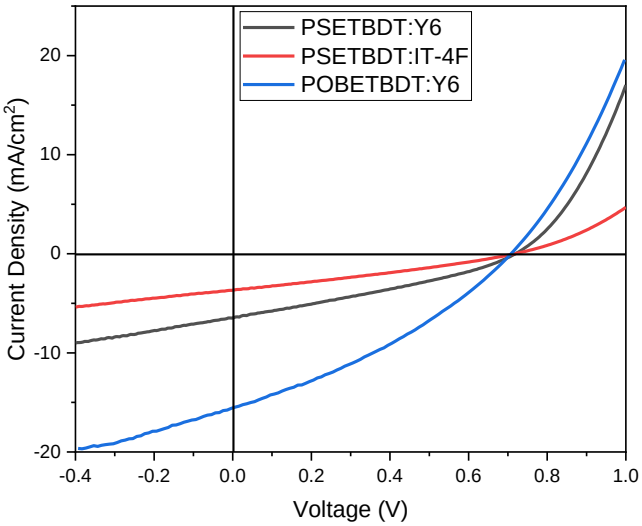

Figure 2-20: J-V curve of PSETBDT:Y6 (100 °C), PSETBDT:IT-4F (50 °C), and POBETBDT:Y6 (100 °C).

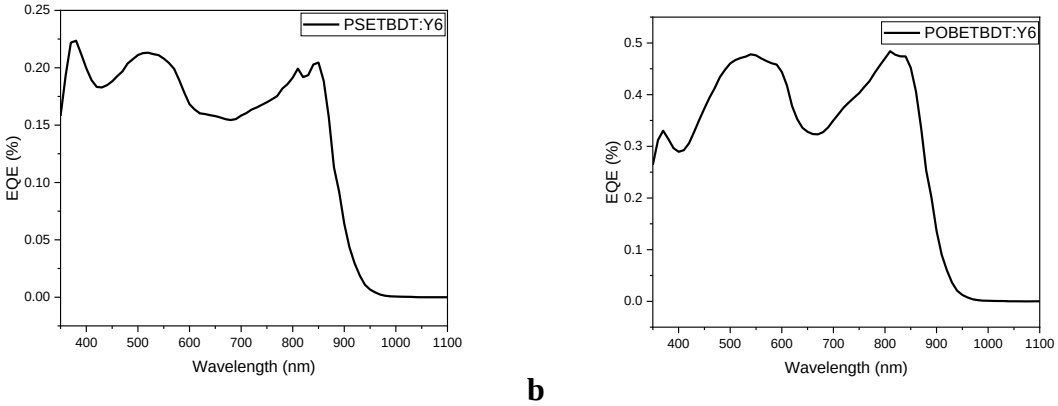

a **b**

Figure 2-21: EQE of best performing OSCs based on a) PSETBDT:Y6; b) POBETBDT:Y6.

Table 2-10: Comparison of Jsc obtained from OPV and EQE measurements for PSETBDT:Y6, and POBETBDT:Y6.

Polymer	Jsc from OPV (mA/cm^2)	Jsc from EQE (mA/cm^2)	Error (%)
PSETBDT	6.11	6.03	1.33
POBETBDT	15.55	13.37	16.31

For further insight into the photovoltaic properties of these polymer donors, the mobility of these materials, both as neat films and blend films, with commercial NFAs must be measured. SCLC is a commonly used technique to measure hole and electron mobility for OSC applications due to its simplicity and ability to measure the vertical mobility using a sandwich structure similar to OPV devices.[66] The hole-only devices are prepared with the following structure: ITO/PEDOT:PSS/active layer/MoO_3/Ag. The electron-only devices are prepared using the following structure: ITO/ZnO/active layer/LiF/Al. SCLC devices were measured under an applied voltage range of 0 to 6 V in the dark. The respective charge carrier mobilities, μ, can be calculated by plotting the natural logarithm of current density versus the natural logarithm of voltage, locating the point where the slope of the curve is 2, and substituting the y-intercept into the rearranged Mott-Gurney equation below:[1]

$$e^{|y-int|} = \frac{9\varepsilon\varepsilon_0\mu}{8l^3} \qquad 13$$

where ε is the dielectric constant of the material (assumed to be 3 for D:A active layer), ε_0 is the vacuum dielectric constant (8.85×10^{-12} F/m), l is the active layer thickness, and μ is the mobility.

Table 2-11 summarizes the calculated hole and electron mobilities, with both the best and average values. For good devices, the SCLC mobility should be greater than 10^{-4} $cm^2V^{-1}s^{-1}$ and the ratio between electron and hole mobilities should be 1.[1] For neat PSETBDT, a good hole mobility of 1.58×10^{-4} $cm^2V^{-1}s^{-1}$ was measured. However, this value sharply decreased when PSETBDT was mixed with Y6 to 2.63×10^{-7} $cm^2V^{-1}s^{-1}$. The electron mobility was poor, with a value of 4.73×10^{-6} $cm^2V^{-1}s^{-1}$, which indicates the charge mobility is quite low and unbalanced. Therefore, this inhibits charge transport, which negatively impacts the J_{sc} and FF. The low mobility and large ratio potentially indicate aggregation occurred. When paired with IT-4F, a much better hole mobility is observed: 7.99×10^{-5} $cm^2V^{-1}s^{-1}$. A similar electron mobility to the

devices with Y6 of $7.87x10^{-5}$ $cm^2V^{-1}s^{-1}$ was observed with IT-4F. This also leads to an unbalanced mobility ratio of ~0.1. Potential causes of this include cross-linking, aggregation, and the lamellar packing discussed in the next section, which is not ideal for vertical charge transport. Polymer POBETBDT showed a good mobility of $1.60x10^{-4}$ $cm^2V^{-1}s^{-1}$ as a neat polymer. However, a decrease to $1.94x10^{-6}$ $cm^2V^{-1}s^{-1}$ is observed when blended with Y6. The electron mobility is $3.87x10^{-6}$ $cm^2V^{-1}s^{-1}$, corresponding to a moderate mobility ratio of 1.99. The low mobility values obtained for POBETDT can limit J_{sc} and FF. The bulky side chain of this polymer might negatively affect the packing, resulting in morphology issues that limit mobility. Furthermore, extensive recombination may occur with this polymer. Since both polymers had good hole mobility as neat films, there are potential issues with mixing, and/or these acceptors might not be suitable candidates for pairing with these polymers. Further investigation into what is causing the drop in mobility is required to determine how to improve the performance of devices based on these polymers.

Table 2-11: SCLC hole and electron mobilities for neat polymers and D:A blend films of PSETBDT, and POBETBDT.

Polymer	μ_e ($x10^{-4}$ $cm^2V^{-1}s^{-1}$)	μ_h ($x10^{-4}$ $cm^2V^{-1}s^{-1}$)	μ_e/μ_h
PSETBDT	N/A	1.58 (1.58)	N/A
PSETBDT:Y6	0.0473 (0.0431)	0.00263 (0.00251)	17.98 (17.17)
PSETBDT:IT-4F	0.787 (0.433)	0.799 (0.687)	0.098 (0.063)
POBETBDT	N/A	1.60 (0.797)	N/A
POBETBDT:Y6	0.0387 (0.0239)	0.0194 (0.00792)	1.99 (3.02)

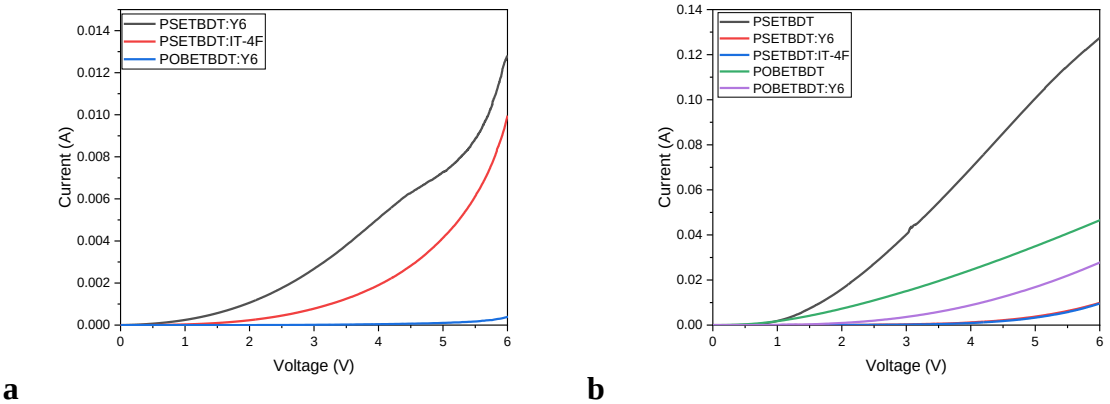

Figure 2-22: a) electron mobility I-V curves for PSETBDT:Y6, PSETBDT:IT-4F, and POBETBDT:Y6; b) hole mobility I-V curves for PSETBDT, PSETBDT:Y6, PSETBDT:IT-4F, POBETBDT, and POBETBDT:Y6.

2.6 Crystallinity

Figure 2-23 shows the 1D and 2D XRD for PSETBDT as a neat polymer and a blend film with IT-4F. As a neat film, there are no obvious peaks observed for the in-plane data; however, a very weak peak appears around $2\theta = 22.37^{o}$ when annealed at 150 ^{o}C. This weak π-π stacking peak appears in both the in-plane and out-of-plane figures for the neat and blend films when annealed at 150 ^{o}C and corresponds to a d-spacing of 0.4 nm. The in-plane blend film showed no other obvious peaks. For the out-of-plane neat and blend films, a peak corresponding to lamellar stacking appears when annealed at temperatures equal to or greater than 100 ^{o}C. For the neat film this occurs at $2\theta = 2.75$ (d = 3.21 nm), which was slightly shifted to $2\theta = 2.62$ (d = 3.37 nm) for the blend film. For the neat film, the lamellar peaks after annealing at 100 and 200 ^{o}C have greater intensity than when annealed at 150 ^{o}C, whereas in the blend film the peak intensity appears to increase with annealing temperature. It appears that the film at 50 ^{o}C is amorphous and could explain why the performance is slightly better when annealed at this temperature since it does not have an edge-on orientation, which is not favoured for OSCs.

The 1D and 2D XRD for POBETBDT as a neat and blend film with Y6 is shown in **Figure 2-24**. Both as a neat polymer and in a blend film, POBETBDT did not show any obvious peaks, and therefore, is an amorphous polymer. This is most likely caused by the bulky side chain consisting of a benzene ring and an ethylhexyl branched alkyl chain.

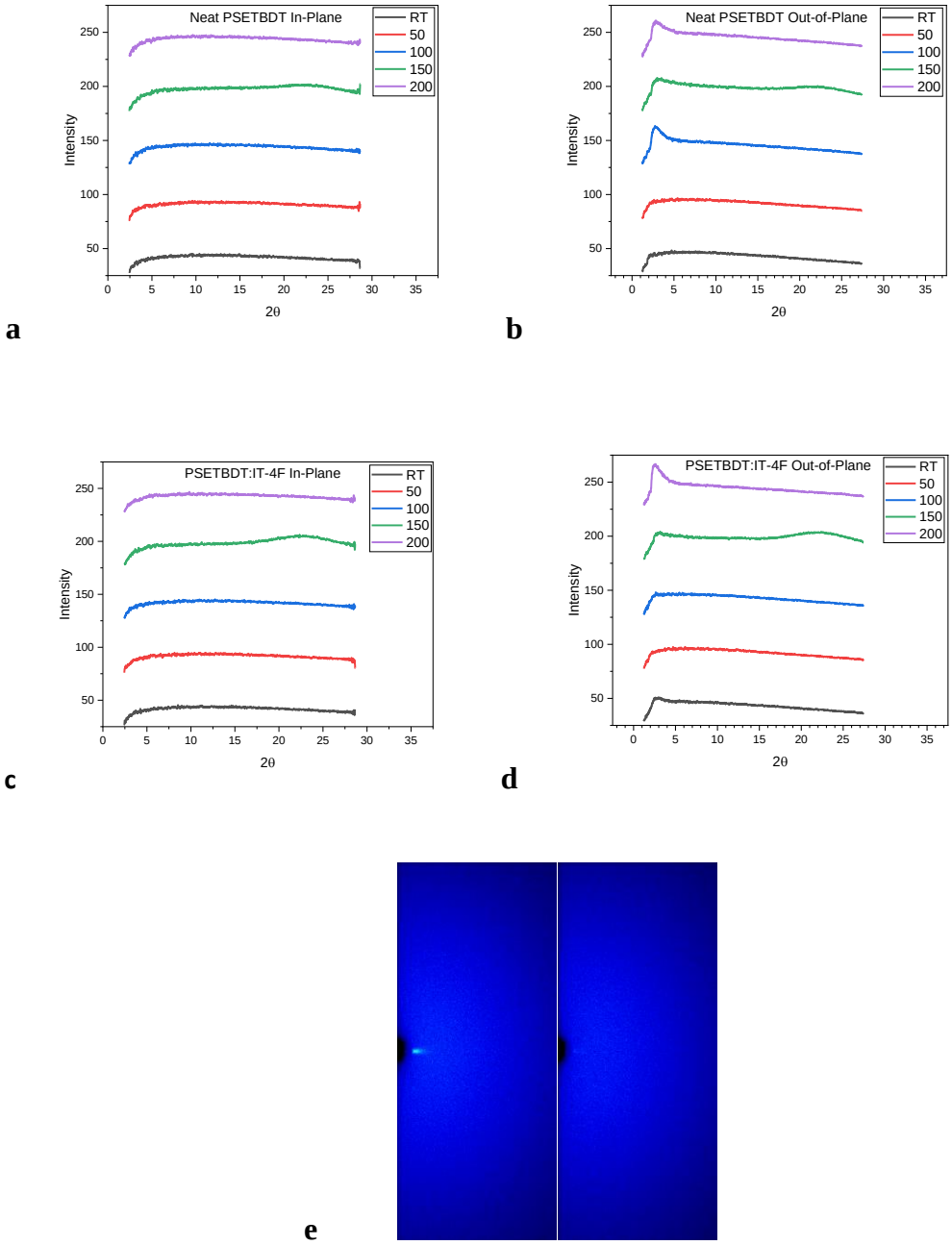

Figure 2-23: GIXD patterns of films at different annealing temperatures: a) in-plane neat PSETBDT; b) out-of-plane neat PSETBDT; c) in-plane PSETBDT:IT-4F blend; d) out-of-plane PSETBDT:IT-4F blend; e) 2D images of the best performing material (annealed at 50 ^{o}C), where the left is neat PSETBDT and the right is PSETBDT:IT-4F.

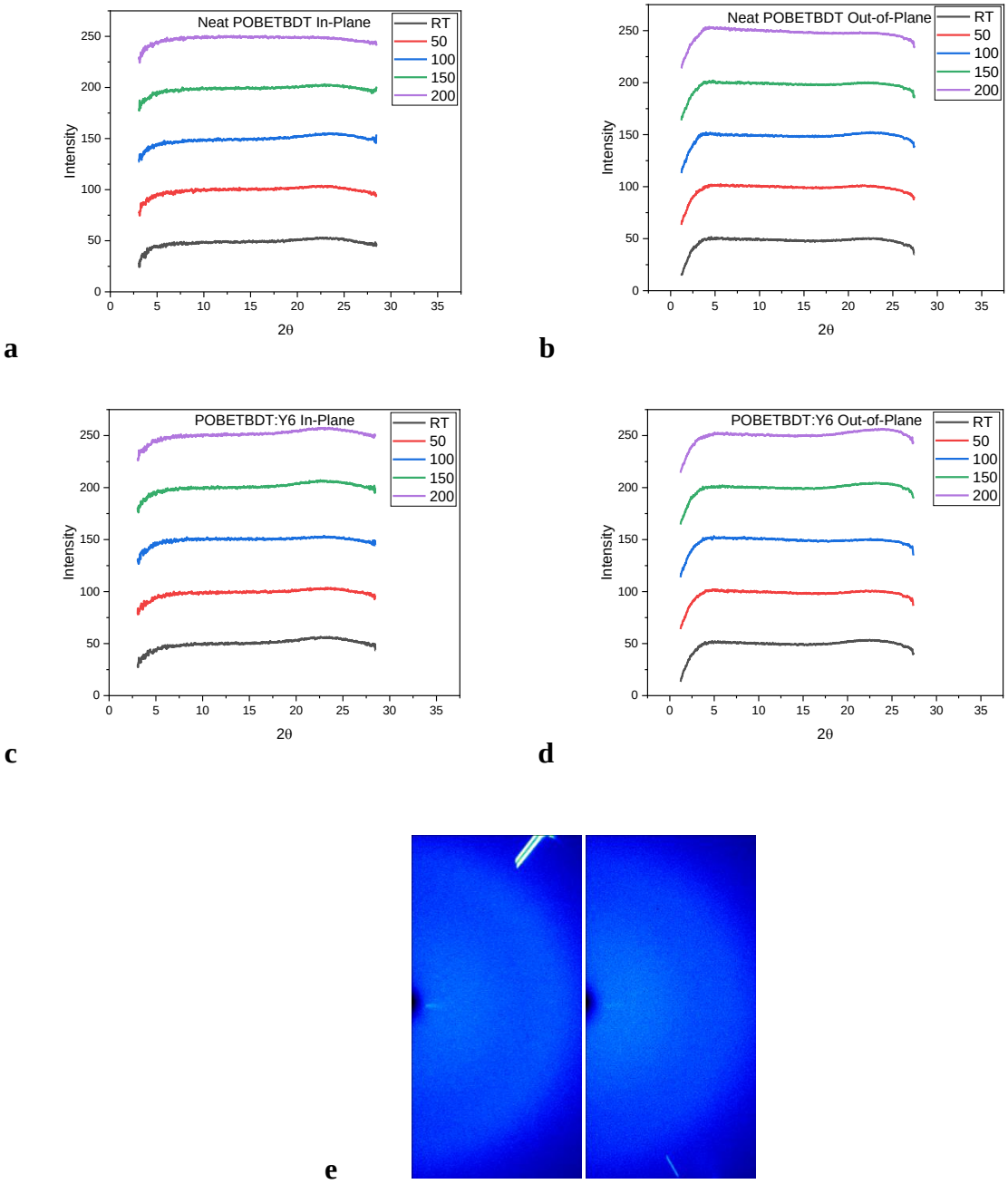

Figure 2-24: GIXD patterns of films at different annealing temperatures: a) in-plane neat POBETBDT; b) out-of-plane neat POBETBDT; c) in-plane POBETBDT:Y6 blend; d) out-of-plane POBETBDT:Y6 blend; e) 2D images of the best performing material (annealed at 100 ^{o}C), where the left is neat POBETBDT and the right is POBETBDT:Y6.

2.7 Summary and Future Direction

In summary, three novel donor polymers were synthesized based on a thiophene-BDT backbone. PSETBDT, PBETBDT, and POBETBDT were synthesized with a trimethyl silyl, benzene, and alkyloxime para-substituted-benzene side chain, respectively, which were all connected to thiophene using an ethynyl bridge. The ethynyl side chains were used to extend the conjugation perpendicular to the backbone and polarize the polymer for good electron-withdrawing capabilities of the A unit in the D-A donor polymer. DFT calculations predicted the side chains would effectively lower the E_{HOMO} level for good energy level matching with NFA materials. GPC results showed a higher M_w and a substantial PDI for PSETBDT, which indicates cross-linking has occurred. All three polymers were thermally stable past 200 ^oC, with wide bandgaps, and low lying E_{HOMO} levels. Due to solubility issues when synthesizing PBETBDT and low molecular weight, it was not tested for OPV performance. Polymer PSETBDT was tested with Y6, achieving a best PCE of 1.44 % (J_{sc} = 6.47 mA/cm^2, V_{oc} = 0.72 V, and FF = 0.31) when annealed at 100 ^oC, while only achieving a PCE of 0.77 % (J_{sc} = 3.67 mA/cm^2, V_{oc} = 0.72 V, and FF = 0.29) when annealed at 50 ^oC with IT-4F. POBETBDT achieved a higher best PCE of 3.65 % (J_{sc} = 15.55 mA/cm^2, V_{oc} = 0.71 V, and FF = 0.33) when annealed at 100 ^oC. PSETBDT showed high SCLC hole mobility as a neat film and with IT-4F; however, the hole mobility was exceptionally low with Y6 (10^{-7} cm^{2}V^{-1}s^{-1}). With both acceptors, the SCLC mobility was unbalanced, which can negatively affect the performance. The suspected crosslinking for PSETBDT can negatively affect charge mobility due to morphological issues. PSETBDT had an edge-on orientation when paired with IT-4F, which is not ideal for vertical charge transfer. POBETBDT had low hole and electron mobility, with a moderate mobility balance. This polymer had an amorphous structure and due to the low mobility and large bulky side chain, the performance was not as high as other polymers synthesized by our group that incorporated an alkyloxime side chain. In terms of OSC D-A polymer donor materials, the use of ethynyl side chains on thiophene was not an effective choice when co-polymerizing with BDT.

For future work, the surface roughness of the active layers can be examined using AFM. AFM can also provide the domain sizes to assess if there are any issues with aggregation that may be limiting the performance. Research into the application of these materials for toxic metal complex detection could be examined since this is an area of opportunity for chemical sensors,

where triple bonds could be a key component for detection.[67,68] For OSC applications, optimization of the active layer (different acceptor, solvent additive, etc.) is necessary to improve the performance of these materials. Furthermore, a different ratio between the donor polymer and NFA could be used to improve the mobility ratio. Finally, to minimize the need for high vacuum deposition, a different hole transfer layer, such as Brilliant Matters BM-HTL-1, could be used, which can be printed, or spin coated onto the substrate.

2.8 Experimental Section

2.8.1 Materials Characterization

The common chemicals and solvents used for synthesis were purchased from commercial vendors including Fluka, Armstrong, Sigma-Aldrich, TCI, and VWR without further purification. For the reactions included in this thesis, anhydrous solvents purchased from Sigma-Aldrich were used. NFAs, Y6 and IT-4F, were purchased from 1-Material. Additionally, 1,1'-[4,8-bis[5-(2-ethylhexyl)-2-thienyl]benzo[1,2-b:4,5-b']dithiophene-2,6-diyl]bis[1,1,1-trimethylstannane] (BDT derivative) was purchased from 1-Material. Specific synthesis details will be shown in Section 2.8.3 below. NMR spectra (^{1}H and ^{13}C) were obtained using $CDCl_3$ as the solvent and a Bruker DPX 300-MHz machine. High temperature-GPC was acquired with an Aligent PL-GPC220 system at a column temperature of 110 ^{o}C using 1,2,4-trichlorobenzene (TCB) as eluent at a flow rate of 1 mL/min and polystyrene as standard. UV-vis data was acquired via a Cary 7000 Universal Measurement Spectrophotometer. Both solution-phase in chloroform and thin film-phase on glass substrates were obtained. CV was obtained using a solution of 0.1 M n-Bu_4NPF_6 in acetonitrile with a CHI600E potentiostat at a sweeping rate of 100 mV/s. The system was purged with nitrogen. The auxiliary and working electrodes were platinum, and Ag/AgCl was used as the reference electrode. For calculations of the polymer energy levels, ferrocene, with an E_{HOMO} of -4.80 eV, was used. PL data was acquired via a Horiba PTI QuantaMaster TM 8000 Series Fluorimeter. Polymer thin film thickness for UV-vis and OSC was verified using an Alpha-Step D-500 Profilometer. XRD measurements were obtained using a Bruker D8 Advance diffractometer with Cu Kα radiation (λ = 0.15418 nm). Dodecyltrichlorosilane modified $SiO_2/p^{++}Si$ substrates were used for spin coating polymer solutions, which were then annealed at different temperatures in a nitrogen-filled glovebox. DSC measurements were obtained using a TA Instruments Q20 Differential Scanning Calorimeter. A scan rate of 10 °C/min for two heating and two cooling cycles in nitrogen was used. TGA was acquired using a TA Instruments TGA Q500 with a heating rate of 10 °C/min under nitrogen and a temperature range of 50 to 600 ^{o}C.

2.8.2 OSC Device Fabrication and Characterization

BHJ OSC devices were fabricated using an inverted structure: ITO/ZnO/Active layer/MoO_3/Ag. This cell structure has ITO as the cathode and Ag as the anode. The ITO glass was commercially obtained from Ossila. Initially, the ITO glass was cleaned using a series of solvents: de-ionized water, acetone, and isopropanol (IPA), which were each sonicated for 20 minutes. After washing, the ITO glass was dried using nitrogen. The substrates were then treated with oxygen plasma for fifteen minutes under vacuum. A ZnO solution was prepared the previous day and stirred overnight. The recipe included 200 mg of zinc acetate dihydrate, mixed with 54 μL of ethanolamine stabilizer, and 2 mL of 2-methoxyethanol. Prior to use, the solution was filtered through a 0.22 μm PTFE filter. The ZnO layer was applied via spin coating, using 2700 rpm and 60 s (~35 nm thick). The ZnO was removed from the top and bottom edge of the ITO glass using a cotton swab with acetone to reveal the electrodes. This layer was annealed at a temperature of 200 ^oC for 1 h. The active layer was then added via spin coating in a nitrogen-filled glovebox. The D-A solution was prepared the previous day and stirred overnight with a concentration of 16 mg/mL (1:1 mass ratio of donor and acceptor – e.g., 8 mg of acceptor and 8 mg of donor in 1 mL of solvent). Before spin coating, the D-A solution was filtered using a 0.22 μm PTFE filter. The spin coating inputs were 60 s, and an acceleration and rpm that varied between 1000 and 2500 to assess different film thicknesses. Some samples were then annealed at different temperatures (50, 100, 150 ^oC) for 10 minutes to assess the affect of annealing temperature on performance. The samples were then loaded into the Angstrom Engineering COVAP physical vapour deposition system to deposit a 10 nm MoO_3 layer (which must be highly pure (>99.9 %)), followed by a 100 nm Ag layer under a vacuum pressure of $1x10^{-7}$ torr. A solar cell I-V test system from Ossila, paired with a Science Tech SLB300-A Solar simulator and a 450 W xenon lamp light source with an AM 1.5 filter, was used to produce I-V curves for the OSC devices. A mask was used to concentrate the light on a known sample area of 0.0256 cm^2.

2.8.3 Synthesis Routes

Synthesis of 2,5-dibromo-3-iodothiophene

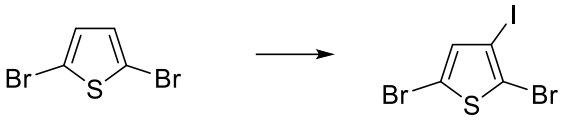

1.1 R:H2O, R:BF3-Et2O, cooled

1.2 R:Iodosuccinimide, 0°C; 0°C → rt; 24 h, rt

To a 25 mL two-neck round bottom flask, N-iodosuccinimide (2.47 g, 11 mmol) was added along with a magnetic stir bar. The reaction system was covered in aluminum foil to eliminate light, purged of oxygen, put under nitrogen, and placed in an ice bath. 2,5-dibromothiophene (2.42 g, 10 mmol) was added to the system. Precooled $BF_3{\cdot}H_2O{\cdot}Et_2O$, prepared from 5 mL $BF_3{\cdot}Et_2O$ and 737 µL of water, was added dropwise to the system. The ice bath was removed, and the reaction mixture was then let to warm to room temperature and stirred for 24 hours. After 24 hours, the reaction mixture was poured into 100 mL of cold water and mixed with 150 mL of diethyl ether. The organic phase was washed with water, sodium thiosulfate solution, saturated sodium bicarbonate solution, and brine, then dried using sodium sulfate. After evaporation of the solvent, the crude product was obtained as a brown oil. This was further purified using a short plug column with pure hexanes as the eluent, where the product was forced through the column using air to avoid decomposition. (Yield: 1.5 g, 41 %). ^{1}H NMR (300 MHz, $CDCl_3$, δ/ppm): 6.91 (s, 1H).[56]

Synthesis of [(2,5-dibromothiophen-3-yl)ethynyl](trimethyl)silane

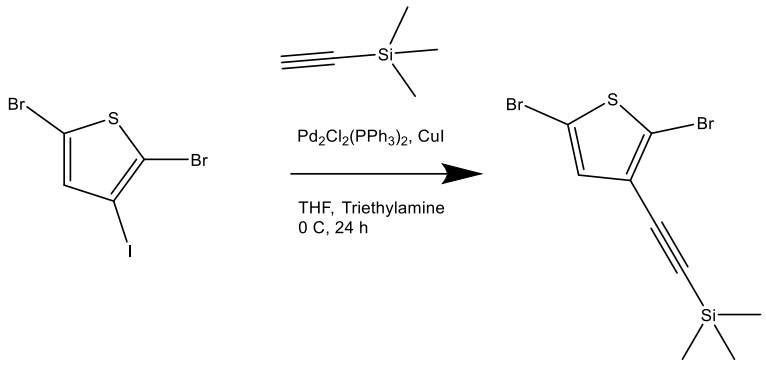

To a 25 mL two-neck round-bottom flask, 2,5-dibromo-3-iodothiophene (1 equiv.) and a catalytic amount of CuI were added, along with a stir bar. The system was placed under nitrogen and vacuumed for three cycles. An ice bath was prepared and used to cool the system to zero degrees. A glove bag was used under nitrogen to measure the palladium catalyst. 1 mL of THF was used to dissolve the catalyst and add to the reaction. The remaining 2 mL of THF and 3 mL of triethylamine was added to the system. Once the total system was cooled, the trimethylsilyl acetylene (1 equiv.) was added dropwise. The reaction was stirred for 24 hours, and the ice was allowed to gradually melt. After stopping the reaction, diethyl ether was used to extract. The organic phase was washed with 1 M HCl, water, saturated sodium bicarbonate solution, and brine. The organic phase was dried with sodium sulfate and then filtered through a Celite plug. The solvent was evaporated, and the product was purified via column chromatography (hexane) to yield a clear liquid. (Yield: 277.4 mg, 80.5 %). ^{1}H NMR (300 MHz, $CDCl_3$, δ/ppm): 6.92 (s, 1H), 0.23 (s, 9H).[69]

Synthesis of [(2,5-dibromothiophen-3-yl)ethynyl]benzene

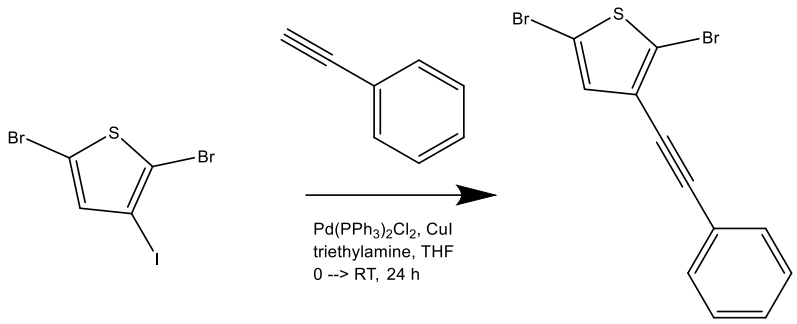

To a 25 mL two-neck round-bottom flask, 2,5-dibromo-3-iodothiophene (1 equiv.) and a catalytic amount of CuI were added along with a stir bar. The system was placed under nitrogen and vacuumed for three cycles. An ice bath was prepared and used to cool the system to zero degrees. A glove bag was used under nitrogen to measure the palladium catalyst. 1 mL of THF was used to dissolve the catalyst and add to the reaction. The remaining 2 mL of THF and 3 mL of triethylamine was added to the system. Once the total system was cooled, the phenylacetylene (1 equiv.) was added dropwise. The reaction was stirred for 24 hours, and the ice was allowed to gradually melt. After stopping the reaction, diethyl ether was used to extract. The organic phase was washed with 1 M HCl, water, saturated sodium bicarbonate solution, and brine. The organic phase was dried with sodium sulfate and then filtered through a Celite plug. The solvent was evaporated, and the product was purified via column chromatography (hexane) to yield a clear liquid. (Yield: 223.9 mg, 74 %). ^{1}H NMR (300 MHz, $CDCl_3$, δ/ppm): 7.51 (m, 2H), 7.35 (m, 3H), 7.0 (s, 1H).[69]

Synthesis of [(2,5-dibromothiophen-3-yl)ethynyl]benzaldehyde

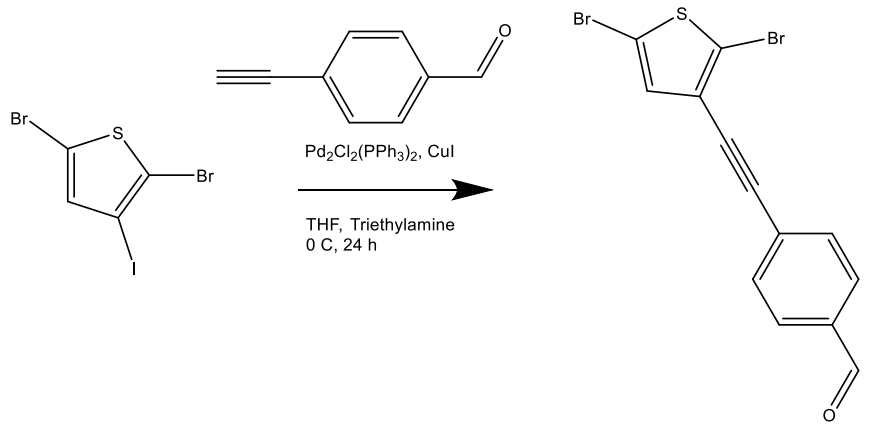

To a 25 mL two-neck round-bottom flask, 2,5-dibromo-3-iodothiophene (1 equiv.) and a catalytic amount of CuI were added along with a stir bar. The system was placed under nitrogen and vacuumed for three cycles. An ice bath was prepared and used to cool the system to zero degrees. A glove bag was used under nitrogen to measure the palladium catalyst. 1 mL of THF was used to dissolve the catalyst and add to the reaction. The remaining 2 mL of THF and 3 mL of triethylamine was added to the system. Once the total system was cooled, the 4-ethynylbenzaldehyde (1 equiv.) was added dropwise. The reaction was stirred for 24 hours, and the ice was allowed to gradually melt. After stopping the reaction, diethyl ether was used to extract. The organic phase was washed with 1 M HCl, water, saturated sodium bicarbonate solution, and brine. The organic phase was dried with sodium sulfate and then filtered through a Celite plug. The solvent was evaporated, and the product was purified via column chromatography (hexane) to yield a clear liquid. (Yield: 284.5 mg, 74.6 %). ^{1}H NMR (300 MHz, $CDCl_3$, δ/ppm): 10.01 (s, 1H), 7.87 (d, 2H), 7.68 (d, 2H), 7.02 (s, 1H).[69]

Synthesis of [(2,5-dibromothiophen-3-yl)ethynyl](2-ethylhexyl oxime)benzene

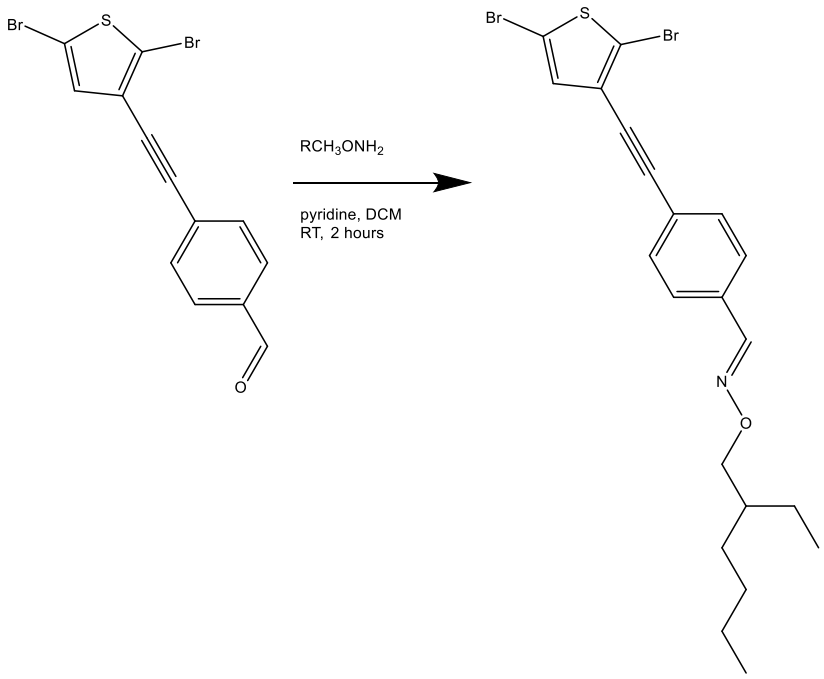

To a 25 mL two-neck round-bottom flask, 2,5-dibromo-3-formaldehyde benzene ethynyl thiophene (1 equiv.) was added to a solution of ethylhexyloxyamine hydrochloride (1.2 equiv.) and pyridine (4 equiv.) in DCM. The reaction was stirred for 2 hours at room temperature. The solvent was evaporated using the rotary evaporator. The remaining residue was dissolved in a minimal amount of DCM and purified via a column in 50:50 DCM:hexanes. (Yield: 284.5 mg, 74.6 %). ^{1}H NMR (300 MHz, $CDCl_3$, δ/ppm): 8.04 (s, 1H), 7.56 (q, 4H), 7.00 (s, 1H), 4.09 (d, 2H), 1.7 (m, 1H), 1.31 (m, 8H), 0.89 (m, 6H).[70]

Synthesis of polymer PSETBDT

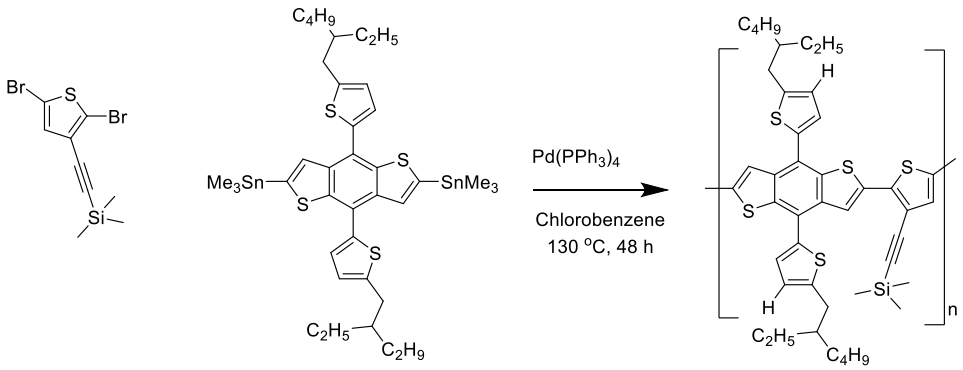

The monomer (1 equiv.) and 1,1'-[4,8-bis[5-(2-ethylhexyl)-2-thienyl]benzo[1,2-b:4,5-b']dithiophene-2,6-diyl]bis[1,1,1-trimethylstannane] (BDT) (1 equiv.) were added to a 2-neck 25 mL round-bottom flask with a small stir bar. The system was purged with argon by performing 3 vacuum cycles. Anhydrous chlorobenzene was added (4 mL). Tetrakis(triphenylphosphine)palladium(0) catalyst ($Pd(PPh_3)_4$) (0.04 equiv.) was measured in an inert atmosphere such as a nitrogen filled glove bag. A 1 mL solution of the catalyst dissolved in chlorobenzene was prepared and added to the flask. 2 drops of DMF were added to the system. The reaction was set at 130 ^oC for 48 hours. After completion, the reaction contents were cooled to room temperature and then stirred in 150 mL of methanol for 30 minutes to an hour. The solid was collected via vacuum filtration and then washed with solvents in the following order: acetone, hexane, chloroform, and chlorobenzene in a Soxhlet extractor. (Yield: 92.2 mg, 70.4 % in chloroform).

Synthesis of polymer PBETBDT

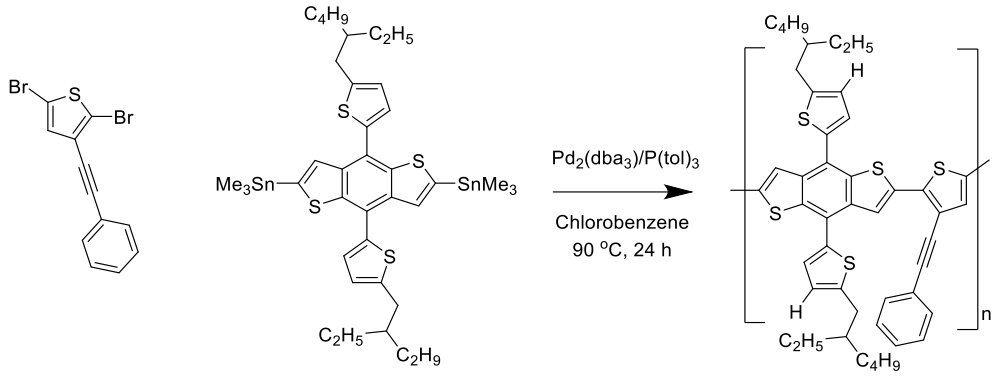

The monomer (1 equiv.), tri(o-tolyl)phosphine ((P(tol)$_3$) (0.08 equiv.), and 1,1'-[4,8-bis[5-(2-ethylhexyl)-2-thienyl]benzo[1,2-b:4,5-b']dithiophene-2,6-diyl]bis[1,1,1-trimethylstannane] BDT (1 equiv.) were added to a 2-neck 25 mL round-bottom flask with a small stir bar. The system was purged with argon by performing 3 vacuum cycles. Anhydrous chlorobenzene was added (4 mL). Tris(dibenzylideneacetone)dipalladium(0) catalyst (Pd_2dba_3) (0.04 equiv.) was measured in an inert atmosphere such as a nitrogen filled glove bag. A 1 mL solution of the catalyst dissolved in chlorobenzene was prepared and added to the flask. The reaction was set at 90 ^oC for 24 hours. After, the reaction vessel was cooled to room temperature and the contents were stirred in 150 mL of methanol for 30 minutes or an hour. The solid was collected via vacuum filtration and then washed with solvents in the following order: acetone, hexane, chloroform, and chlorobenzene in a Soxhlet extractor. (Yield: 27.6 mg, 23 % in chloroform).

Synthesis of polymer POBETBDT

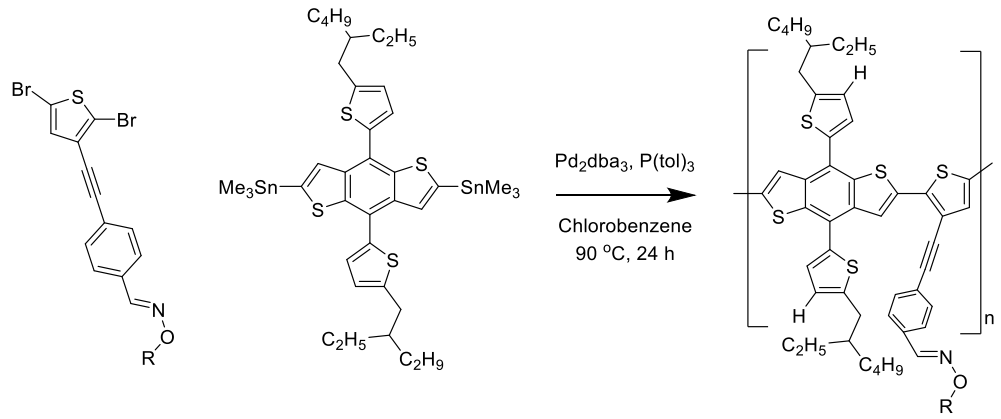

The monomer (1 equiv.), tri(o-tolyl)phosphine ($(P(tol)_3$) (0.08 equiv.), and 1,1'-[4,8-bis[5-(2-ethylhexyl)-2-thienyl]benzo[1,2-b:4,5-b']dithiophene-2,6-diyl]bis[1,1,1-trimethylstannane] BDT (1 equiv.) were added to a 2-neck 25 mL round-bottom flask with a small stir bar. The system was purged with argon by performing 3 vacuum cycles. Anhydrous chlorobenzene was added (4 mL). Tris(dibenzylideneacetone)dipalladium(0) catalyst (Pd_2dba_3) (0.04 equiv.) was measured in an inert atmosphere such as a nitrogen filled glove bag. A 1 mL solution of the catalyst dissolved in chlorobenzene was prepared and added to the flask. The reaction was set at 90 ^oC for 24 hours. After, the reaction vessel was cooled to room temperature and the contents were stirred in 150 mL of methanol for 30 minutes or an hour. The solid was collected via vacuum filtration and then washed with solvents in the following order: acetone, hexane, chloroform, and chlorobenzene in a Soxhlet extractor. (Yield: 78.4 mg, 65.3 % in chloroform).

Chapter 3: Development of BDT-Based Donor Polymers Containing Novel Thiophene Comonomers with Triazole Side Chains

3.1 Introduction

Due to various stability, mobility, and morphological issues with the ethynyl series, poor performance was obtained. However, as previously mentioned, our group has synthesized polymers PTIBT and PBDT-TA, which have shown that double bonds can effectively extend the conjugation into the side chain, polarizing the polymers, and enhancing the performance.[51,52]

The discovery of click chemistry by Sharpless et al. has resulted in many opportunities to expand chemistry methods through simple, near quantitative yield reactions.[71] One application of click chemistry is to convert triple bonds into heterocyclic rings.[71] Specifically, several materials have been developed using a triazole ring for dye-sensitized solar cells, which involves a reaction between an azide and a triple bond, resulting in a five-membered ring consisting of two carbons and three nitrogen atoms.[72–74] This triazole ring has three potential benefits: 1) the nitrogen atoms act as an EWG, where a side chain can be attached to one of these atoms to stabilize the ring; 2) the ring can allow for good co-planarity with BDT; 3) the carbon-carbon double bond extends the π-conjugation.

Overall, the work in this thesis targets easy synthesis routes for low-cost D-A polymer donors that have wide bandgaps and low lying E_{HOMO} levels to effectively pair with high performance NFAs like Y6. An alternative synthesis route uses 3-carboxaldehyde to react an azide with the carbonyl to form a triazole ring. This method results in lower cost starting materials and fewer synthetic steps than if the trimethylsilyl group from Chapter 2 was cleaved to react the ethynyl group with an azide through click chemistry. Therefore, this chapter will also investigate a click chemistry-inspired strategy for extending the π-conjugation of the polymer through triazole ring side chain formation. This structure has the potential to increase charge transport and allow for good morphology. Since BDT is a well-studied D unit that has achieved good performance, triazole-substituted thiophene A units will be co-polymerized with BDT to form novel D-A polymer donors.

3.2 Polymer Structure Design

For the triazole series, two structures were proposed: one with an alkyl chain substituted at the middle nitrogen and another with a carbamate chain substituted at the middle nitrogen. The middle nitrogen substitution was desired to minimize steric effects of the side chains. Carbamate chains are thermally removable groups that have been used in our group to try to produce green solvent soluble polymers; however, for the purpose of this work, the higher polarity compared to an alkyl chain is why carbamate was selected.[75] The triazole series of polymers are shown in **Figure 3-25** below.

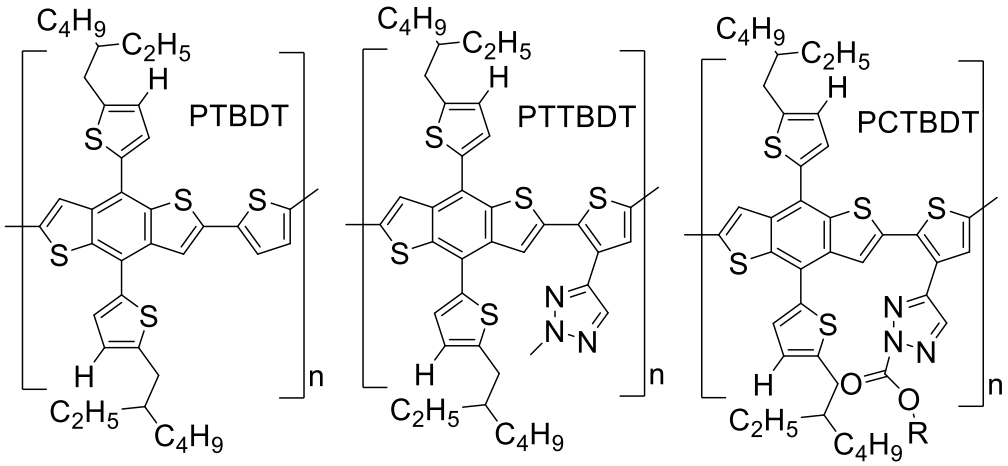

Figure 3-25: Reference polymer (PTBDT) and proposed triazole-substituted thiophene-BDT polymer structures (PTTBDT and PCTBDT).

3.2.1 Density Functional Theory (DFT) Simulations

Like Chapter 2, DFT was used as a tool to assess the relative energy levels to determine the proposed polymers' potential for OSCs, along with their dihedral angles. The same process was used for calculating DFT: Avogadro software for the initial energy minimization estimate, and Gaussian software for the DFT calculation, using the same settings: opt freq b3lyp/6-31g(d) geom=connectivity.

The unsubstituted dimer, PTBDT, was used as a reference for comparing the proposed polymers. The triazole polymers, PTTBDT and PCTBDT, are predicted to have lower lying E_{HOMO} levels than the ethynyl series, which could lead to improved V_{oc}. However, it is worth noting that the triazole polymers are predicted to have larger optical bandgaps, which indicates a smaller range of light will be absorbed by these polymers. Furthermore, the triazole polymers, especially PTTBDT, are predicted to be quite twisted, with angles of 47.78 and 33.25 degrees for PTTBDT

and PCTBDT, respectively. This could negatively affect the charge transport capabilities of these materials since it limits the ability for π-π orbitals to overlap. The reference material, PTBDT, has previously been synthesized with a reported E_{HOMO} of -5.27 eV, which means these polymers should have lower lying E_{HOMO} levels.[55] This will be beneficial for energy level matching with NFAs like Y6 for high performance. The results of the DFT calculations are summarized in **Table 3-12** below.

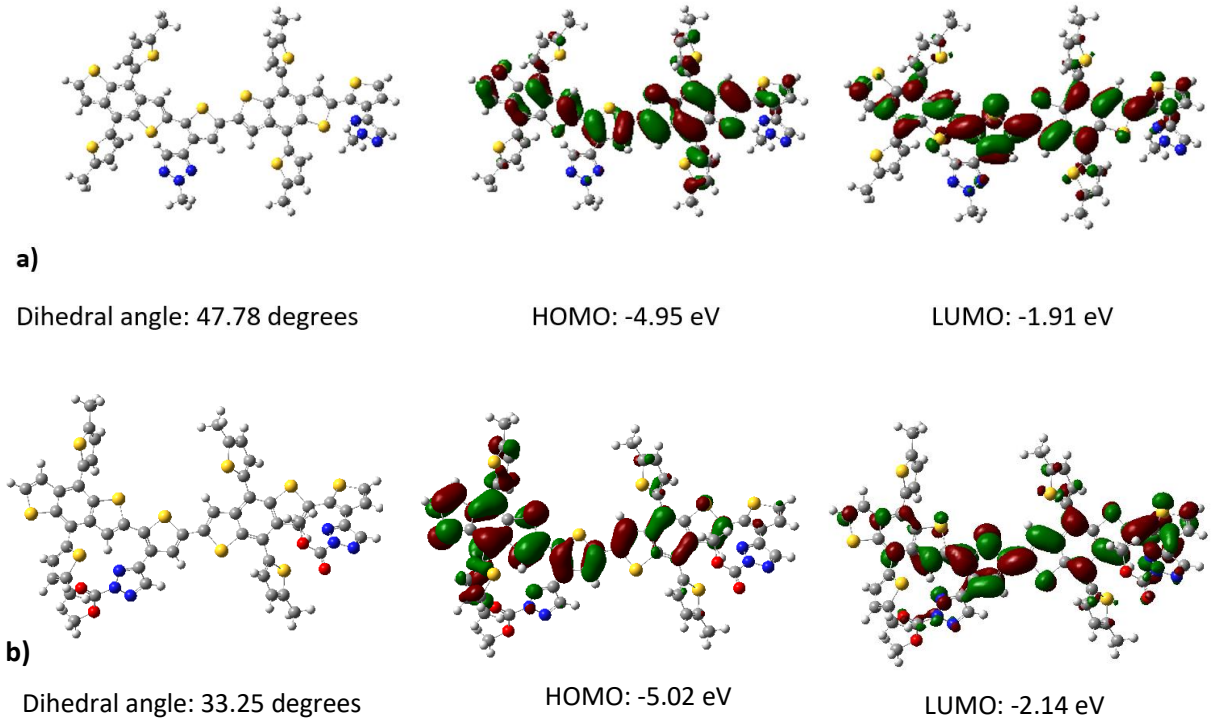

Figure 3-26: DFT calculation results showing overall structure, HOMO, LUMO, and dihedral angle for polymers: a) PTTBDT; b) PCTBDT.

Table 3-12: DFT results for reference polymer, PTBDT, and proposed polymers PTTBDT, and PCTBDT.

Polymer	DFT E_{HOMO} (eV)	DFT E_{LUMO} (eV)	DFT Bandgap (eV)	DFT Dihedral Angle (degrees)
PTBDT	-4.79	-2.02	2.77	12.29
PTTBDT	-4.95	-1.91	3.04	47.78
PCTBDT	-5.02	-2.14	2.88	33.25

3.2.2 Synthesis Scheme

Although polymer PTTBDT could be synthesized by cleaving the trimethylsilyl group (from Chapter 2) and reacting at the triple bond, a different path was developed to minimize the number of synthetic steps and cost. This reaction scheme began with 3-thiophenecarboxaldehyde. The initial step was where sodium azide was reacted with the aldehyde to form a triazole ring.[76] This ring was not stable due to the hydrogen attached to one of the nitrogen atoms. Therefore, the subsequent alkylation step resulted in three isomers; however, only one isomer could be isolated (middle nitrogen substitution).[77] The centre position was favourable since it would cause minimal steric repulsion when polymerized with BDT. Before polymerisation, a bromination reaction using N-bromosuccinimide (NBS) was done. The polymerisation followed the same Stille coupling method mentioned previously for PBETBDT and POBETBDT. PCTBDT was synthesized in a similar fashion. However, for the addition of the carbamate chain, the reaction was conducted at a lower temperature for a longer time to avoid thermal cleavage of this side chain. The other steps of the synthesis were the same as for PTTBDT. The synthesis overview of these two polymers can be seen in **Scheme 3-2** below and further synthesis details can be found in Section 3.8.3.

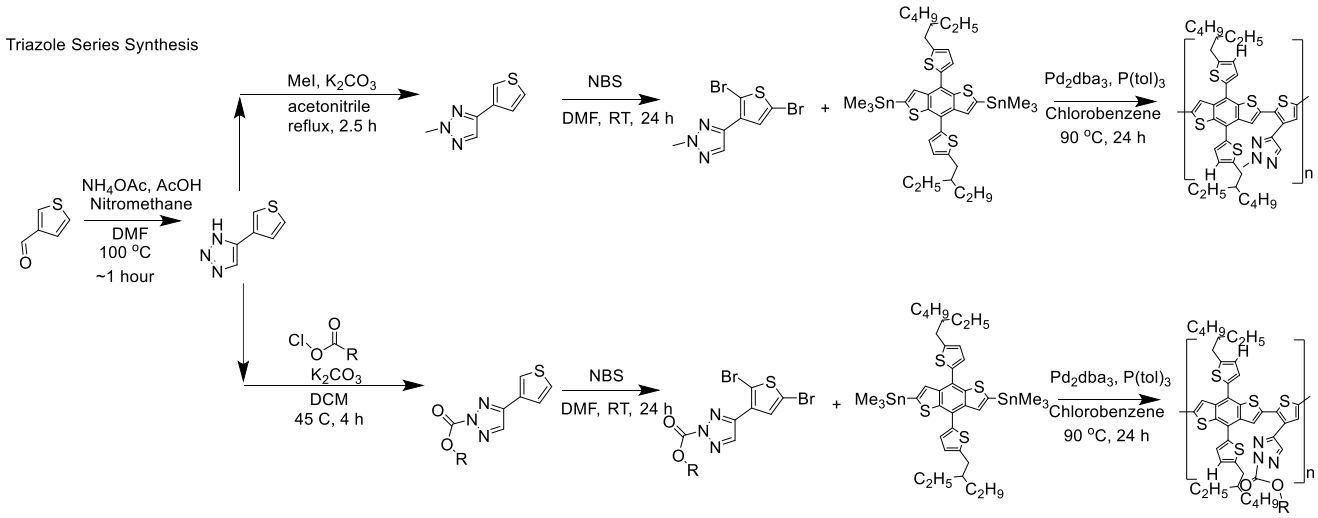

Scheme 3-2: Synthesis scheme for triazole polymers: PTTBDT, and PCTBDT.

3.3 Physical Properties

The molecular weights of the polymers were measured using HT-GPC. Polystyrene was used as a reference, with 1,2,4-trichlorobenzene as the eluent at an operation temperature of 150°. The M_n values were 18.8, and 17.5 kDa, whereas the M_w values were 50.0, and 46.7 kDa for PTTBDT and PCTBDT, respectively. The PDI are 2.66, and 2.70, respectively. A summary of the GPC data is in **Table 3-13** below.

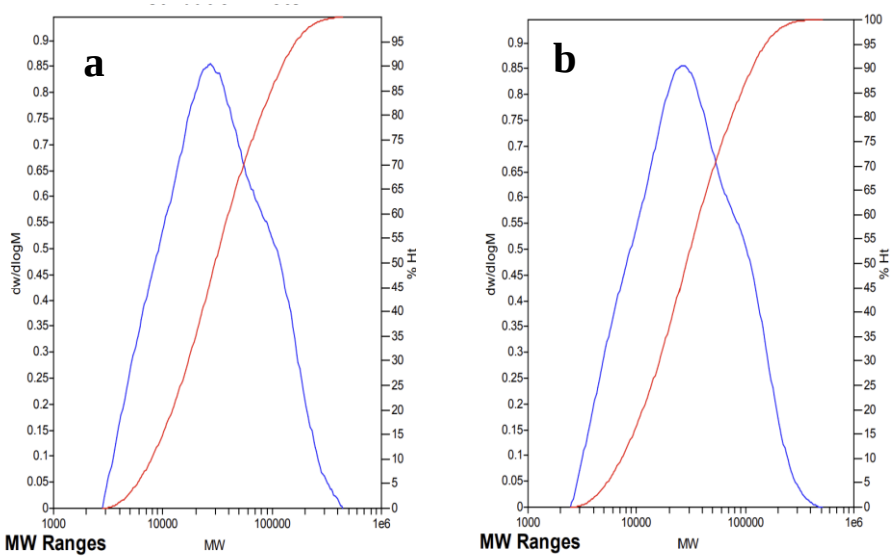

Figure 3-27: HT-GPC molecular weight distribution of polymer: a) PTTBDT; b) PCTBDT.

Table 3-13: HT-GPC molecular weight and PDI data summary for PTTBDT and PCTBDT.

Polymer	M_n (kDa)	M_w (kDa)	PDI
PTTBDT	18.8	50.0	2.66
PCTBDT	17.5	46.7	2.70

Thermal analysis was conducted using TGA and DSC for thermal stability and information on crystalline transitions, respectively. TGA was acquired using a heating rate of 10 °C/min under nitrogen (see **Figure 3-28**). PTTBDT showed 1 % weight loss at 280 °C and a first decomposition step at 399 °C, demonstrating high thermal tolerance. For PCTBDT, 1 % weight loss occurred at 203 °C and a first decomposition step occurred at 256 °C. The thermally removable carbamate side chain is expected to be removed at temperatures around 150-200 °C; however, previously our group has annealed at 250 °C to ensure removal.[75] Due to the relatively

quick heating rate, the side chain is removed continuously as the temperature was increased. At the end of the first step decomposition (381 ^{o}C), 17.8 % of the weight was lost, which corresponds to the percentage of the polymer's weight contained by the carbamate side chain. This confirms that the side chain is thermally removable and indicates why the thermal decomposition occurs earlier than PTTBDT. A second step decomposition was observed at 381 ^{o}C for PCTBDT.

DSC was acquired using a scanning rate of 10 °C/min under nitrogen, where the first cycle went 50 ^{o}C lower than the second cycle and the second cycle went until the polymer lost 0.5 % of its weight in TGA (see **Figure 3-29**). Both polymers have a glass transition around 36 ^{o}C. PTTBDT exhibits a melting temperature at 63 ^{o}C in the first heating scan, but it is not observed in the second. Similarly, PCTBDT has a melting temperature of 64 ^{o}C. These melting temperatures most likely correspond to the side chain, which after cooling is in a different configuration, resulting in no melting peak in the second cycle.[78]

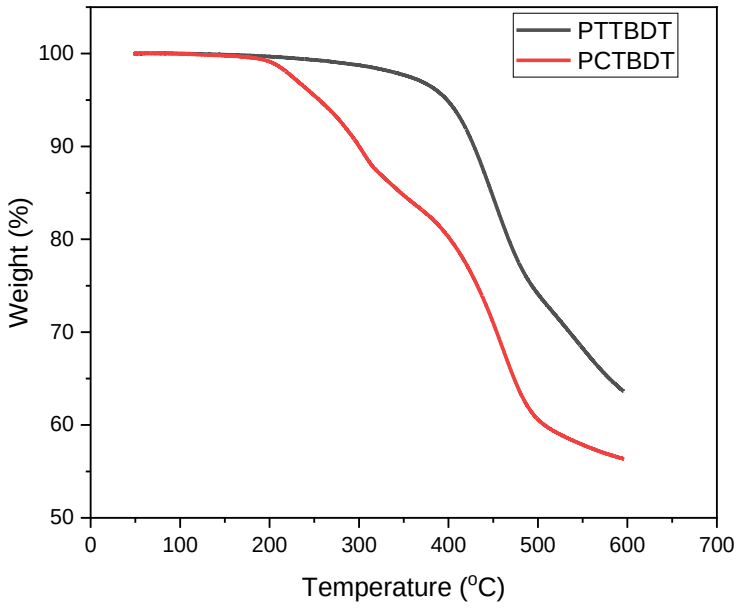

Figure 3-28: TGA curves for polymers PTTBDT, and PCTBDT.

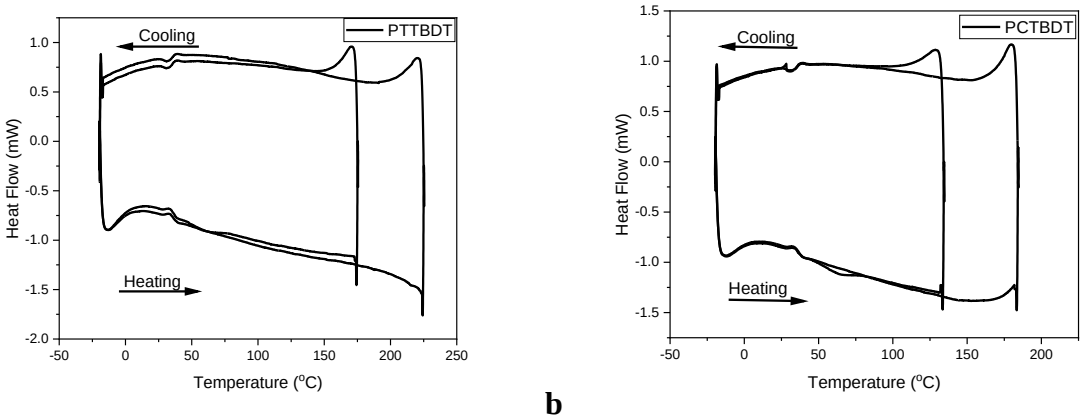

Figure 3-29: DSC curves for polymers: a) PTTBDT; and b) PCTBDT.

3.4 Opto-Electrochemical Properties

UV-vis absorption spectra were taken using the methods described in Section 2.4 (see **Figure 3-30**). Polymers PTTBDT and PCTBDT had large redshifts from solution to thin film. PTTBDT shifted from 478 nm to 521 nm (43 nm) and PCTBDT shifted from 470 nm to 510 nm (40 nm). This indicates a strong shift to better co-planarity and extended conjugation when the polymer is cast as a thin film, compared with noticeable twisting of the backbone and side chain in solution. This is also reflected in the colour changing from orange in solution to light red as a thin film. For both polymers, there is a redshift when the thin film is annealed, indicating a slight improvement on the polymer morphology. PCTBDT showed a larger red shift (13 nm) after annealing, likely caused by rearrangement of the side chain, resulting in better co-planarity and improved conjugation. The optical bandgaps obtained were 2.05, and 2.07 eV for PTTBDT, and PCTBDT, respectively. The overall range of absorption makes these polymers good candidates to pair with NFAs to achieve complementary absorption.

CV was obtained using the same methods described in Section 2.4. The polymers had the following E_{HOMO} levels: PTTBDT (-5.51 eV), and PCTBDT (-5.60 eV). PCTBDT has a 0.09 eV deeper E_{HOMO} than PTTBDT due to the carbamate chain acting as a stronger EWG than the alkyl side chain. **Figure 3-32** shows a comparison between the energy levels obtained from CV and DFT. DFT correctly predicted that PCTBDT would have a lower E_{HOMO} than PTTBDT. The opto-electrochemical information is summarized in **Table 3-14**.

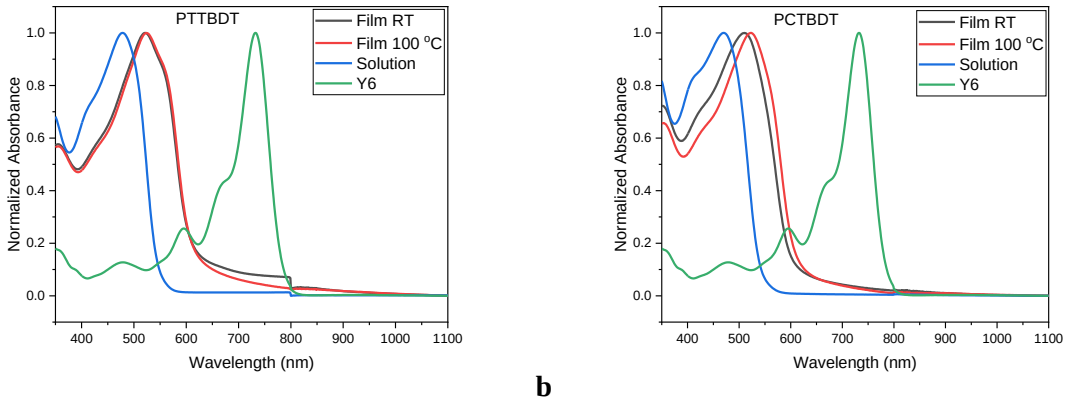

Figure 3-30: UV-vis absorption spectra of as-cast thin film, annealed thin film, and chloroform solution for polymers: a) PTTBDT; and b) PCTBDT.

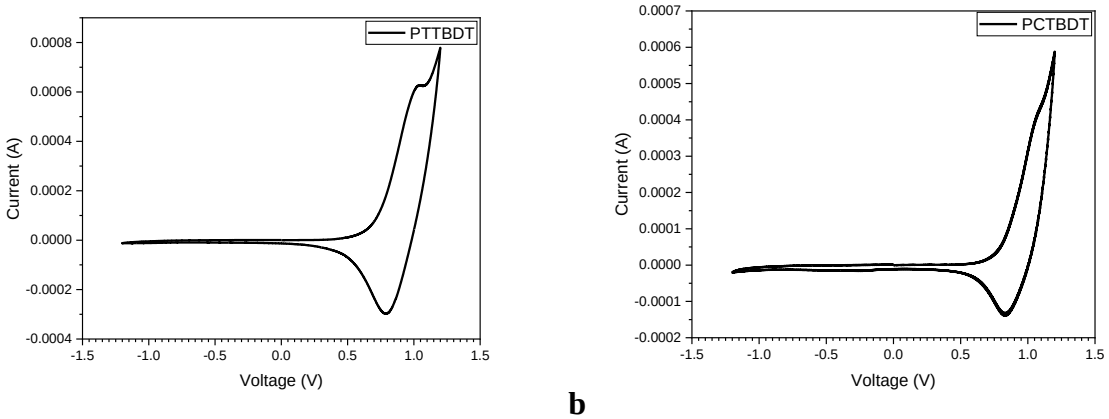

a **b**

Figure 3-31: CV profiles of polymers: a) PTTBDT; and b) PCTBDT.

Table 3-14: Optical and electrochemical properties of polymers PTTBDT, and PCTBDT.

Polymer	$\lambda_{max,s}$ (nm)	$\lambda_{max,fRT}$ (nm)	$\lambda_{max,f100C}$ (nm)	λ_{onset} (nm)	E_g^{opt} (eV)	E_{HOMO} (eV)	E_{LUMO} (eV)
PTTBDT	478	521	524	605	2.05	-5.51	-3.46
PCTBDT	470	510	523	600	2.07	-5.60	-3.53

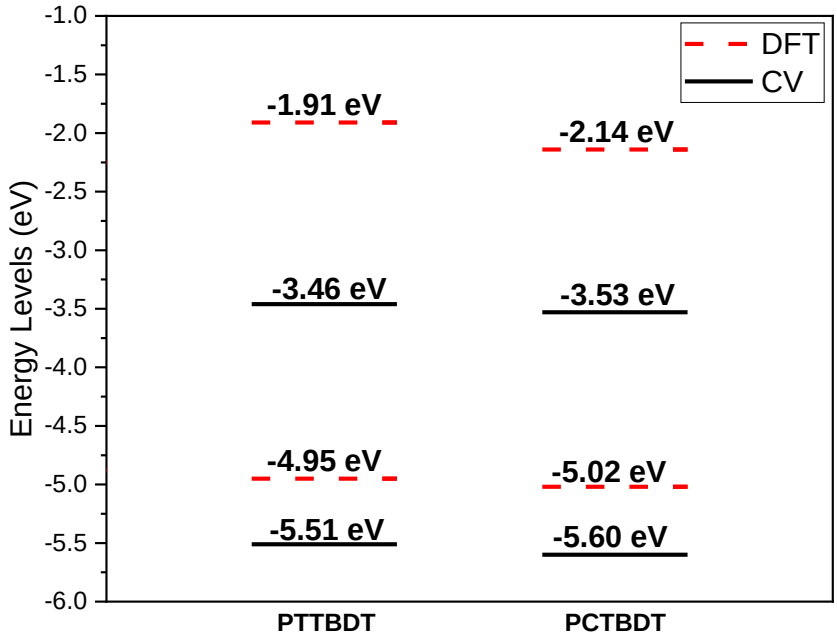

Figure 3-32: Comparison of DFT predicted HOMO and LUMO energy levels with CV obtained HOMO and LUMO levels for polymers PTTBDT, and PCTBDT.

For PL measurements, Y6 was selected as the NFA material to pair with the triazole polymers due to its well-matched energy levels and superior properties compared with IT-4F and ITIC. PL measurements were obtained using the same methods described in Section 2.4 (see **Figure 3-33**). PTTBDT had excellent quenching in the donor region (99.98 %) and good quenching in the acceptor region (91.3 %). PCTBDT showed great quenching in both the donor (97.2 %) and acceptor (98.8 %) regions. The PL results indicated that PTTBDT and PCTBDT have good exciton dissociation with Y6 and have potential for OSC applications.

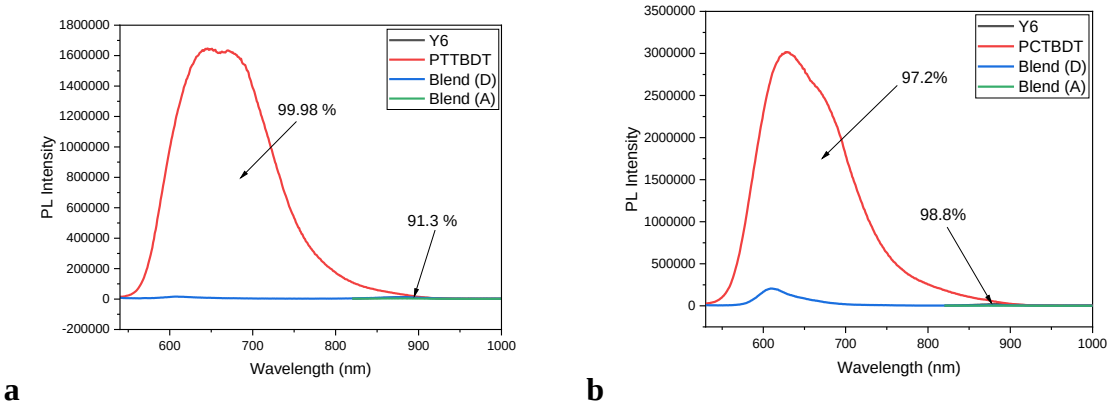

Figure 3-33: PL spectra of a) PTTBDT with Y6; and b) PCTBDT with Y6.

3.5 OPV Performance and Charge Mobility

Details for sample preparation and testing can be found in Section 2.8.2.

Important note: *The triazole polymers were tested with a new device ITO pattern and testing system. In the past devices have achieved a FF of 0.56 by Yuan et al. and as high as 0.71 by Jiang et al. in our lab.*[52,53] *Furthermore, a shunt resistance of 883 ohm•cm^2 and a series resistance of 2.84 ohm•cm^2 have been reported by our group.*[53] *However, after switching to the new system, the FF is lower than previously achieved (~0.51 is best achieved currently), which is related to issues with low shunt resistance and high series resistance. This indicates that there is a problem with one or more of the layers and/or interfaces between layers, which is still being investigated by our group. Therefore, the data presented below might not represent the best data possible for these polymers.*

Summaries of the performance of each polymer can be found in **Table 3-15** to **Table 3-18** and a comparison of the best J-V curves for each polymer is shown in **Figure 3-34**. PTTBDT achieved a highest PCE of 5.00 % (J_{sc} = 17.01 mA/cm^2, V_{oc} = 0.83 V, and FF = 0.35) without annealing. Annealing did not improve the results, and slightly thinner cells (~80 nm) showed better performance than ~90 to ~100 nm devices. PTTBDT achieved a moderate J_{sc} and relatively high V_{oc}, comparable with a high performing polymer PD2, which also has an E_{HOMO} of -5.5 eV.[1] However, the FF is quite low for this device. Considering devices in Chapters 4 and 5 of this thesis (tested under the same conditions) achieved an FF ranging from 0.39 to 0.51, there is some room for improvement once the device fabrication and testing are optimized but it is limited due to higher FF achieved for other materials. For example, if an FF of 0.56 was achieved, the PCE would improve to 8.00 % if all other factors remained the same. A more reasonable improvement to 0.4 would result in a slight PCE improvement to 5.75 %. The low FF is affected by the high series resistance and low shunt resistance. Potentially there are issues with surface roughness of the active layer or one of the other layers of the OSC device, which is negatively affecting the performance. As seen in the DFT calculations, the dihedral angle of this polymer was quite high. From UV-vis there is a substantial redshift when going from solution to thin film; however, it is difficult to know how much the dihedral angle changes. Therefore, this polymer potentially still suffers from backbone and side chain twisting, restricting its ability to achieve good charge transport and morphology, which can negatively impact the FF.

PCTBDT performed worse than PTTBDT, with a best PCE of 3.29 % (J_{sc} = 13.58 mA/cm^2, V_{oc} = 0.76 V, and FF = 0.32). A reduction in J_{sc}, V_{oc}, and FF was observed compared to PTTBDT. Similar to POBETBDT, the carbamate EWG side chain has a triazole ring between the backbone, which could negatively affect the exciton lifetimes and result in recombination. Furthermore, annealing was not helpful for this polymer and resulted in a reduction in PCE, where 150 ^{o}C was slightly better than 50 and 100 ^{o}C. Due to the thermally removable side chain, an unsubstituted nitrogen in the triazole ring results in instability and could potentially be a problem for hole trapping. Additionally, like PTTBDT, PCTBDT was predicted to have a relatively high dihedral angle by DFT calculations, which could be negatively affecting the charge transfer and morphology of the polymer. Although the triazole polymers showed better performance than the ethynyl polymers, barring a significant improvement to the FF of PTTBDT, the performance is still quite low for OSC applications, making the triazole ring a questionable choice for side chain functionalization in OSCs.

EQE was also measured, which provides a ratio of the electrons in the circuit compared to photons in the incident light. This also provides a visual representation of the photocurrent generation efficiency under a range of different wavelengths. PCTBDT achieved a highest EQE of 48 % at 810 nm, whereas PTTBDT achieved a best EQE of 56 %. **Table 3-19** compares the J_{sc} obtained from OPV and EQE. The values for PCTBDT have high agreeance of 0.16 %. However, PTTBDT showed 14.55 % error. This indicates that as the J_{sc} values increase, the error becomes greater. Therefore, OPV overestimates J_{sc} and/or EQE underestimates. This error could be caused by the unoptimized new devices and measurement system. Optimization of this system could reduce the error to an acceptable amount (<10 %), considering under the previous system the percent error was consistently less than 10 %.

Table 3-15: Summary of OSC device parameters for PTTBDT:Y6.

Device	Annealing Temperature (°C)	RPM	Thickness (nm)
1	No annealing	1000	102.95 (±0.45)
2	No annealing	1500	92.35 (±2.25)
3	No annealing	2000	78.95 (±0.65)
4	50	1000	99.05 (±0.65)
5	50	1500	89.20 (±0.20)
6	50	2000	78.20 (±1.50)
7	100	1000	104.00 (±0.50)
8	100	1500	89.90 (±0.30)
9	100	2000	80.75 (±0.45)
10	150	1000	100.00 (±0.30)
11	150	1500	90.55 (±0.85)
12	150	2000	80.35 (±0.55)

Table 3-16: Summary of OSC performance for PTTBDT:Y6.

Device	Jsc (mA/cm^2)	Voc (V)	FF	PCE (%)	Avg. Rsh ($ohm•cm^2$)	Avg. Rs ($ohm•cm^2$)
1	14.32 (13.69±0.48)	0.81 (0.80±0.01)	0.30 (0.30±0.01)	3.54 (3.30±0.19)	112 (±14)	34.67 (±1.58)
2	15.84 (15.50±0.54)	0.82 (0.80±0.01)	0.32 (0.32±0)	4.19 (3.91±0.24)	113 (±4)	26.52 (±0.96)
3	17.01 (16.23±0.68)	0.83 (0.80±0.02)	0.35 (0.34±0.01)	5.00 (4.42±0.40)	133 (±8)	22.05 (±1.35)
4	15.46 (14.28±0.94)	0.80 (0.79±0.01)	0.31 (0.31±0)	3.81 (3.45±0.31)	107 (±1)	30.24 (±3.60)
5	15.37 (14.56±0.88)	0.82 (0.79±0.02)	0.32 (0.31±0.02)	4.03 (3.56±0.36)	112 (±10)	30.38 (±6.89)
6	16.03 (15.84±0.29)	0.81 (0.79±0.01)	0.34 (0.33±0.01)	4.41 (4.13±0.21)	131 (±8)	23.22 (±1.26)
7	12.33 (11.33±0.71)	0.81 (0.80±0.01)	0.30 (0.29±0.01)	3.00 (2.63±0.22)	110 (±1)	45.80 (±5.19)
8	16.55 (15.93±0.70)	0.81 (0.79±0.01)	0.33 (0.33±0.01)	4.49 (3.94±0.40)	118 (±4)	23.38 (±1.22)
9	17.14 (16.17±0.64)	0.79 (0.79±0.01)	0.34 (0.33±0)	4.53 (4.20±0.27)	125 (±5)	22.57 (±0.81)
10	15.54 (14.80±0.87)	0.78 (0.77±0.01)	0.31 (0.31±0)	3.73 (3.54±0.20)	102 (±5)	26.50 (±2.63)
11	16.93 (16.16±0.45)	0.76 (0.76±0.01)	0.32 (0.32±0)	4.12 (3.93±0.14)	103 (±6)	22.59 (±1.44)
12	18.04 (17.49±0.51)	0.77 (0.74±0.03)	0.35 (0.34±0.01)	4.83 (4.36±0.27)	104 (±20)	14.69 (±3.65)

Table 3-17: Summary of OSC device parameters for PCTBDT:Y6.

Device	Annealing Temperature (°C)	RPM	Thickness (nm)
1	No annealing	1500	85.00 (±2.00)
2	No annealing	2000	73.95 (±0.55)
3	No annealing	2500	66.35 (±1.35)
4	50	1500	81.80 (±0.10)
5	50	2000	63.00 (±1.10)
6	50	2500	59.25 (±0.55)
7	100	1500	79.55 (±0.85)
8	100	2000	67.80 (±0.60)
9	100	2500	62.20 (±2.20)
10	150	1500	85.25 (±0.65)
11	150	2000	69.15 (±0.85)
12	150	2500	65.25 (±1.05)

Table 3-18: Summary of OSC performance for PCTBDT:Y6.

Device	Jsc (mA/cm^2)	Voc (V)	FF	PCE (%)	Avg. Rsh ($ohm•cm^2$)	Avg. Rs ($ohm•cm^2$)
1	11.40 (10.46±0.64)	0.75 (0.71±0.02)	0.29 (0.28±0)	2.50 (2.10±0.22)	105 (±5)	19.27 (±5.01)
2	11.83 (10.54±0.79)	0.70 (0.71±0.03)	0.29 (0.29±0)	2.43 (2.15±0.15)	109 (±5)	24.65 (±12.28)
3	13.58 (12.74±1.22)	0.76 (0.73±0.02)	0.32 (0.31±0.01)	3.29 (2.91±0.46)	138 (±17)	17.85 (±0.47)
4	10.18 (9.54±0.90)	0.75 (0.72±0.01)	0.28 (0.28±0)	2.10 (1.88±0.23)	117 (±8)	36.40 (±4.41)
5	11.99 (10.75±0.92)	0.76 (0.73±0.02)	0.29 (0.29±0)	2.66 (2.25±0.28)	128 (±5)	29.22 (±1.90)
6	11.39 (10.69±1.01)	0.73 (0.70±0.04)	0.29 (0.29±0.01)	2.43 (2.17±0.22)	122 (±14)	24.46 (±10.66)
7	11.07 (9.55±1.02)	0.75 (0.72±0.02)	0.29 (0.28±0.01)	2.44 (1.93±0.31)	129 (±8)	35.26 (±4.93)
8	12.45 (12.08±1.13)	0.74 (0.82±0.02)	0.29 (0.33±0)	2.64 (2.39±0.30)	134 (±5)	32.29 (±2.80)
9	11.64 (10.77±0.62)	0.73 (0.71±0.02)	0.29 (0.29±0)	2.41 (2.15±0.19)	86 (±53)	45.22 (±7.32)
10	11.41 (9.68±1.09)	0.76 (0.73±0.02)	0.29 (0.28±0.01)	2.49 (1.95±0.30)	127 (±5)	38.85 (±4.24)
11	11.67 (9.87±1.15)	0.73 (0.71±0.01)	0.29 (0.28±0.01)	2.45 (1.95±0.29)	116 (±10)	35.33 (±5.02)
12	12.59 (11.28±1.16)	0.75 (0.72±0.01)	0.30 (0.29±0.01)	2.78 (2.39±0.31)	127 (±10)	27.94 (±3.18)

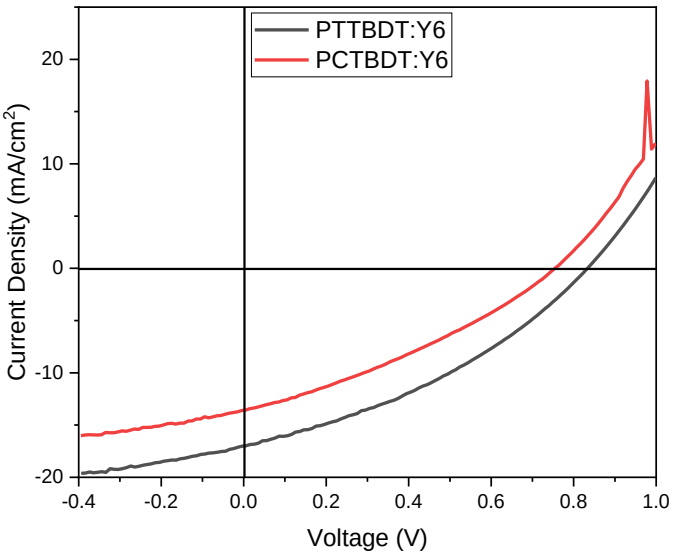

Figure 3-34: J-V curve of best performing OPV devices: PTTBDT:Y6 (RT), PCTBDT:Y6 (RT).

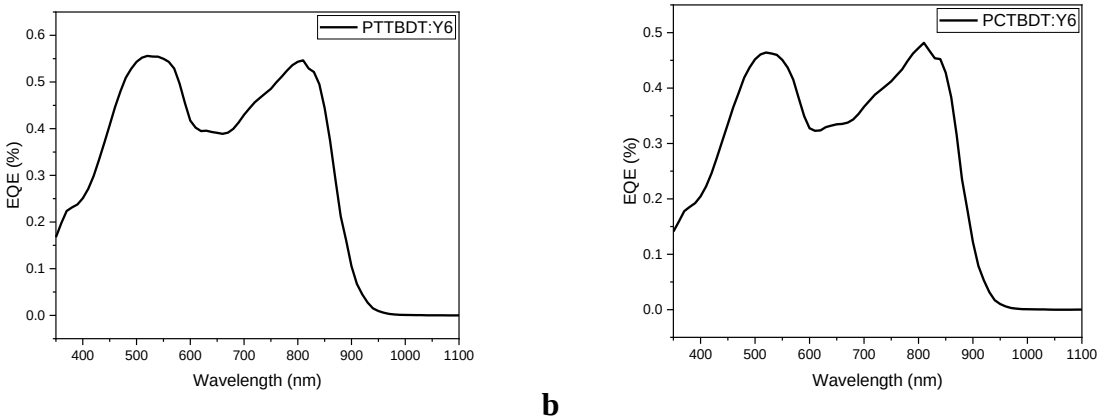

a **b**

Figure 3-35: EQE of best performing OSCs based on a) PTTBDT:Y6; and b) PCTBDT:Y6.

Table 3-19: Comparison of Jsc obtained from OPV and EQE measurements for PTTBDT:Y6, and PCTBDT:Y6.

Polymer	Jsc from OPV (mA/cm^2)	Jsc from EQE (mA/cm^2)	Error (%)
PTTBDT	16.93	14.78	14.55
PCTBDT	12.59	12.61	0.16

SCLC mobility was obtained following the methods described in Section 2.5. **Table 3-20** summarizes the calculated hole and electron mobilities, with both the best and average values. For good devices, the SCLC mobility should be greater than 10^{-4} $cm^2V^{-1}s^{-1}$ and the ratio between electron and hole mobilities should be 1.[1] The neat triazole polymers, PTTBDT and PCTBDT had low hole mobilities with values of $6.27x10^{-5}$ $cm^2V^{-1}s^{-1}$ and $4.70x10^{-6}$ $cm^2V^{-1}s^{-1}$, respectively. For PTTBDT a significant decrease in hole mobility to $2.43x10^{-6}$ $cm^2V^{-1}s^{-1}$ was observed when blended with Y6. However, the electron mobility is $3.40x10^{-6}$ $cm^2V^{-1}s^{-1}$, providing a relatively balanced ratio of 1.40. Unfortunately, although the mobility is relatively balanced, it is quite low compared to the best performing materials. Backbone twisting could be negatively impacting the charge mobility, and therefore, the performance of the material. PCTBDT also has a substantial decrease in hole mobility when mixed with Y6, with a value of $5.23x10^{-7}$ $cm^2V^{-1}s^{-1}$ obtained. The electron mobility is two magnitudes larger (10^{-5} $cm^2V^{-1}s^{-1}$), resulting in extremely unbalanced charge mobility (25.62). This polymer has several flaws, which could explain the low mobility: 1) the backbone is predicted to be moderately twisted by DFT; 2) partial removal of the side chain could impact the morphology of the polymer; 3) the thermally removable side chain might result in hole traps at the negatively charged unsubstituted nitrogen. The unbalanced mobility can contribute to the lower J_{sc} compared with PTTBDT and the low FF.

Table 3-20: SCLC hole and electron mobilities for neat polymers and D:A blend films of PTTBDT, and PCTBDT with Y6.

Polymer	μ_e ($x10^{-4}$ $cm^2V^{-1}s^{-1}$)	μ_h ($x10^{-4}$ $cm^2V^{-1}s^{-1}$)	μ_e/μ_h
PTTBDT	N/A	0.627 (0.555)	N/A
PTTBDT:Y6	0.0340 (0.0204)	0.0243 (0.0166)	1.40 (1.23)
PCTBDT	N/A	0.0470 (0.0221)	N/A
PCTBDT:Y6	0.134 (0.124)	0.00523 (0.00433)	25.62 (28.64)

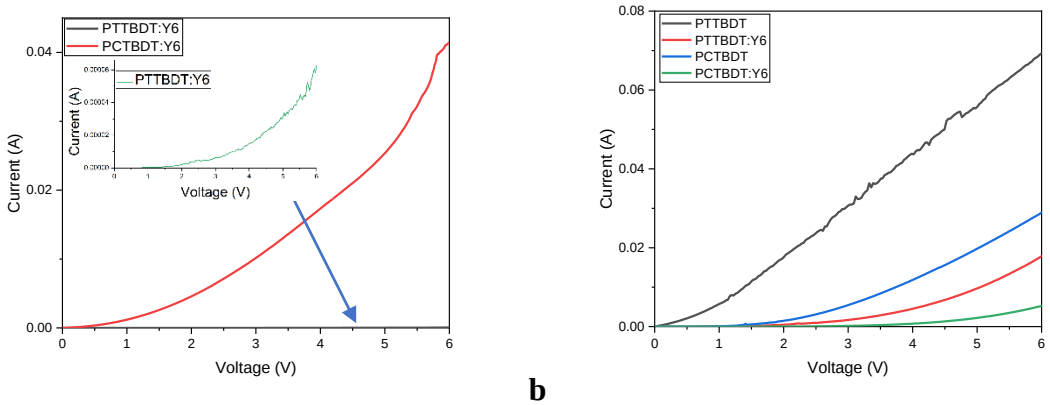

a **b**

Figure 3-36: a) electron mobility I-V curves for PTTBDT:Y6, and PCTBDT:Y6; b) hole mobility I-V curves of neat PTTBDT, PTTBDT:Y6, neat PCTBDT, and PCTBDT:Y6.

3.6 Crystallinity

Figure 3-37 shows the 1D and 2D XRD for PTTBDT as a neat polymer and when blended with Y6. PTTBDT displays no obvious peaks both in-plane and out-of-plane, indicating it forms an amorphous film. The probable cause of this is twisting in the backbone and/or triazole ring side chain, resulting in an inability to form strong π-π stacking interactions.

Similarly, **Figure 3-38** shows the 1D and 2D XRD for PTTBDT as a neat polymer and when blended with Y6. As a neat film, PTTBDT shows weak π-π stacking in both the in-plane and out-of-plane measurements when annealed at 150 ^{o}C. This corresponds to a d-spacing of 0.376 nm. This peak is likely caused by the carbamate removal process beginning. However, no other temperatures display any significant peaks for the neat polymer. The blend film shows no peaks in the in-plane or out-of-plane measurements, indicating the active layer adopts an amorphous morphology.

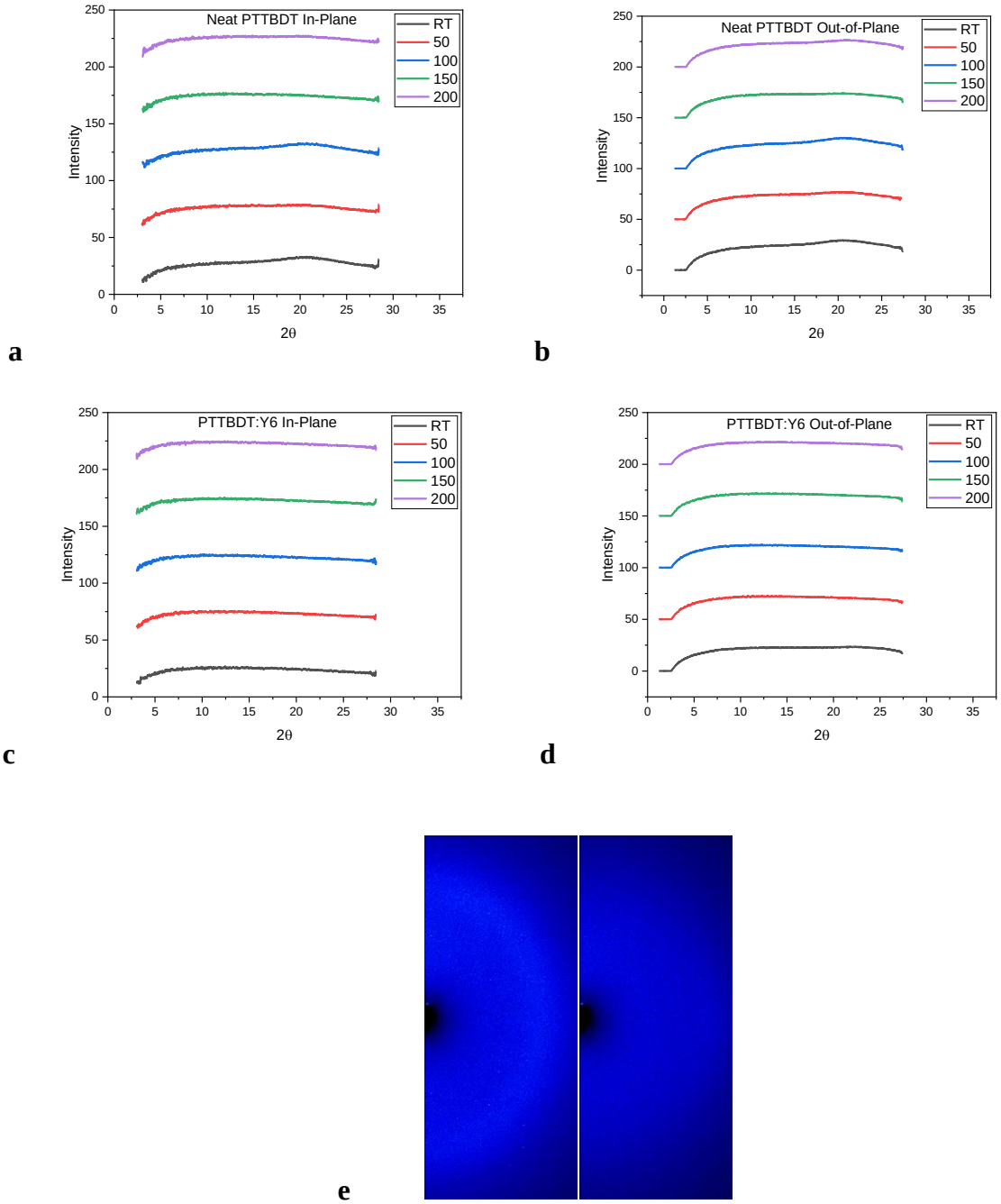

Figure 3-37: GIXD patterns of films at different annealing temperatures: a) in-plane neat PTTBDT; b) out-of-plane neat PTTBDT; c) in-plane PTTBDT:Y6 blend; d) out-of-plane PTTBDT:Y6 blend; e) 2D images of the best performing material (no annealing), where the left is neat PTTBDT and the right is PTTBDT:Y6.

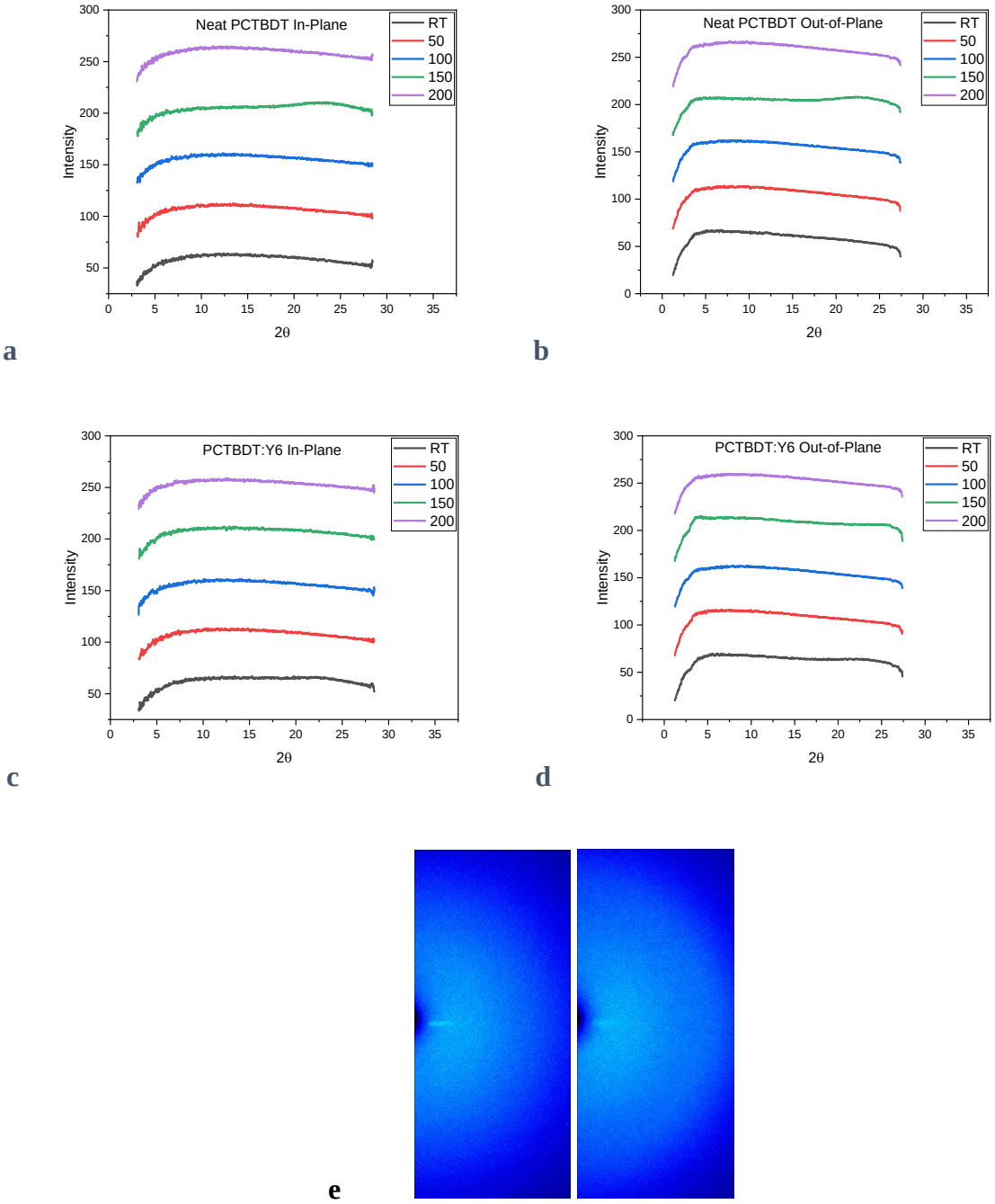

Figure 3-38: GIXD patterns of films at different annealing temperatures: a) in-plane neat PCTBDT; b) out-of-plane neat PCTBDT; c) in-plane PCTBDT:Y6 blend; d) out-of-plane PCTBDT:Y6 blend; e) 2D images of the best performing material (no annealing), where the left is neat PCTBDT and the right is PCTBDT:Y6.

3.7 Summary and Future Direction

In summary, two novel donor polymers were synthesized based on a thiophene-BDT backbone. PTTBDT, and PCTBDT, were synthesized by adding a triazole ring side chain to thiophene, which had an alkyl and carbamate chain attached at the middle nitrogen atom in the triazole ring, respectively. The triazole rings were used to extend the conjugation perpendicular to the backbone and polarize the polymer for good electron-withdrawing capabilities of the A unit in the D-A donor polymer. DFT calculations predicted the side chains would effectively lower the E_{HOMO} for good energy level matching with Y6. However, PTTBDT and PCTBDT had dihedral angles greater than thirty degrees, indicating substantial twisting that could negatively affect the performance. PTTBDT appeared to be highly thermally stable, while both polymers had wide bandgaps and low lying E_{HOMO} levels. The polymers displayed good PL quenching with Y6, indicating light could be effectively captured. PTTBDT had a best PCE of 5.00 % (J_{sc} = 17.01 mA/cm^2, V_{oc} = 0.83 V, and FF = 0.35) without annealing, while PCTBDT had a best PCE of 3.29 % (J_{sc} = 13.58 mA/cm^2, V_{oc} = 0.76 V, and FF = 0.32). PTTBDT had low, relatively balanced mobility and an amorphous structure. It is suspected that this polymer is too twisted to achieve satisfactory performance. Finally, PCTBDT had extremely low hole mobility, resulting in an unbalanced mobility ratio. PCTBDT has potential issues including backbone twisting, and a thermally removable side chain, which when removed potentially results in hole trapping, limiting the performance of this material. For OSC D-A polymer donor materials, the use of triazole ring side chains on a thiophene unit was not an effective choice when co-polymerizing with BDT.

In terms of future direction, the surface roughness and domain sizes of the active layers can be examined using AFM to identify any potential morphology issues. For OSC applications, it is necessary to optimize the active layer to improve the FF. Furthermore, a different ratio between the donor polymer and NFA could be used to improve the mobility ratio, which could be especially effective in pushing the performance limits of PTTBDT since it was the best performing material and had slightly unbalanced mobility. For PTTBDT, the donor polymer can also be tuned by introducing halogen atoms (F, Cl) onto the BDT unit, which would lower the E_{HOMO}, potentially leading to improved V_{oc} and PCE, and has been shown to improve crystallinity.[79] For PCTBDT, organic field-effect transistor mobility could be compared with

PTTBDT to assess potential hole-trapping issues, especially upon thermal removal of the carbamate side chain. Finally, to minimize the need for high vacuum deposition and to eliminate potential problems associated with MoO_3, a different hole transfer layer, such as Brilliant Matters BM-HTL-1, could be used, which can be printed, or spin coated onto the substrate.

3.8 Experimental Section

3.8.1 Materials Characterization

The chemicals and solvents used for synthesis were purchased from commercial vendors including Fluka, Armstrong, Sigma-Aldrich, TCI, and VWR without further purification. All anhydrous solvents were purchased from Sigma-Aldrich. Y6 and 1,1'-[4,8-bis[5-(2-ethylhexyl)-2-thienyl]benzo[1,2-b:4,5-b']dithiophene-2,6-diyl]bis[1,1,1-trimethylstannane] (BDT) were purchased from 1-Material. Specific synthesis details will be shown in Section 3.8.3 below. The characterization and testing of polymers were done using the same equipment as specified in Section 2.8.1.

3.8.2 OSC Device Fabrication and Characterization

The OSC fabrication and characterization was completed according to the information provided in Section 2.8.2.

3.8.3 Synthesis Routes

Synthesis of 5-(thiophen-3-yl)-1H-1,2,3-triazole

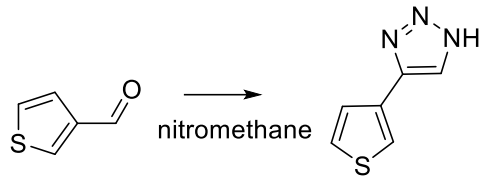

1.1 R:NaN3, R:NH4OAc, R:AcOH, S:DMF, 100°C; 100°C → rt

1.2 R:H2O, rt

A stir bar was placed in a 500 mL two-neck round bottom flask and the system was evacuated to purge with nitrogen. The reagents were added into the flask with sodium azide added last (3-thiophenecarboxaldehyde: 1 equiv.; nitromethane: 3 equiv.; sodium azide: 2.5 equiv.; ammonium acetate: 1 equiv.; acetic acid: 0.5 equiv.) . The reaction was stirred at 100 ^{o}C for 1 hour. TLC was checked; if complete, the reaction was cooled to room temperature, quenched with water, and extracted with diethyl ether. The organic phase was dried with sodium sulfate and the solvent was evaporated under vacuum. The product was purified with a column under air, with an initial eluent of hexane:ethyl acetate (5:1), which was increased to 3:1 once the initial compounds were exiting. A white solid is obtained. (Yield: 1.519 g, 56 %). ^{1}H NMR (300 MHz, $CDCl_3$, δ/ppm): 7.85 (s, 1H), 7.68 (d, 1 H), 7.48 (d, 1H), 7.40 (m, 1H).[76]

Synthesis of 2-methyl-4-(thiophen-3-yl)-2H-1,2,3-triazole

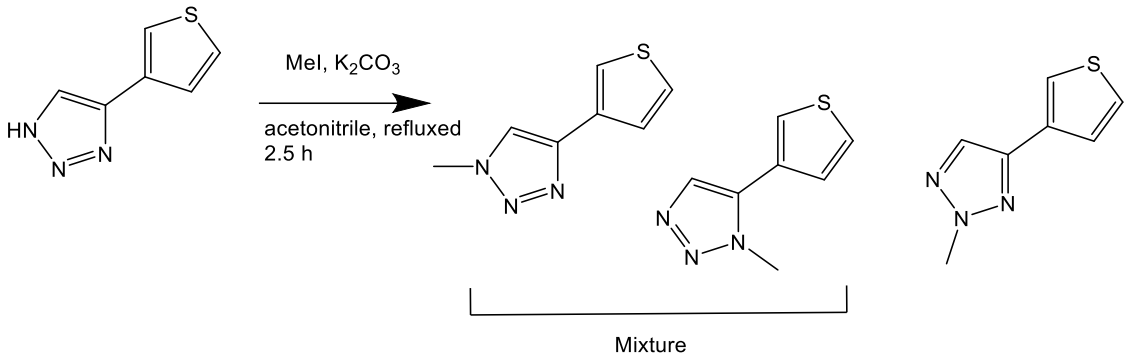

To a solution of triazole thiophene (1 equiv.), potassium carbonate (2 equiv.) and acetonitrile were added. Iodomethane (1.5 equiv.) was added dropwise. The reaction was heated to 80 ^{o}C and stirred for 2.5 hours. The flask was then cooled, and the contents were filtered. The solvent was evaporated using the rotary evaporator and purified via a column using hexane:ethyl acetate 4:1. Three isomers are expected during this reaction; however, the two undesirable isomers are obtained in a mixture at a lower yield than the middle substitution. (Yield: 205.5 mg, 38 % desired product, 158.1 mg, 29 % mixture of other isomers). ^{1}H NMR (300 MHz, $CDCl_3$, δ/ppm): 7.70 (s, 1H), 7.59 (m, 1H), 7.43 (m, 1H), 7.37 (m, 1H), 4.2 (s, 3H).[77]

Synthesis of 4-(2,5-dibromothiophen-3-yl)-2-methyl-2H-1,2,3-triazole

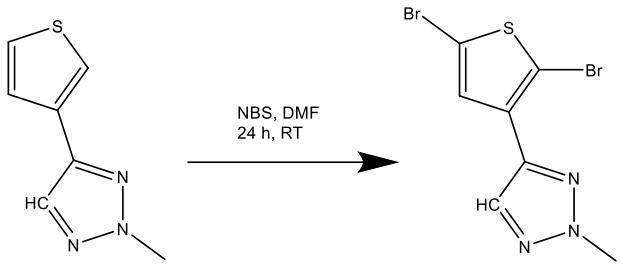

In a 25 mL 2-neck round-bottom flask, methyl triazole thiophene (1 equiv.) and half of the DMF were added. The reaction vessel was wrapped in aluminum foil to avoid light. Next, a mixture of NBS (2.5 equiv.) in the remaining DMF was made and added dropwise to the solution. The solution was stirred for 24 hours in the dark. The mixture was then poured into water and extracted with ether. The organic phase was dried with sodium sulfate and the solvent was removed via rotary evaporator. The crude product was purified via column with the eluent as hexane:ethyl acetate 6:1, yielding a white solid. (Yield: 115.2 mg, 30 %). ^{1}H NMR (300 MHz, $CDCl_3$, δ/ppm): 8.1 (s, 1H), 7.35 (s, 1H), 4.21 (s, 3H).

Synthesis of 2-ethylhexyl 4-(thiophen-3-yl)-2H-1,2,3-triazole-2-carboxylate

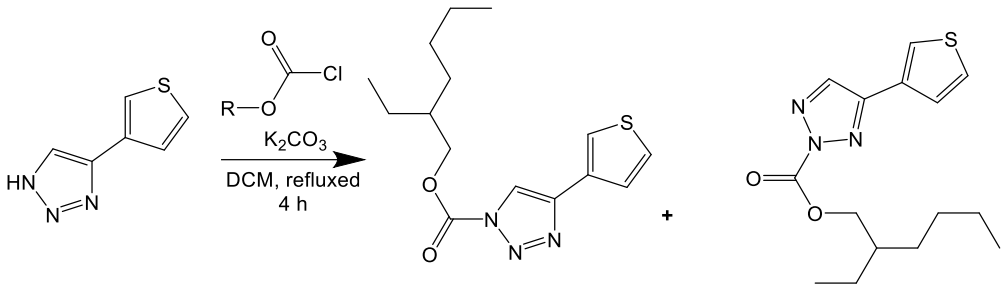

To a solution of triazole thiophene (1 equiv.), potassium carbonate (2 equiv.) and DCM were added. The system was placed in an ice bath. Ethylhexyl chloroformate (1.5 equiv.) was added dropwise. The reaction was heated to 45 ^{o}C and stirred for 4 hours. The flask was then cooled to room temperature, and water was added. DCM was used to extract the product. The solvent was evaporated using the rotary evaporator and purified via a column using hexane:ethyl acetate 4:1. (Yield: 212.1 mg, 41.8 % middle substitution, 134.1 mg, 26.5 % undesired outer nitrogen substitution). ^{1}H NMR (300 MHz, $CDCl_3$, δ/ppm): 8.02 (s, 1H), 7.82 (m, 1H), 7.59 (m, 1H0, 7.43 (m, 1H), 4.47 (d, 2H), 1.85 (m, 1H), 1.33 (m, 8H), 0.89 (m, 6H).[77]

Synthesis of 2-ethylhexyl 4-(2,5-dibromothiophen-3-yl)-2H-1,2,3-triazole-2-carboxylate

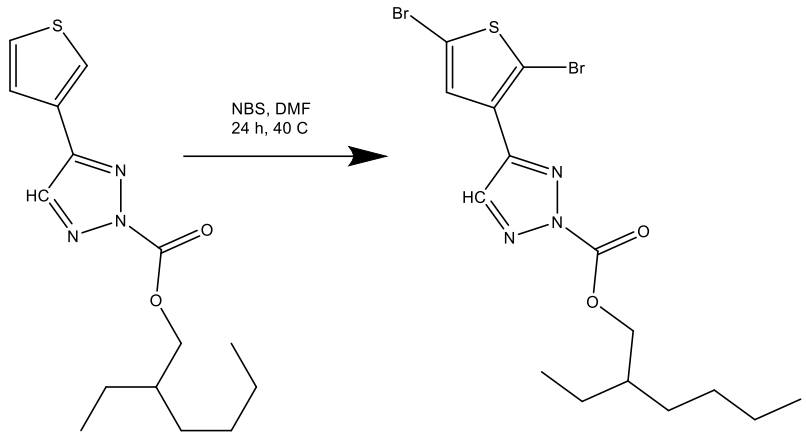

In a 25 mL 2-neck round-bottom flask, carbamate triazole thiophene (1 equiv.) and half of DMF were added. The reaction vessel was wrapped in aluminum foil to avoid light. Next, a mixture of NBS (2.5 equiv.) in the remaining DMF was made and added dropwise to the solution. The solution was stirred for 24 hours in the dark at 40 ^{o}C. The mixture was then cooled, poured into water, and extracted with ether. The organic phase was dried with sodium sulfate and the solvent was removed via rotary evaporator. The crude product was purified via column with the eluent DCM:hexane 3:1, yielding a white solid. (Yield: 148.6 mg, 49 %). ^{1}H NMR (300 MHz, $CDCl_3$, δ/ppm): 8.45 (s, 1H), 7.51 (s, 1H), 4.47 (d, 2H), 1.86 (m, 1H), 1.31 (m, 8H), 0.89 (m, 6H).

Synthesis of polymer PTTBDT

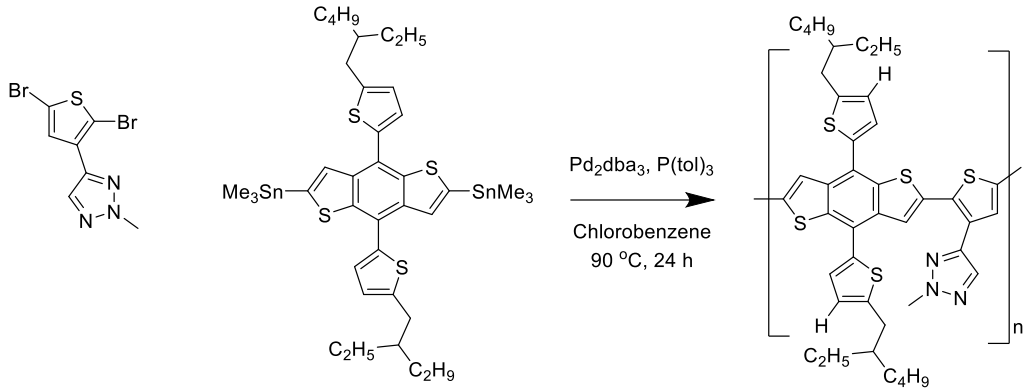

The monomer (1 equiv.), tri(o-tolyl)phosphine ($(P(tol)_3$) (0.08 equiv.) and 1,1'-[4,8-bis[5-(2-ethylhexyl)-2-thienyl]benzo[1,2-b:4,5-b']dithiophene-2,6-diyl]bis[1,1,1-trimethylstannane] (BDT) (1 equiv.) were added to a 2-neck 25 mL round-bottom flask with a small stir bar. The system was purged with argon by performing 3 vacuum cycles. Anhydrous chlorobenzene was added (4 mL). Tris(dibenzylideneacetone)dipalladium(0) catalyst (Pd_2dba_3) (0.04 equiv.) was measured in an inert atmosphere such as a nitrogen filled glove bag. A 1 mL solution of the catalyst dissolved in chlorobenzene was prepared and added to the flask. The reaction was set at 90 °C for 24 hours. After, the reaction was cooled to room temperature and then stirred in 150 mL of methanol for 30 minutes to an hour. The solid was collected via vacuum filtration and then washed with solvents in the following order: acetone, hexane, chloroform, and chlorobenzene in a Soxhlet extractor. (Yield: 115.7 mg, 96.4 % in chloroform).

Synthesis of polymer PCTBDT

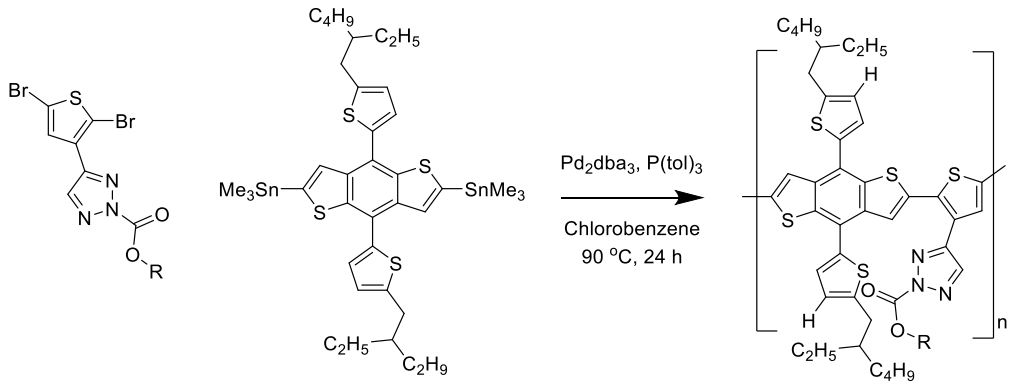

The monomer (1 equiv.), tri(o-tolyl)phosphine ((P(tol)$_3$) (0.08 equiv.) and 1,1'-[4,8-bis[5-(2-ethylhexyl)-2-thienyl]benzo[1,2-b:4,5-b']dithiophene-2,6-diyl]bis[1,1,1-trimethylstannane] (BDT) (1 equiv.) were added to a 2-neck 25 mL round-bottom flask with a small stir bar. The system was purged with argon by performing 3 vacuum cycles. Anhydrous chlorobenzene was added (4 mL). Tris(dibenzylideneacetone)dipalladium(0) catalyst (Pd_2dba_3) (0.04 equiv.) was measured in an inert atmosphere such as a nitrogen filled glove bag. A 1 mL solution of the catalyst dissolved in chlorobenzene was prepared and added to the flask. The reaction was set at 90 ^oC for 24 hours. After, the reaction was cooled to room temperature and then stirred in 150 mL of methanol for 30 minutes to an hour. The solid was collected via vacuum filtration and then washed with solvents in the following order: acetone, hexane, and chloroform in a Soxhlet extractor. (Yield: 88.8 mg, 74 % in chloroform).

Chapter 4: Synthesis, Characterization, and Performance of a Wide Bandgap Tetrafluorobenzene-BDT D-A Polymer

4.1 Introduction

The discovery of Y6, by Zou et al. has led to major breakthroughs in PCE for OSCs, with the leading materials approaching 19 %.[21] A lot of resources have been applied to research on wide bandgap D-A polymer donors, which can achieve complementary absorption, balanced charge mobility, and good morphology when paired with Y6. For commercialization, it is important to target inexpensive materials with low synthetic complexity and good solubility for easy processability. This chapter discusses the synthesis, characterization, and testing of a novel polymer, which is synthesized with the goal of an inexpensive, wide bandgap D-A polymer. This polymer should have a low lying E_{HOMO} that matches well with Y6, while maintaining good co-planarity to potentially achieve face-on orientation for good charge transfer.

In 2019, Zhang et al. synthesized a polymer with the repeat unit BDT-benzene to function as a hole transport layer in perovskite solar cells.[55] This polymer had an E_{HOMO} of -5.16 eV, and an E_{LUMO} of -2.89 eV, rendering a bandgap of 2.27 eV.[55] Furthermore, a dihedral angle of 22.4 degrees was predicted by DFT.[55] In comparison with other BDT-thiophene based materials tested by Zhang et al., the SCLC hole mobility was an order of magnitude less for the BDT-benzene polymer, with a value of $3x10^{-5}$ $cm^2/V^{-1}s^{-1}$.[55] However, the reason for worse hole mobility was due to the more twisted structure when BDT was paired with benzene as opposed to thiophene.[55] Despite the different application, the structure was interesting for applications in the active layer of OSCs. However, some of its limitations need to be overcome to ensure the opto-electrochemical properties favour good OPV performance. The HOMO energy level of the benzene-BDT polymer is similar to P3HT; thus, it is too high for applications with NFAs like Y6. One potential reason is that the BDT-benzene structure is a D-D polymer. Therefore, substitution of the benzene ring with EWGs could help lower the E_{HOMO} and make an effective D-A polymer for OSC applications. This chapter will investigate one polymer where the benzene ring is fluorinated to assess the potential of this new structure.

4.2 Polymer Structure Design

To address the addition of EWG substituents onto the benzene ring, a 1,4-dibromotetrafluorobenzene ring was commercially available. This is a promising candidate for OSC applications for two reasons: 1) fluorine atoms are a good EWG, which will help polarize the benzene unit and lower the E_{HOMO} level;[1] 2) the fluorine atoms could promote better co-planarity through a conformation lock due to hydrogen bonding. Since the reason for poor mobility of the unsubstituted benzene-BDT polymer synthesized by Zhang et al. was twisting, a more co-planar molecule with EWGs could help with increasing the hole mobility, resulting in a good D-A donor polymer for OSCs. Therefore, this structure was investigated with DFT calculations, before proceeding to synthesize and characterize this material for OPV applications. This chapter will investigate the polymer, PFBBDT, seen in **Figure 4-39** to assess its applicability as a wide bandgap D-A polymer for OSC devices.

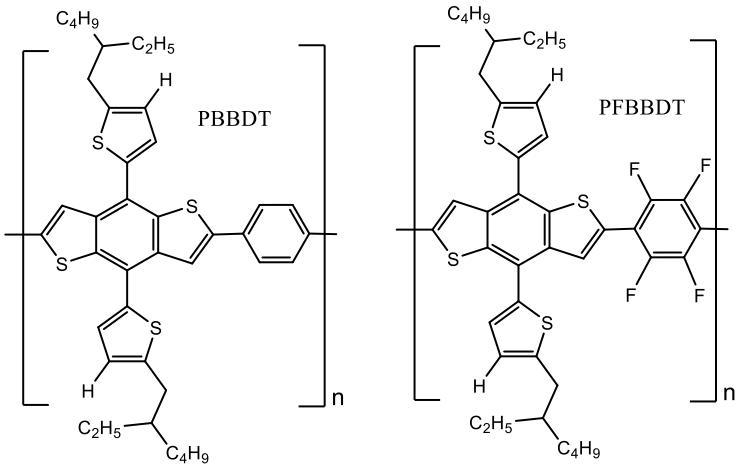

Figure 4-39: Reference polymer (PBBDT) and proposed fluorinated BDT-benzene polymer (PFBBDT) structures.

4.2.1 Density Functional Theory (DFT) Simulations

As summarized in Section 2.2.1, Avogadro software was used for the initial energy minimization estimate, and Gaussian software was used for the DFT calculation. The same settings were used for Gaussview: opt freq b3lyp/6-31g(d) geom=connectivity.

Since the polymer in this chapter has a fluorinated benzene A unit, a DFT calculation for an unsubstituted BDT-benzene dimer (PBBDT) was completed to provide a better comparison to

the fluorinated polymer (PFBBDT). The results for each polymer can be seen in **Figure 4-40**. This reference polymer (PBBDT) was previously reported to have an E_{HOMO} of -5.16 eV and a very wide bandgap of 2.27 eV.[55] DFT showed that PFBBDT is predicted to have a lower E_{HOMO} than the reference PBBDT, which means a HOMO level lower than -5.16 eV can be expected. This will positively impact the energy level matching of PFBBDT with Y6 and can allow for better V_{oc}. The predicted smaller bandgap could also help with energy level matching between PFBBDT and Y6. Interestingly, the dihedral angle of PFBBDT is 6 degrees less than the reference with an unsubstituted benzene.[55] Using Avogadro software, the distances between the fluorine atoms on the benzene ring and the hydrogen atoms on the subsequent thiophenes in the BDT structure were measured to be 2.21 and 2.22 Å. This distance coincides with hydrogen bonding and can explain why the structure is highly co-planar.[80] A highly co-planar structure will allow for extended conjugation, good morphology, and potentially improved charge transport. The DFT calculated values are summarized in **Table 4-21**.

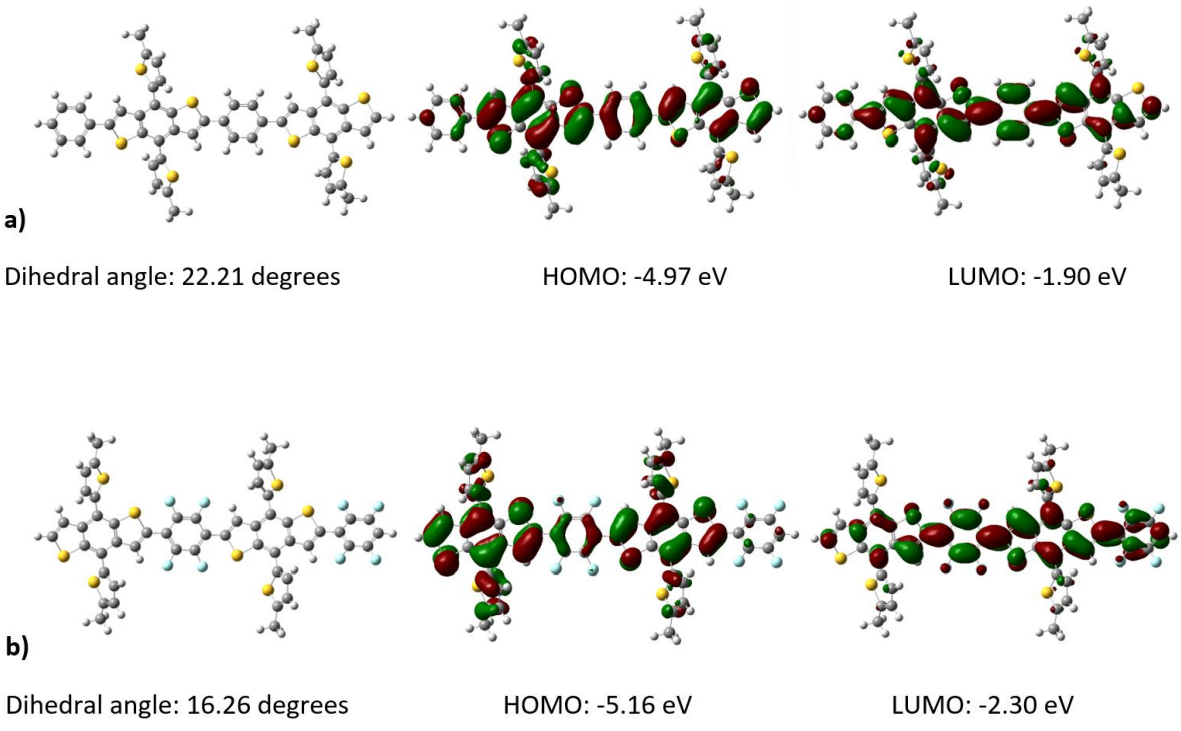

Figure 4-40: DFT calculation results showing overall structure, HOMO, LUMO, and dihedral angle for polymers: a) reference PBBDT; b) PFBBDT.

Table 4-21: DFT results for the reference polymer (PBBDT) and the proposed benzene-BDT polymer (PFBBDT).

Polymer	DFT E_{HOMO} (eV)	DFT E_{LUMO} (eV)	DFT Bandgap (eV)	DFT Dihedral Angle (degrees)
PBBDT	-4.97	-1.90	3.07	22.21
PFBBDT	-5.16	-2.30	2.86	16.26

4.2.2 Synthesis Scheme

Part of the merit of PFBBDT is the synthetic simplicity since the commercial monomer is already dibrominated. Therefore, the synthesis only involved a Stille coupling polymerisation step using anhydrous chlorobenzene as the solvent and a catalyst/ligand system of tris(dibenzylideneacetone)dipalladium(0) catalyst (Pd_2dba_3)/ tri(o-tolyl)phosphine ($(P(tol)_3$) reacted at 90 ^oC for 24 hours. The synthesis overview of this polymer can be seen in **Scheme 4-3** below and further synthesis details can be found in Section 4.8.3.

PFBBDT Synthesis

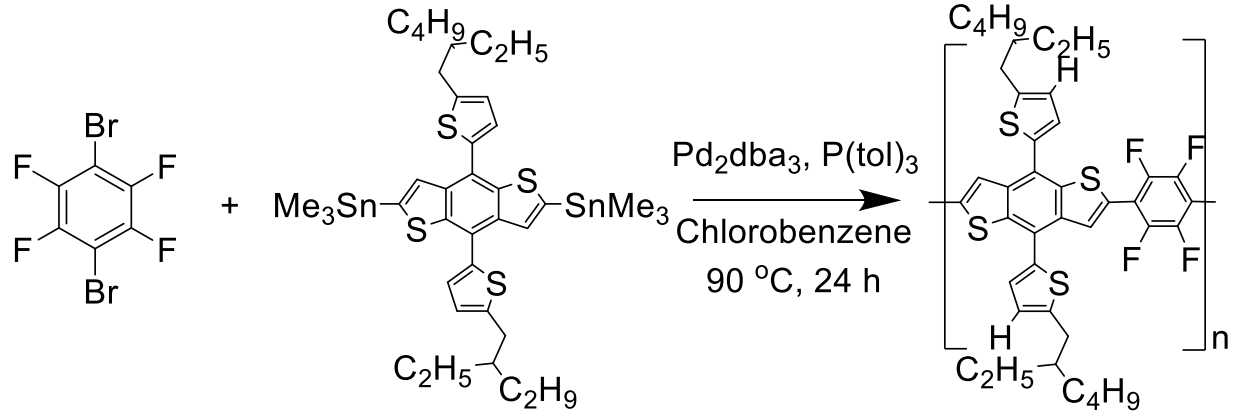

Scheme 4-3: Synthesis scheme for polymer PFBBDT.

4.3 Physical Properties

The molecular weight of PFBBDT was measured using HT-GPC. Polystyrene was used as a reference, with 1,2,4-trichlorobenzene as the eluent at an operation temperature of 150°. The M_n value was 4.41 kDa, whereas the M_w value was 6.01 kDa. This molecular weight is quite low, indicating an oligomer is formed. Studies have shown that low molecular weight leads to worse J_{sc} and FF, resulting in worse PCE.[81,82] In comparison, the reference polymer, PBBDT, was obtained with a M_n of 15.7 kDa.[55] Therefore, the fluorine atoms limit the solubility of this material, resulting in a lower degree of polymerization. Although the fluorine atoms have benefits for performance, including their strong EWG nature, the resulting low molecular weight will also negatively affect the performance. The performance of the OPV devices will provide insight into which aspect has the greater effect. A summary of the GPC data is in **Table 4-22** below.

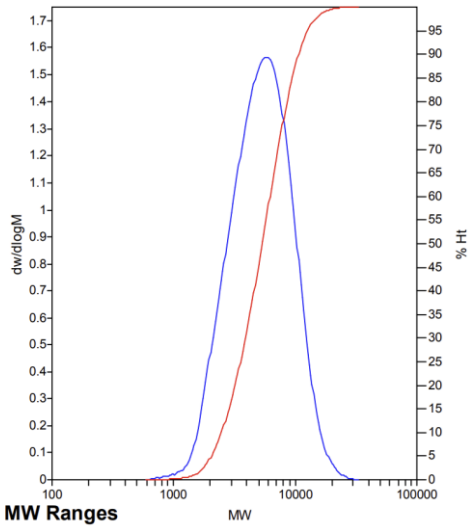

Figure 4-41: HT-GPC molecular weight distribution of polymer PFBBDT.

Table 4-22: HT-GPC molecular weight and PDI data summary for PFBBDT.

Polymer	M_n (kDa)	M_w (kDa)	PDI
PFBBDT	4.41	6.01	1.36

TGA for polymer PFBBDT was acquired using a heating rate of 10 °C/min under nitrogen (see **Figure 4-42**). A weight loss of 1 % was observed at 336 °C and the first step decomposition occurred at 408 °C. PFBBDT displayed excellent thermal stability, making it an ideal candidate for elevated temperature OSC applications.

DSC was acquired using a scanning rate of 10 °C/min under nitrogen, where the first cycle went 50 °C lower than the second cycle and the second cycle went until the polymer lost 0.5 % of its weight in TGA (see **Figure 4-43**). PFBBDT displayed a glass transition temperature around 36 °C and a melting temperature at 113 °C in the first heating cycle. The melting temperature increased to 152 °C in the second heating cycle. The melting temperatures could be visible in this region due to the low molecular weight of this material. Furthermore, PFBBDT showed a cold crystallization in the first heating cycle at 100 °C. These peaks indicate this polymer has some crystalline characteristics, which is abnormal for this type of conjugated polymer and can be detrimental to OPV performance.

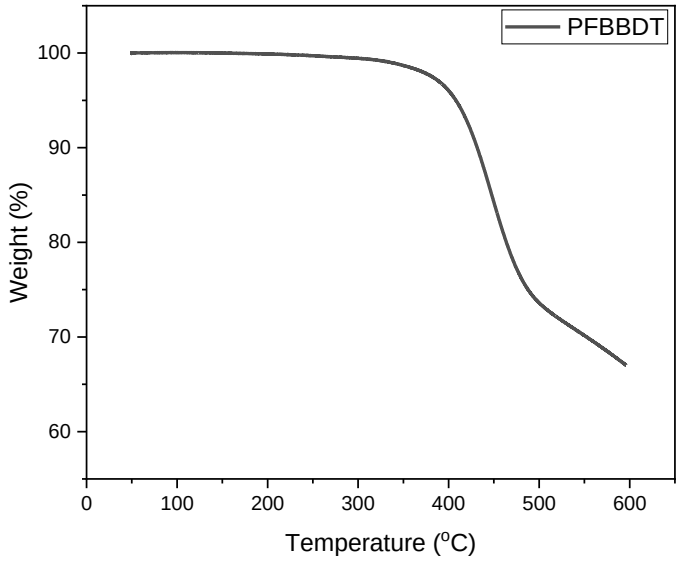

Figure 4-42: TGA curve for polymer PFBBDT.

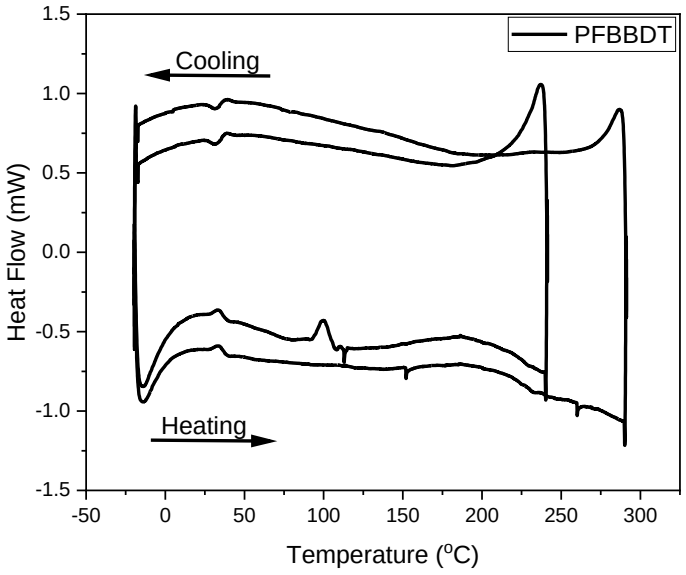

Figure 4-43: DSC curve for polymer PFBBDT.

4.4 Opto-Electrochemical Properties

UV-vis and CV samples were prepared according to the procedure outlined in Section 2.4. Polymer PFBBDT had a trimodal absorption spectrum (see **Figure 4-44**), which reflected the benzene-BDT base unit structure, and was also observed by Zhang et al..[55] PFBBDT had a $\lambda_{max,s}$ of 490 nm. A redshift of λ_{max} to 543 nm was observed for a PFBBDT thin film. However, in solution the middle peak has the maximum absorption, whereas as a thin film the right peak has the maximum absorption. Therefore, the right peak in solution was at 533 nm, corresponding to an actual spectrum redshift of 10 nm when applied as a thin film. The increase in absorption intensity of the right peak indicated the polymer adopts a more co-planar orientation as a thin film, which subsequently results in improved conjugation. The optical bandgap for PFBBDT was calculated as 2.13 eV, which could potentially be too wide for good energy level matching with Y6.

From CV, an E_{HOMO} level of -5.52 eV was obtained for PFBBDT. From **Figure 2-15**, the E_{HOMO} appears to be well matched with Y6; however, due to the relatively large bandgap, the E_{LUMO} of -3.39 eV might be too low for good matching with Y6. **Figure 4-46** shows a comparison between the DFT calculated energy levels and the energy levels obtained from CV. DFT agreed with CV for PFBBDT since the E_{HOMO} was lower and the bandgap was smaller than the reference polymer, PBBDT, which is promising for OSC applications.

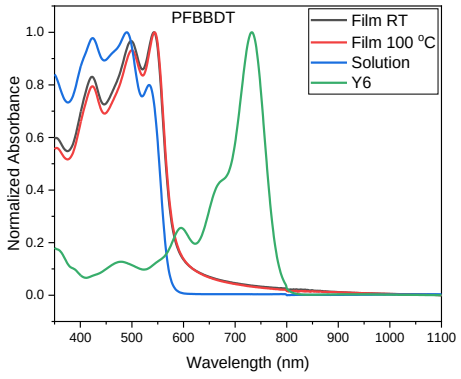

Figure 4-44: UV-vis absorption spectra of as-cast thin film, annealed thin film, and chloroform solution for polymer PFBBDT.

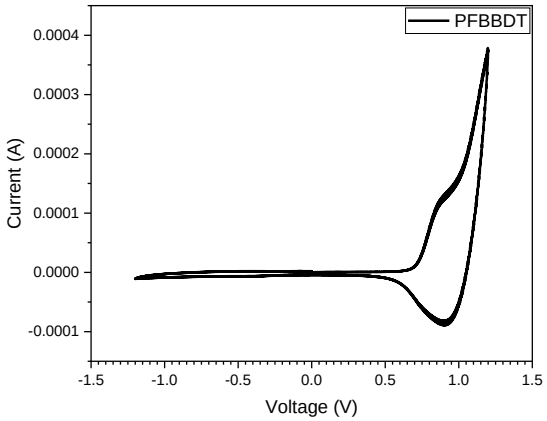

Figure 4-45: CV profile of polymer PFBBDT.

Table 4-23: Optical and electrochemical properties of polymer PFBBDT.

Polymer	$\lambda_{max,s}$ (nm)	$\lambda_{max,fRT}$ (nm)	$\lambda_{max,f100C}$ (nm)	λ_{onset} (nm)	E_g^{opt} (eV)	E_{HOMO} (eV)	E_{LUMO} (eV)
PFBBDT	490	543	544	582	2.13	-5.52	-3.39

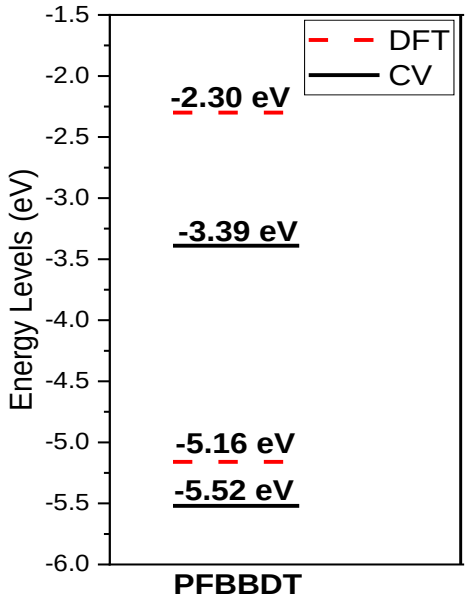

Figure 4-46: Comparison of DFT predicted HOMO and LUMO energy levels with CV obtained HOMO and LUMO levels for PFBBDT.

PL was acquired using the same method described in Section 2.4 (see **Figure 4-47**). Due to the favourable characteristics and strong performance of Y6 for OSC applications, Y6 was used as the commercial NFA for pairing with PFBBDT. PFBBDT showed good quenching in the donor region (99.9 %); however, the acceptor region resulted in insufficient quenching (71.5 %). This result reflected the energy level concerns for PFBBDT due to the abnormally large optical bandgap resulting in a very high E_{LUMO}.

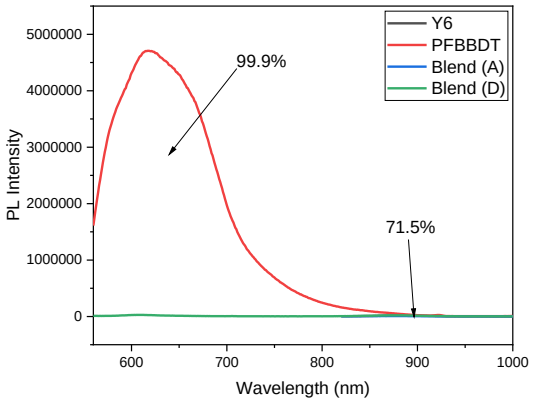

Figure 4-47: Photoluminescence spectrum of PFBBDT with Y6.

4.5 OPV Performance and Charge Mobility

A detailed device fabrication procedure can be found in Section 2.8.2.

Important note: *The polymer in this chapter was tested with a new device ITO pattern and testing system. In the past devices have achieved a FF of 0.56 by Yuan et al. and as high as 0.71 by Jiang et al. in our lab.*[52,53] *Furthermore, a shunt resistance of 883 ohm•cm*^{2} *and a series resistance of 2.84 ohm•cm*^{2} *have been reported by our group.*[53] *However, after switching to the new system, the FF is lower than previously achieved, which is related to issues with low shunt resistance and high series resistance. This indicates that there is a problem with one or more of the layers and/or interfaces between layers, which is still being investigated by our group. Therefore, the data presented below might not represent the best data possible for this polymer.*

Summaries of the performance of PFFBDT with Y6 can be found in **Table 4-24** and **Table 4-25**, and the best J-V curve is shown in **Figure 4-48**. It is worth noting that the active layer was quite thin for these polymers, likely caused by the low molecular weight. Therefore, further testing with a higher concentration in the active layer solution is necessary. Polymer PFBBDT achieved a highest PCE of 5.14 % (J_{sc} = 16.77 mA/cm^2, V_{oc} = 0.74 V, and FF = 0.41) with the active layer annealed at 50 ^{o}C. A slight increase in PCE was observed for this polymer with moderate annealing temperatures; however, higher annealing temperatures did not provide improvements. Presence of the melting point in DSC could explain why annealing at higher temperatures did not improve performance. The J_{sc} for this polymer is adequate but the V_{oc} and FF are low. Voltage losses for this polymer is calculated as 0.68 V according to **Eq. 12.** The high voltage losses and low FF are potentially caused by the highly intense lamellar stacking observed for this polymer, which will be explained further in Section 4.6. Due to the hydrogen bonding between the fluorine and hydrogen atoms in the polymer backbone (as shown in the DFT calculations), the polymer strongly packs with an edge-on orientation. This might result in large domain sizes and aggregates forming due to the strong attraction of fellow polymer chains, which could lead to surface roughness that would negatively affect the charge transfer, resulting in more recombination (lowering FF and V_{oc}). Furthermore, the low molecular weight is not ideal for OPV performance and could be contributing to the poor FF and V_{oc}.[81]

EQE of the polymer was measured, where PFBBDT had a maximum EQE of 64 % at 540 nm. The error for PFBBDT between OPV and EQE for J_{sc} was 6.05 %, which is reasonable.

Table 4-24: Summary of OSC device parameters for PFBBDT:Y6.

Device	Annealing Temperature (°C)	RPM	Thickness (nm)
1	No annealing	1500	68.90 (±0.60)
2	No annealing	2000	59.20 (±0.90)
3	No annealing	2500	50.00 (±0.20)
4	50	1500	66.35 (±0.45)
5	50	2000	55.85 (±0.95)
6	50	2500	50.05 (±0.35)
7	100	1500	68.60 (±0.60)
8	100	2000	60.60 (±0.60)
9	100	2500	55.05 (±0.55)
10	150	1500	69.35 (±0.35)
11	150	2000	55.65 (±0.65)
12	150	2500	49.65 (±0.55)

Table 4-25: Summary of OSC performance for PFBBDT:Y6.

Device	Jsc (mA/cm^2)	Voc (V)	FF	PCE (%)	Avg. Rsh ($ohm•cm^2$)	Avg. Rs ($ohm•cm^2$)
1	16.52 (15.68±0.85)	0.74 (0.74±0.01)	0.37 (0.37±0.01)	4.61 (4.27±0.26)	128 (±22)	9.20 (±4.27)
2	16.52 (16.57±0.45)	0.75 (0.74±0.01)	0.40 (0.39±0.01)	5.00 (4.76±0.20)	160 (±13)	7.13 (±1.46)
3	16.33 (15.86±0.63)	0.74 (0.73±0.02)	0.40 (0.38±0.02)	4.84 (4.44±0.46)	182 (±10)	11.31 (±6.71)
4	16.72 (15.61±0.76)	0.75 (0.74±0.01)	0.37 (0.36±0.01)	4.61 (4.12±0.30)	116 (±11)	12.95 (±5.18)
5	16.28 (15.40±0.78)	0.73 (0.73±0.01)	0.39 (0.37±0.02)	4.62 (4.16±0.39)	146 (±24)	11.56 (±6.95)
6	16.77 (14.94±1.49)	0.74 (0.73±0.01)	0.41 (0.41±0.02)	5.14 (4.49±0.37)	232 (±31)	9.57 (±2.00)
7	16.71 (15.97±0.61)	0.73 (0.73±0.01)	0.38 (0.37±0.01)	4.64 (4.35±0.24)	124 (±7)	8.62 (±2.94)
8	16.69 (16.29±0.47)	0.75 (0.73±0.01)	0.40 (0.39±0.01)	5.02 (4.63±0.29)	160 (±10)	6.45 (±1.65)
9	17.20 (15.52±0.85)	0.75 (0.73±0.01)	0.40 (0.40±0.02)	5.08 (4.48±0.34)	185 (±37)	8.65 (±3.30)
10	16.76 (16.17±0.52)	0.71 (0.70±0.01)	0.39 (0.38±0)	4.62 (4.37±0.21)	122 (±2)	6.38 (±1.03)
11	15.80 (15.62±0.19)	0.71 (0.70±0.02)	0.40 (0.39±0.01)	4.50 (4.23±0.27)	141 (±14)	6.41 (±0.42)
12	16.43 (15.62±0.50)	0.72 (0.70±0.02)	0.41 (0.40±0.01)	4.86 (4.31±0.32)	163 (±7)	4.86 (±0.41)

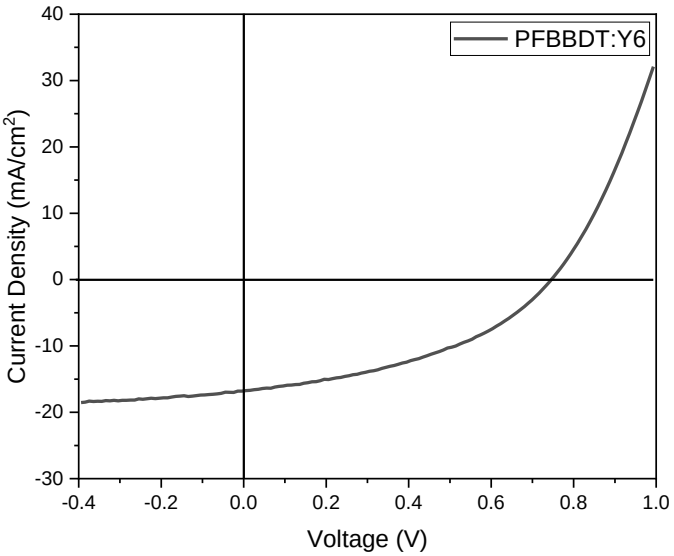

Figure 4-48: J-V curve for PFBBDT:Y6 (50 ^{o}C).

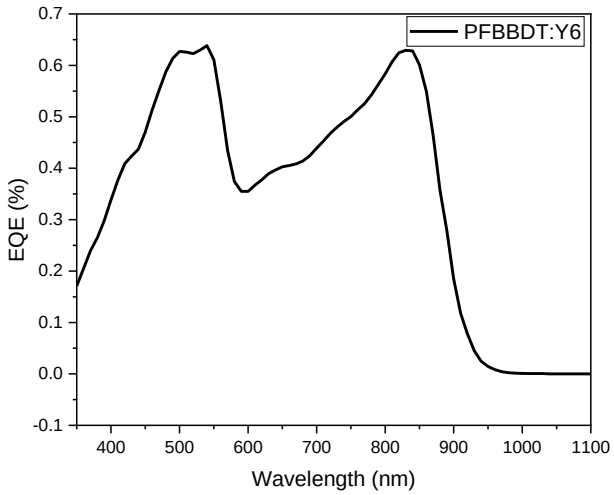

Figure 4-49: EQE of best performing OSC based on PFBBDT:Y6.

Table 4-26: Comparison of Jsc values obtained from OPV and EQE measurements for PFBBDT.

Polymer	Jsc from OPV (mA/cm^2)	Jsc from EQE (mA/cm^2)	Error (%)
PFBBDT	17.19	16.21	6.05

Devices for SCLC mobility were prepared and tested as previously described in Section 2.5. Polymer PFBBDT showed a hole mobility of 7.53×10^{-5} $cm^2V^{-1}s^{-1}$ as a neat polymer film, which decreased to 1.59×10^{-6} $cm^2V^{-1}s^{-1}$ when mixed with Y6. The electron mobility was 6.28×10^{-6} $cm^2V^{-1}s^{-1}$, resulting in a mobility ratio of 3.95. The low mobility and considerable ratio could be caused by the intense lamellar packing of PFBBDT as described in Section 4.6 below, which is not ideal for vertical charge transfer and could result in considerable aggregation. Furthermore, the low molecular weight could also be causing issues with mobility.

Table 4-27: SCLC hole and electron mobilities for the neat polymer and D:A blend film of PFBBDT and Y6.

Polymer	μ_e ($x10^{-4}$ $cm^2V^{-1}s^{-1}$)	μ_h ($x10^{-4}$ $cm^2V^{-1}s^{-1}$)	μ_e/μ_h
PFBBDT	N/A	0.753 (0.689)	N/A
PFBBDT:Y6	0.0628 (0.0300)	0.0159 (0.00989)	3.95 (3.03)

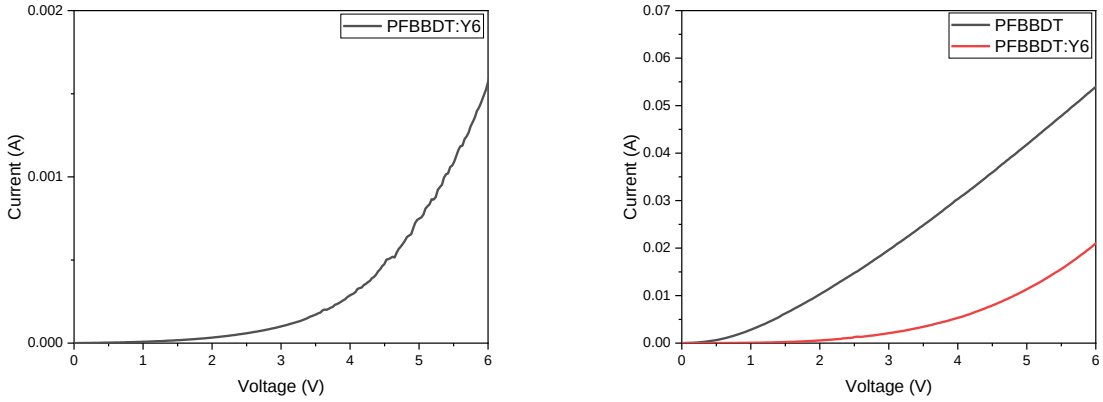

Figure 4-50: Left: electron mobility I-V curve of PFBBDT:Y6; Right: hole mobility I-V curves of PFBBDT and PFBBDT:Y6.

4.6 Crystallinity

Figure 4-51 shows the 1D and 2D XRD plots and images for PFBBDT as a neat polymer and as a blend film with Y6. The in-plane plots of the neat and blend films display no obvious peaks. However, the neat polymer shows very intense lamellar peaks in the out-of-plane plot. A ring can also be seen in the 2D image indicating this lamellar peak. The peak appears when $2\theta = 4.37$, which corresponds to a d-spacing of 2.02 nm. As seen in **Figure 4-51**, the most intense peak occurs when annealed at 100 ^{o}C for the neat polymer, followed by 200, and 150 ^{o}C. The intensity of the peaks for room temperature and 50 ^{o}C is much less than when annealed at higher temperatures. Lamellar peaks can also be observed in the blend film out-of-plane plot; however, the intensity is much less. These peaks are slightly shifted to $2\theta = 4.52$, corresponding to a d-spacing of 1.95 nm. For the blend film, the peak intensity appears to increase with annealing temperature, aside from 150 ^{o}C, which is less intense than 100 ^{o}C. The lamellar packing results in an edge-on orientation, which is not preferred for OSCs. Strong lamellar packing can cause large domains, which could be limiting the performance of this material. Due to the intense lamellar features, especially in the neat polymer film, charge transfer in the horizontal direction could be much better than the vertical, which could make this material a strong candidate for transistor applications instead of OSCs.

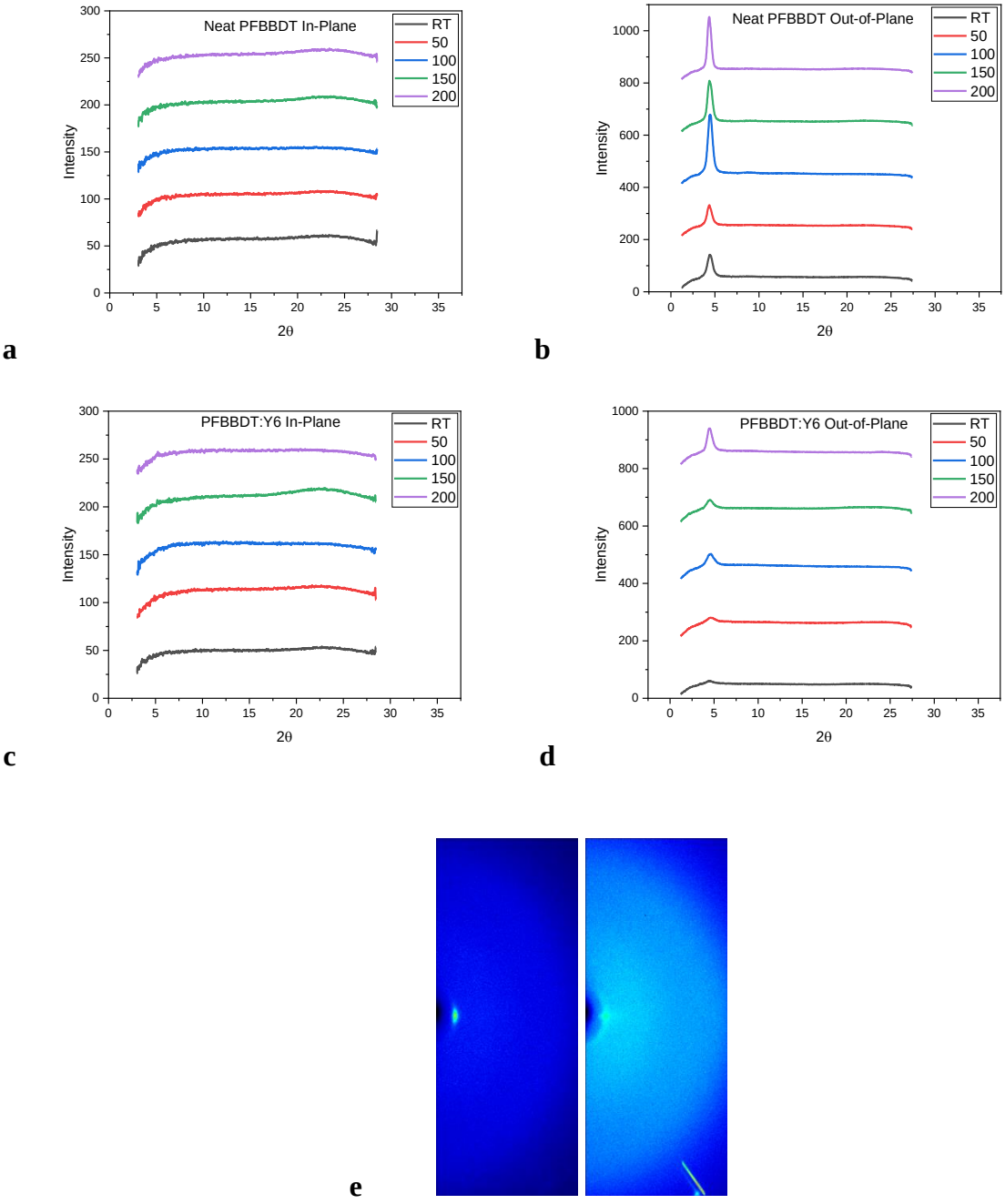

Figure 4-51: GIXD patterns of films at different annealing temperatures: a) in-plane neat PFBBDT; b) out-of-plane neat PFBBDT; c) in-plane PFBBDT:Y6 blend; d) out-of-plane PFBBDT:Y6 blend; e) 2D images of the best performing material (annealed at 50 ^{o}C), where the left is neat PFBBDT and the right is PFBBDT:Y6.

4.7 Summary and Future Direction

In summary, a novel D-A polymer consisting of a benzene-BDT backbone was synthesized in a single-step reaction scheme. PFBBDT was inspired by a related benzene-BDT-based polymer, which was used as a hole transfer layer in perovskite solar cells. The addition of fluorine groups was used to lower the E_{HOMO}, resulting in a promising material for OSC applications. DFT calculations predicted this polymer to have a lower E_{HOMO} and smaller dihedral angle than the reference polymer PBBDT. PFBBDT had quite low molecular weight, indicating an oligomer structure. This polymer was thermally stable, displaying a wide bandgap, and low E_{HOMO}. PFBBDT showed good PL quenching in the donor region but only moderate quenching in the acceptor region. In terms of OPV performance, PFBBDT achieved a best PCE of 5.14 % (J_{sc} = 16.77 mA/cm^2, V_{oc} = 0.74 V, and FF = 0.41) with the active layer annealed at 50 ^{o}C. PFBBDT had low electron and hole SCLC mobility, while also having non-ideal mobility balance. This polymer showed very intense lamellar stacking peaks indicating the active layer has an edge-on structure. Due to hydrogen bonding in the polymer donor, the highly intense lamellar stacking could cause aggregation, and potentially contributes to the low mobility and performance of this material. Furthermore, the low molecular weight can negatively effect the OPV performance Based on the results obtained, this polymer structure is not good for OPV applications but has potential for transistor applications due to the lamellar packing structure.

For future work, the surface roughness of the active layer can be examined using AFM. AFM can also provide the domain sizes to assess if there are any issues with aggregation caused by the intense lamellar stacking that may be limiting the performance. Optimization of the polymerization is necessary to improve the molecular weight through various strategies including a different catalyst, higher temperature, longer reaction time, catalytic amount of copper iodide, etc. A spacer molecule such as thiophene, with a solubilizing side chain could be used to improve the solubility of the polymer, which could result in higher molecular weight. Finally, PFBBDT can be tested as a transistor since the strong edge-on orientation should result in high horizontal charge transfer.

4.8 Experimental Section

4.8.1 Materials Characterization

The chemicals and solvents used for synthesis were purchased from commercial vendors including Fluka, Armstrong, Sigma-Aldrich, TCI, and VWR without further purification. The reaction used anhydrous chlorobenzene purchased from Sigma-Aldrich. Y6 and 1,1'-[4,8-bis[5-(2-ethylhexyl)-2-thienyl]benzo[1,2-b:4,5-b']dithiophene-2,6-diyl]bis[1,1,1-trimethylstannane] (BDT) were both purchased from 1-Material. Specific synthesis details will be shown in Section 4.8.3 below. The characterization and testing of the polymer were done using the same equipment as specified in Section 2.8.1.

4.8.2 OSC Device Fabrication and Characterization

The OSC fabrication and characterization was completed according to the information provided in Section 2.8.2.

4.8.3 Synthesis Routes

Synthesis of polymer PFBBDT

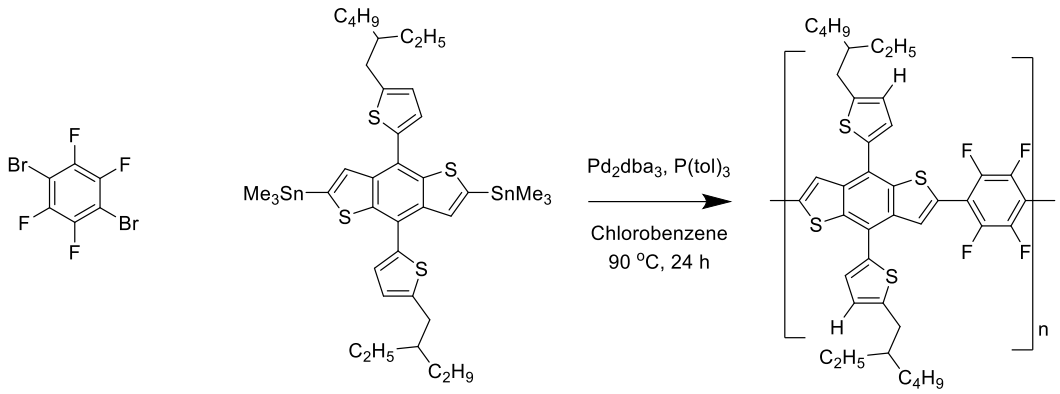

The monomer (1 equiv.), tri(o-tolyl)phosphine ((P(tol)$_3$) (0.08 equiv.), and 1,1'-[4,8-bis[5-(2-ethylhexyl)-2-thienyl]benzo[1,2-b:4,5-b']dithiophene-2,6-diyl]bis[1,1,1-trimethylstannane] (BDT) (1 equiv.) were added to a 2-neck 25 mL round-bottom flask with a small stir bar. The system was purged with argon by performing 3 vacuum cycles. Anhydrous chlorobenzene was added (4 mL). Tris(dibenzylideneacetone)dipalladium(0) catalyst (Pd_2dba_3) (0.04 equiv.) was measured in an inert atmosphere such as a nitrogen filled glove bag. A 1 mL solution of the catalyst was dissolved in chlorobenzene and added to the flask. The contents were reacted at 90 ^oC for 24 hours. After, the reaction was cooled to room temperature and then stirred in 150 mL of methanol for 30 minutes or an hour. The solid was collected via vacuum filtration and then washed with solvents in the following order: acetone, hexane, chloroform, and chlorobenzene in a Soxhlet extractor. (Yield: 75.7 mg in chloroform, 50.5 %).

Chapter 5: Study of an Acid-Catalyzed Post Polymerization Modification on an Acetal to Yield a Simple, Low-Cost Aldehyde-Substituted BDT-Based Polymer

5.1 Introduction

Research on OSCs has largely focused on improving performance, which has driven considerable progress in the field of OSCs. However, commercialization will also require long-term stability, large area device fabrication, low-cost materials development, and environmentally friendly synthesis. Therefore, the research focus in the field of OSCs must expand to target other crucial factors.

Simple, cost-effective synthesis routes are critical for developing materials that can be profitable. Research has been increased in this area with example systems of an MO-IDIC-2F acceptor and PTQ10 low-cost donor, and BTzO-4F acceptor with PBDB-T donor, which have shown PCEs greater than 13%.[17] In Chapters 2 and 3, a common, simple but effective backbone structure of BDT co-polymerised with thiophene was implemented. As previously mentioned, side chain engineering is critical for balancing solubility with performance. Inexpensive side chain substitution on the thiophene unit, through synthetically simple reactions could lead to marketable technology.

Carbonyl groups are commonly used EWGs for D-A polymer donor design. An inexpensive, commercially available thiophene option with a carbonyl substitution is 3-thiophenecarboxaldehyde. Previously, our group has attempted to dibrominate this material and co-polymerise with BDT directly; however, this Stille Coupling reaction resulted in an insoluble polymer in common chlorinated processing solvents (e.g., chloroform, chlorobenzene, etc.).

Developing an alternative synthesis route to obtaining the aldehyde-substituted thiophene-BDT polymer is of interest to take advantage of the formaldehyde EWGs potential properties. Alkoxy chains are another well known EWG.[1] Aldehyde groups can be converted to acetals through simple chemistry using alcohols, and can be easily reverted back to an aldehyde via an acid or base. This method has potential to synthesize a soluble form of the aldehyde-substituted thiophene-BDT polymer, while also providing a second novel polymer with an acetal side chain.

Therefore, this chapter will investigate the use of an acetal side chain on thiophene for a novel D-A polymer donor, as well as a post polymerization modification to form another novel polymer, where the acetal chain is converted to an aldehyde using an acid. The aldehyde will potentially have better co-planarity, leading to better properties and performance.

5.2 Polymer Structure Design

The proposed acetal-substituted thiophene-BDT polymer was studied via DFT to confirm its potential for OSC applications using the methods described in Section 2.2. Not only is the acetal a good EWG, but it should also provide sufficient solubility in chloroform for polymer extraction and processing. Furthermore, this group can be cleaved via acid to form an aldehyde. Previously our group has had solubility issues when trying to prepare a polymer directly from 2,5-dibromo-3-carboxaldehyde thiophene with BDT; therefore, if after acid cleavage the polymer is soluble in chloroform, it is a way to make a second novel material using a post polymerization modification. This chapter will investigate the two novel polymers seen in **Figure 5-52** to assess their applicability as wide bandgap D-A polymers for OSC devices.

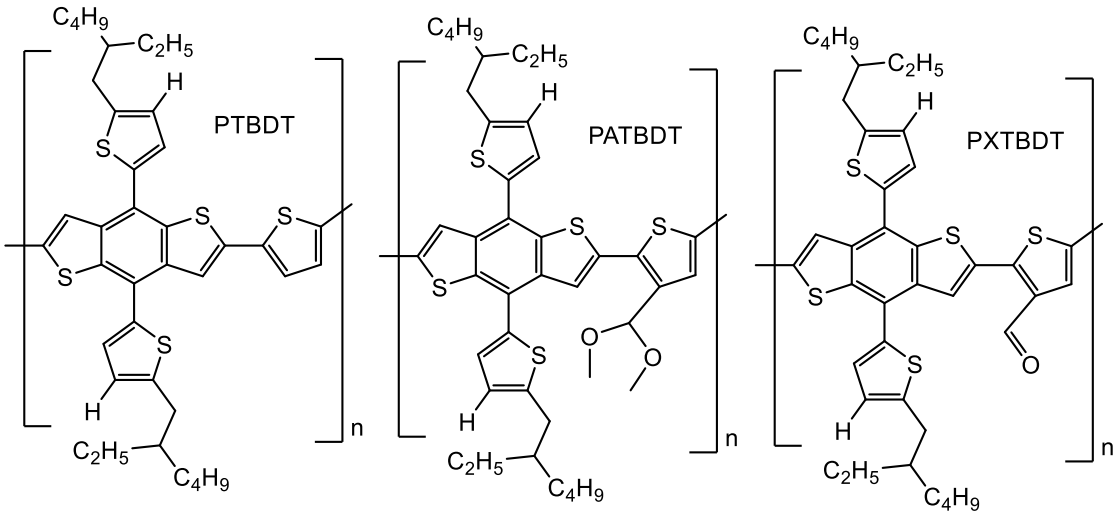

Figure 5-52: Polymer structures of a reference polymer (PTBDT) and two proposed polymers: an acetal-substituted (PATBDT) and a formaldehyde-substituted (PXTBDT) thiophene-BDT, where the "X" indicates the acetal has been cleaved and converted to an aldehyde.

5.2.1 Density Functional Theory (DFT) Simulations

DFT simulations were completed using Avogadro software for the initial energy minimization estimate, and Gaussian software for the DFT calculation. The same settings as previous chapters were used for Gaussview: opt freq b3lyp/6-31g(d) geom=connectivity.

Both the acetal (PATBDT) and aldehyde (PXTBDT) substituted thiophene-BDT dimers were assessed by comparing with an unsubstituted thiophene-BDT dimer, PTBDT. The results for each polymer can be seen in **Figure 5-53**. Both polymers were predicted to have lower E_{HOMO}

levels, with the aldehyde group of PXTBDT showing strong EWG capabilities due to its substantially lower calculated E_{HOMO}. PATBDT is calculated to have a larger bandgap than PTBDT and the electrons look evenly delocalized, which suggests good charge transfer and potential for π-π stacking. PXTBDT shows an uneven delocalization of electrons, favouring the right side of the molecule. This could potentially have negative effects on charge transfer and performance of this material. The DFT calculated values are summarized in **Table 5-28**.

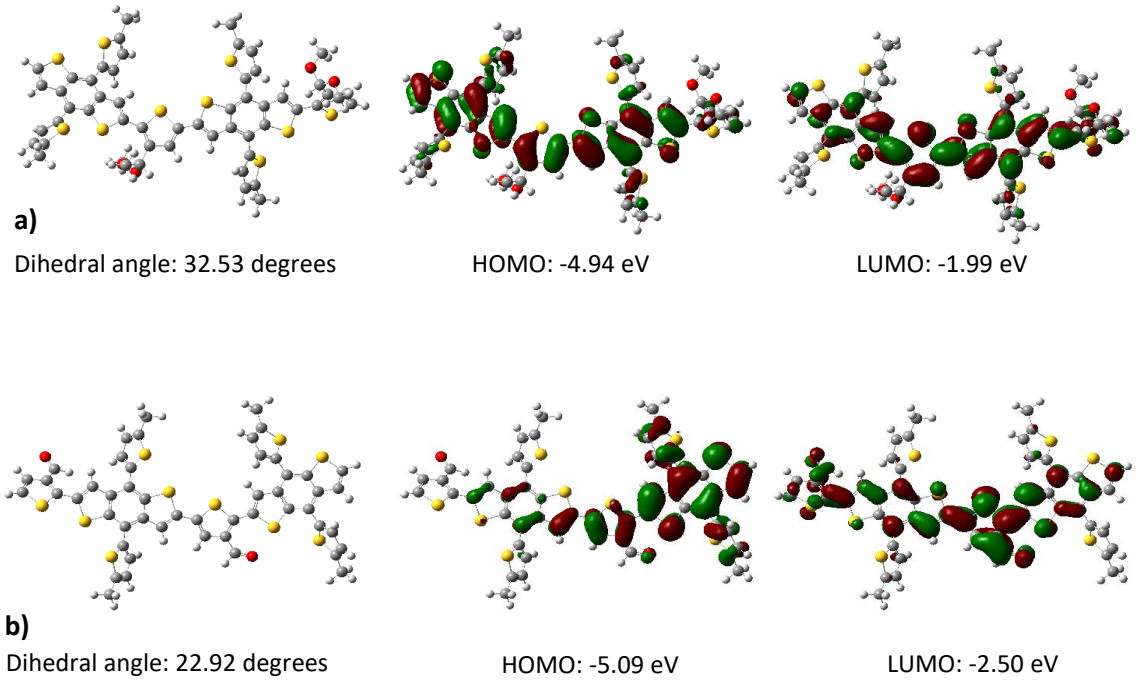

Figure 5-53: DFT calculation results showing overall structure, HOMO, LUMO, and dihedral angle for polymers: a) PATBDT; b) PXTBDT.

Table 5-28: DFT results for the reference polymer, PTBDT, and proposed polymers, PATBDT and PXTBDT.

Polymer	DFT E_{HOMO} (eV)	DFT E_{LUMO} (eV)	DFT Bandgap (eV)	DFT Dihedral Angle (degrees)
PTBDT	-4.79	-2.02	2.77	12.29
PATBDT	-4.94	-1.99	2.95	32.53
PXTBDT	-5.09	-2.50	2.59	22.92

5.2.2 Synthesis Scheme

The synthesis of PATBDT was a two-step process. First, an acid-catalyzed acetal formation reaction was completed starting from 2,5-dibromo-3-carboxaldehyde thiophene, where methanol was used as both a solvent and reagent. This monomer was then co-polymerised with BDT using the same Stille coupling conditions mentioned in Chapter 4 to yield the polymer, PATBDT. From PATBDT, the polymer PXTBDT can be produced via a post polymerisation modification in which acid is used to convert the acetal group back to an aldehyde. This polymer was then neutralized with pyridine in a methanol solution. **Figure 5-54** shows ^{1}H NMR of both PATBDT and PXTBDT. In the PATBDT spectrum, there is a peak at 3.47 ppm, which corresponds to the hydrogen attached to the carbons neighbouring the oxygen atoms in the acetal side chain. In the PXTBDT spectrum, this peak is nearly completely removed, indicating the acetal chain was successfully cleaved.

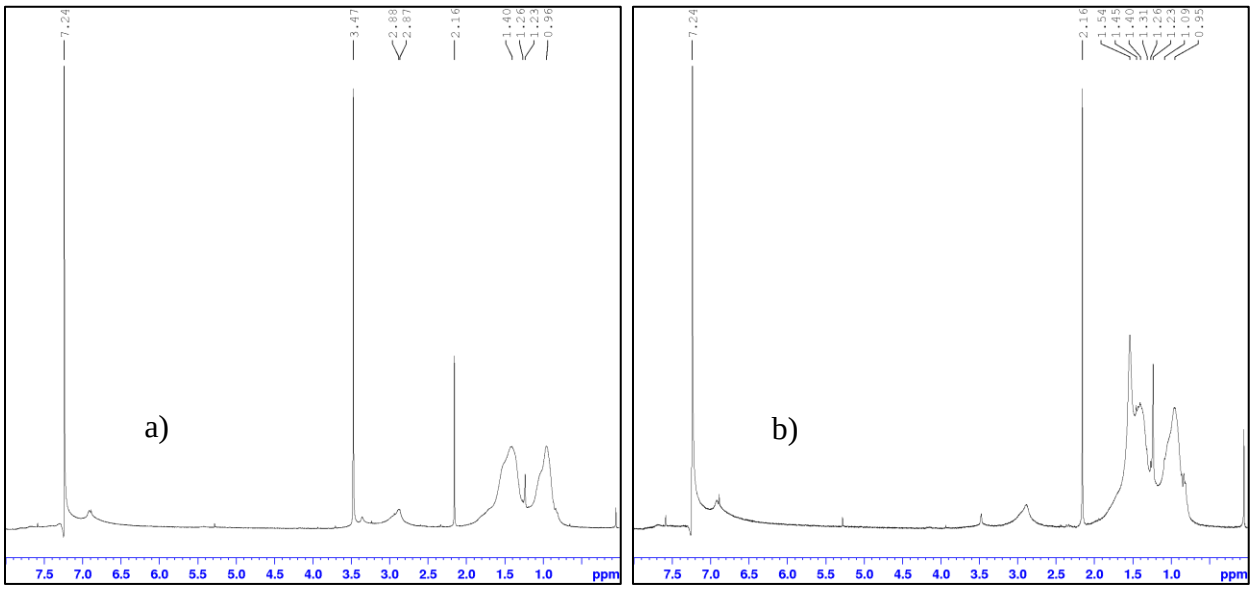

Figure 5-54: a) ^{1}H NMR of PATBDT; b) ^{1}H NMR of PXTBDT.

The synthesis overview of these two polymers can be seen in **Scheme 5-4** below and further synthesis details can be found in Section 5.8.3.

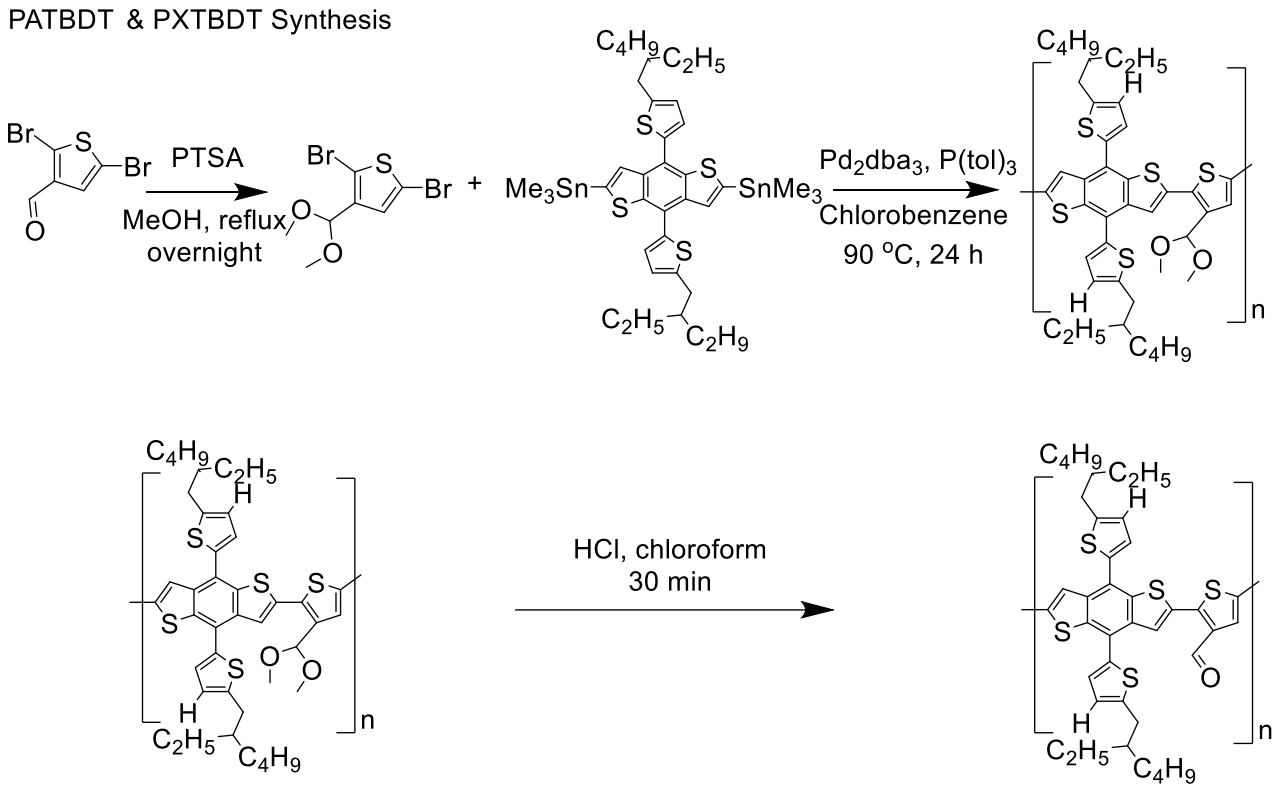

Scheme 5-4: Synthesis scheme for polymers PATBDT, and PXTBDT.

5.3 Physical Properties

The molecular weights of the polymers were measured using HT-GPC. Polystyrene was used as a reference, with 1,2,4-trichlorobenzene as the eluent at an operation temperature of 150°. The M_n values were 22.2, and 24.0 kDa, whereas the M_w values were 47.5, and 49.3 kDa for PATBDT and PXTBDT, respectively. The PDIs are 2.14, and 2.06, respectively. A summary of the GPC data is in **Table 5-29** below.

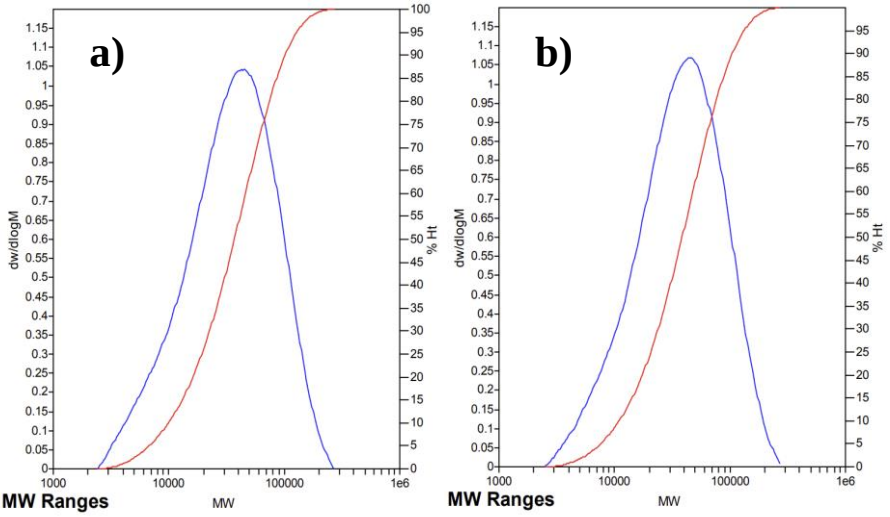

Figure 5-55: HT-GPC molecular weight distribution of polymer: a) PATBDT; b) PXTBDT.

Table 5-29: HT-GPC molecular weight and PDI data summary for PATBDT and PXTBDT.

Polymer	M_n (kDa)	M_w (kDa)	PDI
PATBDT	22.2	47.5	2.14
PXTBDT	24.0	49.3	2.06

Like Chapters 2 through 4, TGA for polymers PATBDT, and PXTBDT was acquired using a heating rate of 10 °C/min under nitrogen (see **Figure 5-56**). A weight loss of 1 % was observed at 313, and 265 °C for PATBDT, and PXTBDT, respectively. The first step decomposition occurred at 376, and 358 °C, respectively. These polymers displayed excellent thermal stability making them ideal candidates for high temperature OSC applications.

DSC was acquired using a scanning rate of 10 °C/min under nitrogen, where the first cycle went 50 °C lower than the second cycle and the second cycle went until the polymer lost 0.5 % of its weight in TGA (see **Figure 5-57**). Both polymers displayed a glass transition temperature around

36 ^{o}C. PATBDT and PXTBDT do not show any additional significant peaks in their respective DSC curves. However, PXTBDT shows an irreversible transition in the first heating cycle beginning around 106 ^{o}C.

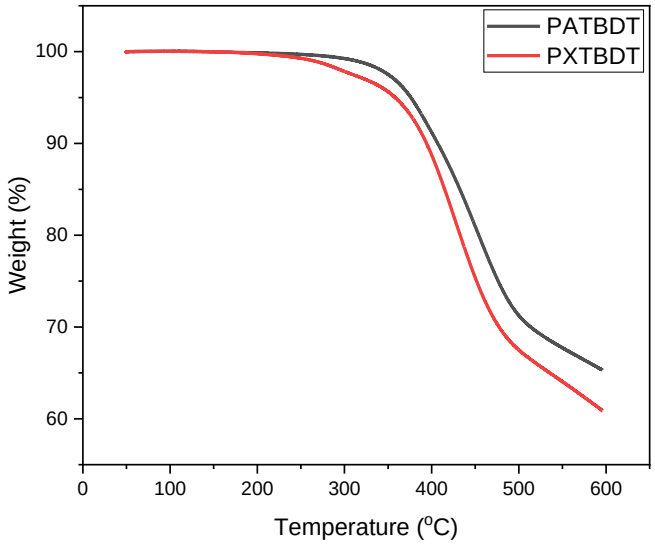

Figure 5-56: TGA curves for polymers: PATBDT, and PXTBDT.

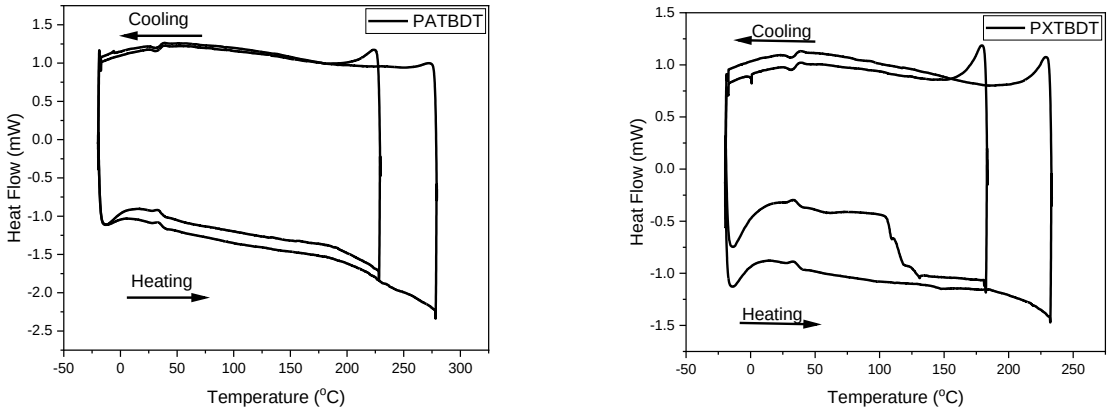

Figure 5-57: DSC curves for polymers: PATBDT, and PXTBDT.

5.4 Opto-Electrochemical Properties

UV-vis and CV samples were prepared according to the procedure outlined in Section 2.4. PATBDT had a $\lambda_{max,s}$ of 505 nm, which shifted to 517 nm when cast as a thin film. Furthermore, in solution there was a very weak shoulder peak, which became nearly as intense as the maximum absorption peak for a thin film. This indicated a strong shift to better co-planarity and improved conjugation, likely caused by a better orientation of the acetal side chain. Unlike PATBDT, PXTBDT only had one peak in its spectra. The $\lambda_{max,s}$ for PXTBDT was 532 nm, which was redshifted to 550 nm as a thin film. PXTBDT had an optical bandgap of 1.94 eV, which was not as wide as PATBDT (2.06 eV).

From CV, an E_{HOMO} level of -5.55 eV was obtained for PATBDT, while PXTBDT had a much lower E_{HOMO} of -5.67 eV. This indicated that the aldehyde side chain is a strong EWG and resulted in an energy level that is quite close to Y6 (<0.1 eV HOMO offset), which could have a negative effect on the performance. However, studies have shown that good PCE can be obtained with minimal HOMO level offset. For example, Li et al. studied the effect of the HOMO offset and showed that even with an offset of 0 eV, a PCE of 10.42 % was achieved, while with an offset of 0.06 eV, a PCE of 11.75 % was achieved.[83] Furthermore, Chen et al. showed a PCE of 10.4 % could be achieved with their material despite a HOMO offset of 0.09 eV.[84] As the HOMO level offset decreases, the energy losses typically decrease; however, since the offset is the driving force, the driving force is also reduced. [83] A strong EWG, like the aldehyde in PXTBDT, can help overcome this small driving force.[83] Furthermore, Li et al. found that only a small offset was required to have good hole transfer.[83] Therefore, although the HOMO offset with Y6 is quite low for PXTBDT, previous studies indicate that it still could have potential for OSC applications.

The opto-electrochemical data is summarized in **Table 5-30**. **Figure 5-60** shows a comparison between the DFT calculated energy levels and the energy levels obtained from CV. DFT correctly predicted that the E_{HOMO} of PXTBDT would be significantly lower than PATBDT. Likewise, the bandgap for PXTBDT was smaller, which agreed with DFT.

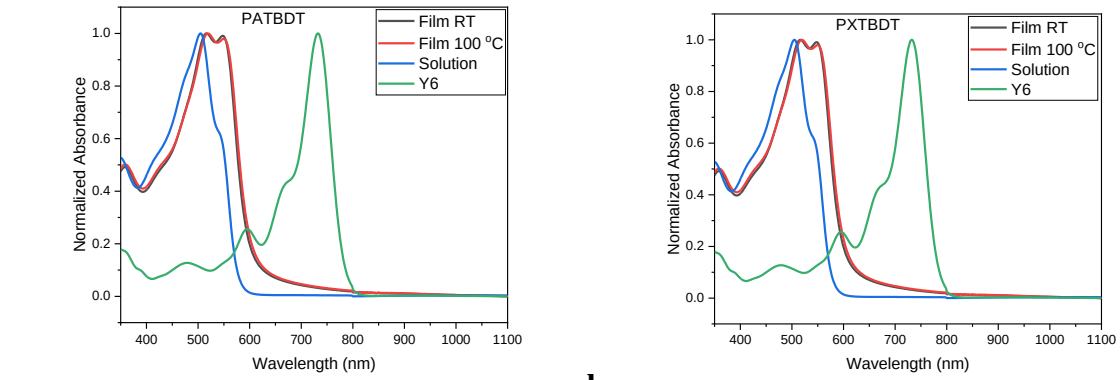

a **b**

Figure 5-58: UV-vis absorption spectra of as-cast thin film, annealed thin film, and chloroform solution for polymers: a) PATBDT, and b) PXTBDT.

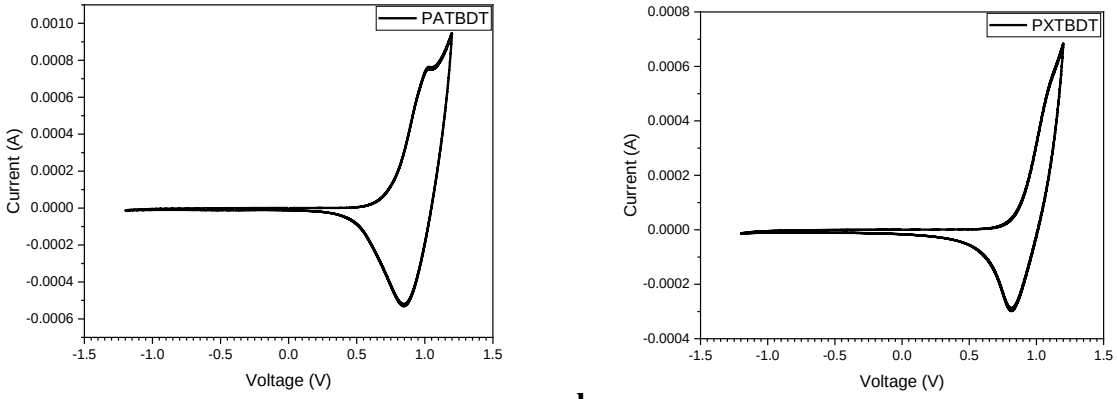

a **b**

Figure 5-59: CV profiles of polymers: a) PATBDT, and b) PXTBDT.

Table 5-30: Optical and electrochemical properties of polymers PATBDT, and PXTBDT.

Polymer	$\lambda_{max,s}$ (nm)	$\lambda_{max,fRT}$ (nm)	$\lambda_{max,f100C}$ (nm)	λ_{onset} (nm)	E_g^{opt} (eV)	E_{HOMO} (eV)	E_{LUMO} (eV)
PATBDT	505	517	519	602	2.06	-5.55	-3.49
PXTBDT	532	550	553	640	1.94	-5.67	-3.73

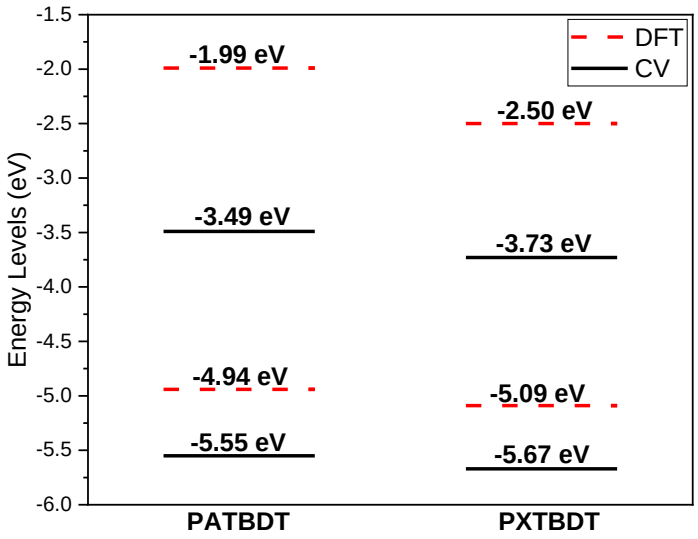

Figure 5-60: Comparison of DFT predicted HOMO and LUMO energy levels with CV obtained HOMO and LUMO levels for polymers PATBDT, and PXTBDT.

PL was acquired using the same method described in Section 2.4 (see **Figure 5-61**). Due to the favourable characteristics and strong performance of Y6 for OSC applications, Y6 was used as the commercial small molecule NFA for pairing with the polymer donors outlined in this chapter. PATBDT showed excellent quenching with Y6, with 99.4 and 99.85 % in the donor and acceptor regions, respectively, making it a good candidate for OSC applications. PXTBDT had 98.6 % quenching in the donor region and 89 % in the acceptor region. The exceptionally low E_{HOMO} might have contributed to the worse exciton dissociation performance when compared to PATBDT; however, the quenching is still promising for OSC applications.

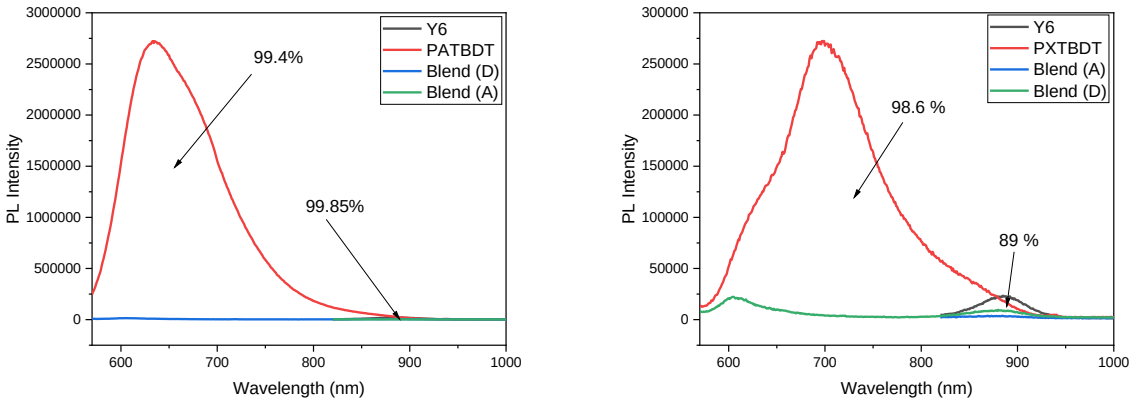

Figure 5-61: Photoluminescence spectra of PATBDT with Y6, and PXTBDT with Y6.

5.5 OPV Performance and Charge Mobility

A detailed device fabrication procedure can be found in Section 2.8.2.

Important note: *The polymers in this chapter were tested with a new device structure and testing system. In the past devices have achieved a FF of 0.56 by Yuan et al. and as high as 0.71 by Jiang et al. in our lab.*[52,53] *Furthermore, a shunt resistance of 883 ohm•cm*^{2} *and a series resistance of 2.84 ohm•cm*^{2} *have been reported by our group.*[53] *However, after switching to the new system, the FF is lower than previously achieved, which is related to issues with low shunt resistance and high series resistance. This indicates there is a problem with one or more of the layers and/or interfaces between layers, which is still being investigated by our group. Therefore, the data presented below might not represent the best data possible for these polymers.*

Summaries of the performance of each polymer can be found in **Table 5-31** to **Table 5-34**, and a comparison of the best J-V curves for each polymer is shown in **Figure 5-62**. PATBDT achieved a best PCE of 8.20 % (J_{sc} = 24.00 mA/cm^2, V_{oc} = 0.77 V, and FF = 0.46) when annealed at 100 ^{o}C. The main reasons for the better performance compared with the other polymers presented in this thesis are significantly better J_{sc} and FF. If the FF could be improved to previous levels (~0.56), a PCE around 10 % could be possible (if the other metrics remain the same). From DFT, this polymer was predicted to have a dihedral angle of 32.5 degrees due to the relative bulkiness of the acetal sidechain, with the methoxy groups repelling each other and bending in different directions. This could have a negative affect on charge transfer and morphology, which might explain why the V_{oc} is lower than high performing polymers with similar E_{HOMO} levels.[85] In comparison to other polymers in this thesis, the shunt resistance has noticeably increased for PATBDT, and the series resistance has noticeably decreased, although they are still not at the previously reported levels. This explains why the FF has improved for these devices.

PXTBDT achieved the best performance of the polymers reported within this thesis, with a best PCE of 9.97 % (J_{sc} = 24.20 mA/cm^2, V_{oc} = 0.84 V, and FF = 0.49) without annealing. Compared with PATBDT, the V_{oc} and FF have noticeably improved. The E_{HOMO} level for PXTBDT is significantly lower than PATBDT, which will help increase the V_{oc}. Furthermore, removal of the acetal chains results in a rigid aldehyde side chain, which decreases the dihedral angle

significantly to 23 degrees. Reduction of the dihedral angle can allow for better charge transport along the backbone of the polymer, and potentially better morphology, allowing for improved FF as compared to PATBDT. If the FF could be increased to 0.56, a PCE of approximately 11.5 % could be achieved, which is decent performance for OSCs. The improvement of FF from PATBDT to PXTBDT can be seen in **Figure 5-62**, where PXTBDT appears significantly more "square-shaped" resulting in better series and shunt resistances, as well as V_{oc}.

EQE of the polymers was also measured. PATBDT had a maximum EQE of 72 % and maintained greater than 50 % EQE in the range of 430 to 600 nm and 700 to 860 nm. Similarly, PXTBDT had a maximum EQE of 72 % and maintained greater than 50 % EQE in the range of 440 to 860 nm. However, PATBDT and PXTBDT had large errors of 26.18 and 26.92 %, respectively when comparing the J_{sc} obtained from OPV and EQE. This error is unacceptable, and like Chapters 2 and 3, it suggests that OPV is overestimating J_{sc} and/or EQE is underestimating J_{sc}. Optimization of the solar cell fabrication and testing with the new devices and testing station is required to determine the cause of the error and potential solutions to this problem.

Table 5-31: Summary of OSC device parameters for PATBDT:Y6.

Device	Annealing Temperature (°C)	RPM	Thickness (nm)
1	No annealing	1000	98.80 (±0.40)
2	No annealing	1500	89.95 (±0.05)
3	No annealing	2000	74.65 (±0.85)
4	50	1000	99.45 (±0.35)
5	50	1500	86.70 (±0.40)
6	50	2000	80.65 (±0.15)
7	100	1000	100.20 (±0.30)
8	100	1500	83.90 (±0.20)
9	100	2000	75.00 (±0.30)
10	150	1000	99.10 (±0.50)
11	150	1500	85.90 (±0.20)
12	150	2000	76.90 (±0.40)

Table 5-32: Summary of OSC performance for PATBDT:Y6.

Device	Jsc (mA/cm^2)	Voc (V)	FF	PCE (%)	Avg. Rsh ($ohm•cm^2$)	Avg. Rs ($ohm•cm^2$)
1	23.18 (22.78±0.37)	0.76 (0.76±0.01)	0.39 (0.39±0)	6.90 (6.69±0.14)	153 (±5)	11.84 (±0.61)
2	23.12 (22.61±0.48)	0.77 (0.76±0.01)	0.43 (0.41±0.01)	7.75 (7.08±0.37)	186 (±14)	10.41 (±0.82)
3	22.86 (22.02±0.75)	0.77 (0.77±0.01)	0.46 (0.45±0.01)	8.16 (7.67±0.42)	229 (±26)	8.17 (±0.52)
4	23.60 (22.32±1.00)	0.76 (0.75±0.01)	0.40 (0.39±0.01)	7.05 (6.49±0.42)	167 (±10)	11.51 (±0.47)
5	22.97 (22.62±0.32)	0.76 (0.75±0.01)	0.43 (0.43±0)	7.55 (7.21±0.23)	211 (±6)	9.63 (±0.50)
6	23.10 (21.96±0.87)	0.75 (0.75±0.01)	0.44 (0.44±0.01)	7.67 (7.19±0.41)	227 (±18)	8.84 (±0.46)
7	23.43 (23.19±0.52)	0.78 (0.76±0.01)	0.43 (0.41±0.01)	7.76 (7.26±0.29)	183 (±14)	9.88 (±0.34)
8	24.00 (24.20±0.20)	0.77 (0.77±0.01)	0.45 (0.44±0.01)	8.20 (8.15±0.05)	213 (±7)	8.19 (±0.03)
9	22.82 (21.88±0.76)	0.77 (0.76±0.01)	0.46 (0.45±0.01)	8.02 (7.46±0.44)	228 (±43)	8.83 (±0.40)
10	24.86 (23.73±0.68)	0.77 (0.76±0.01)	0.41 (0.40±0)	7.76 (7.24±0.36)	174 (±9)	9.94 (±0.37)
11	23.99 (22.84±0.74)	0.73 (0.73±0)	0.42 (0.42±0)	7.36 (7.00±0.25)	202 (±8)	9.51 (±0.62)
12	22.87 (21.87±0.68)	0.74 (0.73±0.01)	0.45 (0.43±0.01)	7.51 (6.87±0.53)	225 (±20)	9.21 (±0.57)

Table 5-33: Summary of OSC device parameters for PXTBDT:Y6.

Device	Annealing Temperature (^oC)	RPM	Thickness (nm)
1	No annealing	1000	111.75 (±2.05)
2	No annealing	1500	83.90 (±1.70)
3	No annealing	2000	67.40 (±1.00)
4	50	1000	95.05 (±0.95)
5	50	1500	80.85 (±1.65)
6	50	2000	67.25 (±0.35)
7	100	1000	92.20 (±1.10)
8	100	1500	78.90 (±1.60)
9	100	2000	69.50 (±1.90)
10	150	1000	90.90 (±0.70)
11	150	1500	80.75 (±2.55)
12	150	2000	70.80 (±0.80)

Table 5-34: Summary of OSC performance for PXTBDT:Y6.

Device	Jsc (mA/cm^2)	Voc (V)	FF	PCE (%)	Avg. Rsh ($ohm•cm^2$)	Avg. Rs ($ohm•cm^2$)
1	22.81 (21.05±1.57)	0.81 (0.81±0.01)	0.39 (0.38±0.01)	7.20 (6.46±0.47)	181 (±47)	11.80 (±3.21)
2	25.54 (23.95±1.16)	0.82 (0.80±0.01)	0.44 (0.42±0.01)	9.21 (8.12±0.64)	213 (±24)	7.32 (±0.49)
3	24.20 (23.84±0.78)	0.84 (0.81±0.01)	0.49 (0.47±0.01)	9.97 (9.19±0.56)	285 (±28)	6.47 (±0.14)
4	25.20 (24.42±1.11)	0.80 (0.79±0.01)	0.41 (0.40±0.01)	8.34 (7.71±0.55)	166 (±17)	5.66 (±2.33)
5	24.75 (23.94±0.93)	0.82 (0.80±0.01)	0.47 (0.45±0.01)	9.49 (8.65±0.62)	235 (±79)	6.48 (±0.26)
6	24.98 (23.39±1.11)	0.82 (0.80±0.01)	0.47 (0.45±0.02)	9.59 (8.38±0.66)	237 (±31)	7.19 (±1.49)
7	24.68 (23.51±1.15)	0.81 (0.79±0.01)	0.41 (0.40±0.01)	8.19 (7.47±0.59)	178 (±23)	7.73 (±0.52)
8	24.76 (23.97±1.26)	0.82 (0.80±0.02)	0.48 (0.45±0.02)	9.63 (8.61±0.84)	238 (±34)	6.34 (±0.22)
9	23.25 (22.91±1.00)	0.82 (0.80±0.02)	0.47 (0.45±0.02)	9.08 (8.22±0.76)	248 (±52)	7.01 (±0.60)
10	24.34 (23.66±0.65)	0.80 (0.79±0.01)	0.41 (0.39±0.01)	8.06 (7.21±0.56)	166 (±39)	7.07 (±1.66)
11	24.31 (23.49±0.74)	0.81 (0.78±0.01)	0.43 (0.40±0.01)	8.35 (7.31±0.54)	176 (±28)	7.98 (±0.75)
12	23.26 (22.99±1.00)	0.82 (0.80±0.02)	0.51 (0.48±0.02)	9.68 (8.83±0.75)	302 (±84)	6.12 (±0.23)

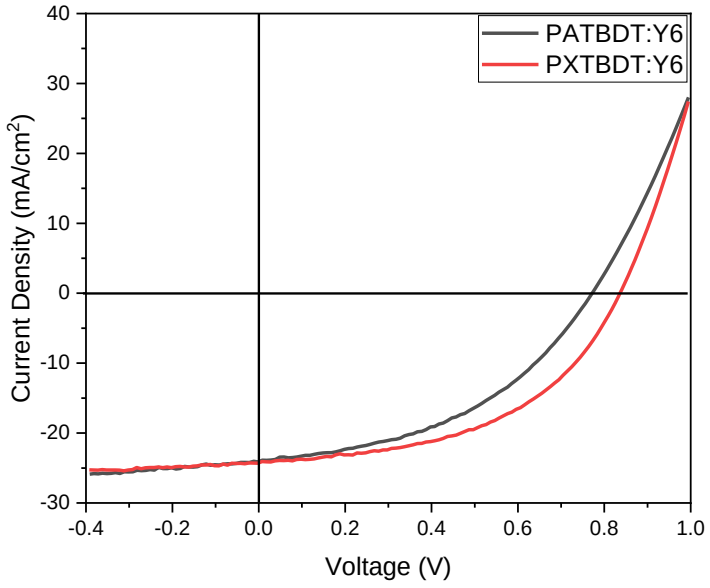

Figure 5-62: J-V curves for PATBDT:Y6 (100 °C), and PXTBDT:Y6 (RT).

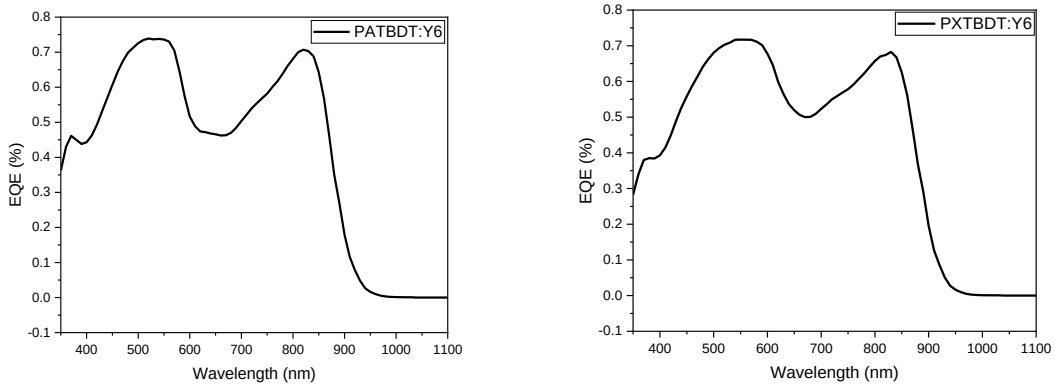

Figure 5-63: EQE of best performing OSCS based on PATBDT:Y6, and PXTBDT:Y6.

Table 5-35: Comparison of Jsc values obtained from OPV and EQE measurements for PATBDT, and PXTBDT.

Polymer	Jsc from OPV (mA/cm^2)	Jsc from EQE (mA/cm^2)	Error (%)
PATBDT	24.39	19.33	26.18
PXTBDT	24.99	19.69	26.92

Devices for SCLC mobility were prepared and tested as described in Section 2.5. PATBDT and PXTBDT had good hole mobilities as neat films with values of $1.63x10^{-4}$ and $1.43x10^{-4}$ $cm^2V^{-1}s^{-1}$, respectively. PATBDT had even better hole mobility when mixed with Y6 ($2.82x10^{-4}$ $cm^2V^{-1}s^{-1}$); however, the electron mobility was low ($2.50x10^{-5}$ $cm^2V^{-1}s^{-1}$), resulting in an unbalanced ratio of 0.0887. The electron mobility is too low and could be the cause of the lower FF. Potentially a different acceptor or different donor:acceptor ratio is necessary to get balanced charge mobility and improve the performance. For PXTBDT, a decrease in hole mobility is observed when blended with Y6 ($4.64x10^{-5}$ $cm^2V^{-1}s^{-1}$); however, the electron mobility is still lower than the hole mobility, resulting in a ratio of 0.319. The moderately unbalanced and low mobility is limiting the performance of this material; however, the better mobility ratio for PXTBDT might contribute to its better performance than PATBDT. To achieve higher performance, a different donor:acceptor ratio or a different NFA material should be tested with PATBDT and PXTBDT to improve the electron SCLC mobility.

Table 5-36: SCLC hole and electron mobilities for neat polymers and D:A blend films of PATBDT, and PXTBDT with Y6.

Polymer	μ_e (x10^{-4} $cm^2V^{-1}s^{-1}$)	μ_h (x10^{-4} $cm^2V^{-1}s^{-1}$)	μ_e/μ_h
PATBDT	N/A	1.63 (1.52)	N/A
PATBDT:Y6	0.250 (0.199)	2.82 (1.02)	0.0887 (0.195)
PXTBDT	N/A	1.43 (1.28)	N/A
PXTBDT:Y6	0.148 (0.134)	0.464 (0.359)	0.319 (0.373)

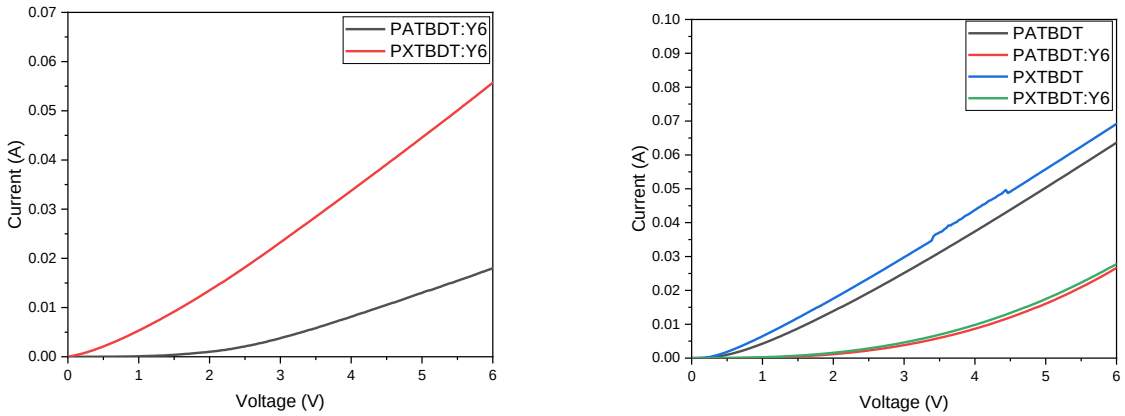

Figure 5-64: Left: electron mobility I-V curves for PATBDT:Y6, and PXTBDT:Y6; Right: hole mobility I-V curves of neat PATBDT, PATBDT:Y6, neat PXTBDT, and PXTBDT:Y6.

5.6 Crystallinity

Figure 5-65 does not contain any significant peaks for PATBDT as a neat film and as a blend with Y6, both for the in-plane and out-of-plane measurements. This indicates the polymer is quite amorphous. Similarly, no significant peaks are observed for PXTBDT in **Figure 5-66**, which indicates it also adopts a disordered packing structure.

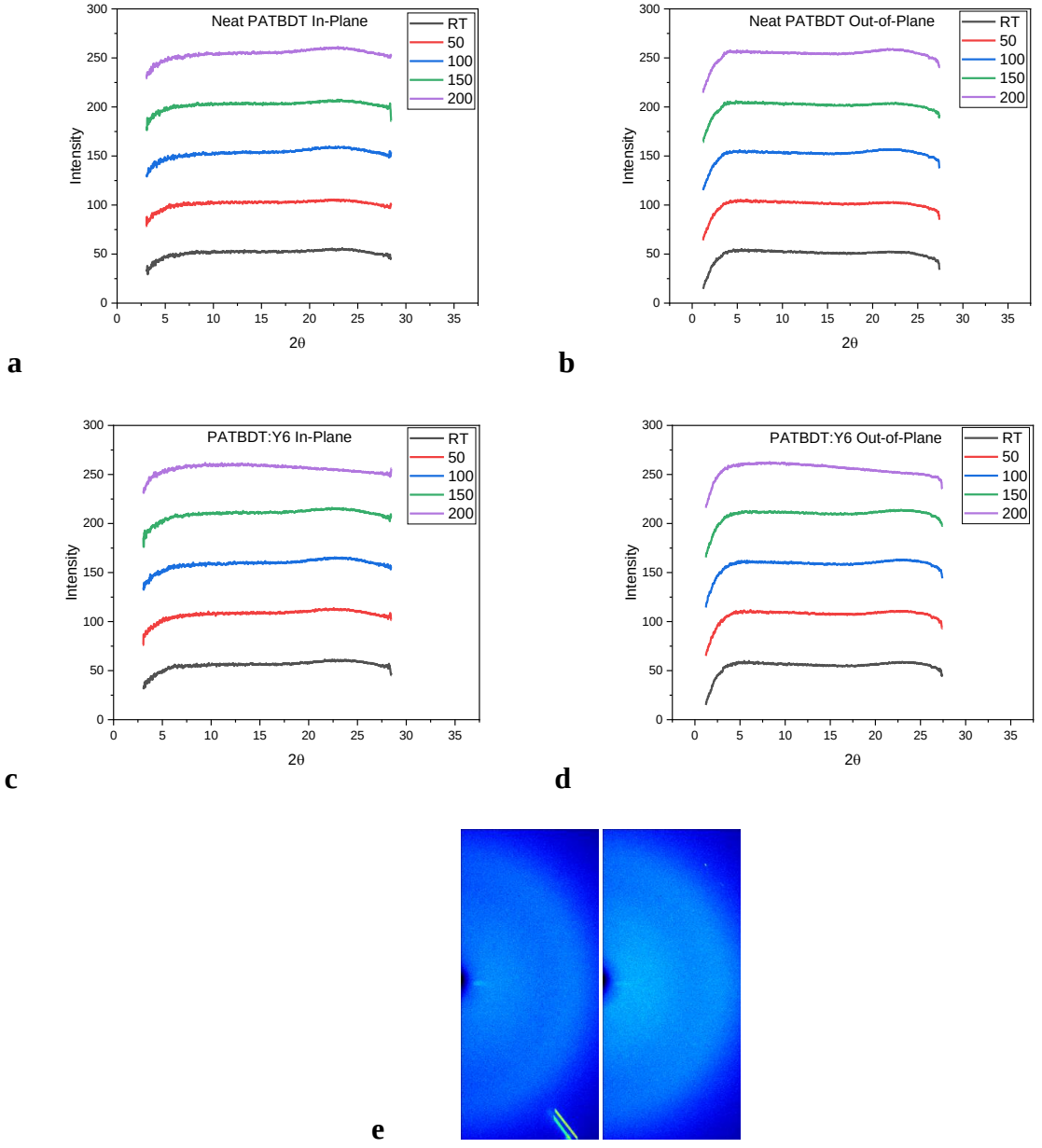

Figure 5-65: GIXD patterns of films at different annealing temperatures: a) in-plane neat PATBDT; b) out-of-plane neat PATBDT; c) in-plane PATBDT:Y6 blend; d) out-of-plane PATBDT:Y6 blend; e) 2D images of the best performing material (annealed at 100 ºC), where the left is neat PATBDT and the right is PATBDT:Y6.

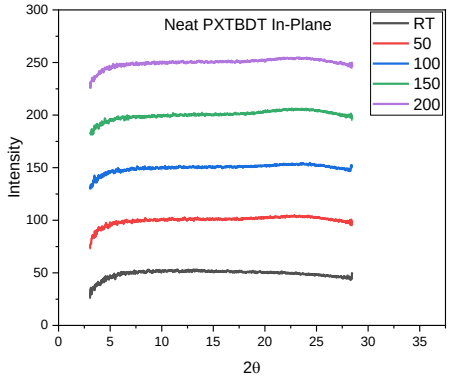

a

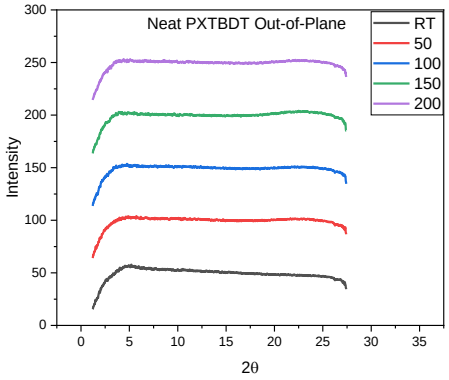

b

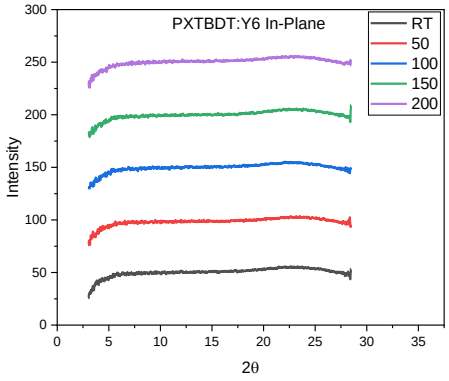

c

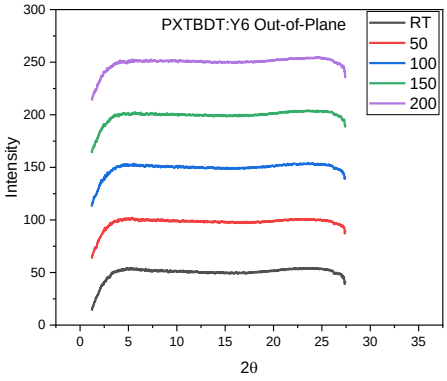

d

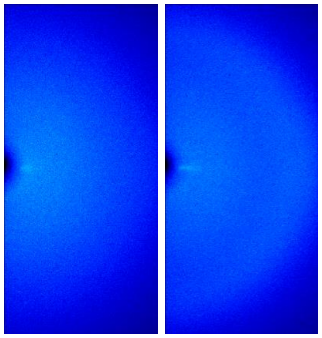

e

Figure 5-66: GIXD patterns of films at different annealing temperatures: a) in-plane neat PXTBDT; b) out-of-plane neat PXTBDT; c) in-plane PXTBDT:Y6 blend; d) out-of-plane PXTBDT:Y6 blend; e) 2D images of the best performing material (no annealing), where the left is neat PXTBDT and the right is PXTBDT:Y6.

5.7 Summary and Future Direction

In summary, two novel D-A polymers were synthesized, with PATBDT and PXTBDT consisting of a thiophene-BDT backbone. PATBDT was designed due to its low-cost, easy synthesis, and ability to modify the structure after polymerization using an acid to form PXTBDT. DFT calculations predicted these polymers to have low E_{HOMO} levels, while PATBDT was predicted to have a slightly high dihedral angle which could negatively affect the performance. ^{1}H NMR was used to show the acetal group was successfully converted to an aldehyde upon the addition of HCl, forming PXTBDT. These polymers were thermally stable, displaying wide bandgaps, and low E_{HOMO} levels. The E_{HOMO} of PXTBDT was especially low (-5.67 eV) indicating the aldehyde was a very strong EWG. PATBDT and PXTBDT showed good PL quenching when mixed with Y6. In terms of OPV performance, PATBDT achieved a decent PCE of 8.20 % (J_{sc} = 24.00 mA/cm^2, V_{oc} = 0.77 V, and FF = 0.46) when annealed at 100 ^{o}C, while PXTBDT achieved a better PCE of 9.97 % (J_{sc} = 24.20 mA/cm^2, V_{oc} = 0.84 V, and FF = 0.49) without annealing. The increase in V_{oc} and FF for PXTBDT compared to PATBDT are likely due to the lower E_{HOMO} and probable reduction in backbone twisting. PATBDT had a high hole mobility, but a magnitude lower electron mobility resulted in unbalanced charge transfer. PXTBDT had low electron and hole mobility (10^{-5}) and moderately unbalanced transfer due to three times lower electron mobility than hole mobility. Both PATBDT and PXTBDT formed amorphous films with Y6. PATBDT and PXTBDT are promising materials with room to improve the FF by optimizing the OPV fabrication and testing processes.

For future work, similar to Chapters 2 through 4, the surface roughness of the active layers can be examined using AFM to determine if there are any issues with the film. This can also provide the domain sizes to assess if there are issues with aggregation that may be limiting the performance. The device stability could also be tested to determine if the performance is stable, which could provide insight into potential polymer structures that can enhance stability in OSCs. Solvent additives and/or a different acceptor could be used to try to control the crystallinity for better OPV performance. The donor:acceptor ratio can be optimized to try to improve and balance the SCLC mobility ratios by increasing the portion of Y6 added in the active layer blend, which could lead to better PCE for PATBDT and PXTBDT. Furthermore, optimization of the solar cell fabrication and/or testing is required to improve the FF of these materials, which will

result in more accurate and better performance of these materials. For PATBDT, halogens could be introduced to the BDT portion to lower the E_{HOMO}, which could increase the V_{oc}. Different post polymerization modifications could be examined; for example, exchanging of the aldehyde oxygen to a sulfur atom in the thiophene side chain. Finally, different D units such as bithiophene or thienothiophene could be implemented into the polymer backbone to try to find other polymers which can take advantage of the good performance and simple chemistry of the acetal/aldehyde-substituted thiophene A unit.

5.8 Experimental Section

5.8.1 Materials Characterization

The chemicals and solvents used for synthesis were purchased from commercial vendors including Fluka, Armstrong, Sigma-Aldrich, TCI, and VWR without further purification. The reactions used anhydrous solvents which were obtained from Sigma-Aldrich. 1,1'-[4,8-bis[5-(2-ethylhexyl)-2-thienyl]benzo[1,2-b:4,5-b']dithiophene-2,6-diyl]bis[1,1,1-trimethylstannane] (BDT) and Y6 were purchased from 1-Material. Specific synthesis details will be shown in Section 5.8.3 below. The characterization and testing of polymers were done using the same equipment as specified in Section 2.8.1.

5.8.2 OSC Device Fabrication and Characterization

The OSC fabrication and characterization was completed according to the information provided in Section 2.8.2.

5.8.3 Synthesis Routes

Synthesis of 2,5-dibromo-3-(dimethoxymethyl)thiophene

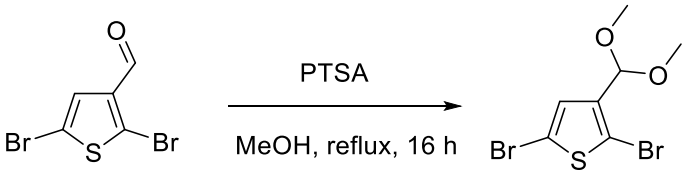

To a 25 mL two-neck round bottom flask, PTSA (3.27 mg, 0.019 mmol) and 2,5-dibromo-3-acetal thiophene (170.95 mg, 0.63 mmol) were added along with a magnetic stir bar. The reaction system was purged of oxygen. Anhydrous methanol (10 mL) was added, and the reaction mixture was refluxed overnight. After 16 hours, the reaction mixture was poured into diethyl ether and washed with saturated sodium bicarbonate solution 3 times (50 mL each). Then it was dried using sodium sulfate. After evaporation of the solvent, the crude product was obtained as a yellow oil. (Yield: 168.1 mg, 84 %). ^{1}H NMR (300 MHz, $CDCl_3$, δ/ppm): 7.02 (s, 1H), 5.28 (s, 1H), 3.33 (s, 6H).[86]

Synthesis of polymer PATBDT

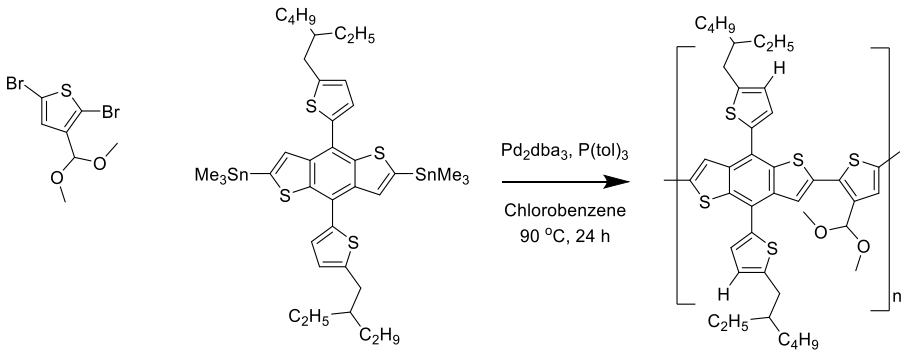

2,5-dibromo-3-(dimethoxymethyl)thiophene (81.1 mg, 0.256 mmol, 1.0 equiv.) was added to the system with 1,1'-[4,8-bis[5-(2-ethylhexyl)-2-thienyl]benzo[1,2-b:4,5-b']dithiophene-2,6-diyl]bis[1,1,1-trimethylstannane] (BDT-derivative) (231.6 mg, 0.256 mmol, 1.0 equiv.), and tri(o-tolyl)phosphine ($(P(tol)_3$) (6.2 mg, 0.02 mmol, 0.08 equiv.) into a 25 mL two-neck round bottom flask along with a stir bar. The system was purged with argon for three 10-minute cycles. A solution of tris(dibenzylideneacetone)dipalladium(0) catalyst (Pd_2dba_3) (9.15 mg, 0.01 mmol, 0.04 equiv.) in 1 mL chlorobenzene was obtained using a glove bag under nitrogen, by measuring out the solid catalyst, before adding 1 mL of solvent. This catalyst solution was added with a syringe. 4 additional mL of chlorobenzene were added as solvent. The reaction mixture was then heated at 90 ^oC under argon atmosphere for 24 hours. After cooling down to room temperature, the mixture was poured into a stirring methanol (150 mL) with several drops of triethylamine. The solid was collected by filtration, dried, and further purified through Soxhlet extraction using acetone, hexane, chloroform, and chlorobenzene. (Yield: 179.7 mg, 95.6 % in chloroform).

Synthesis of polymer PXTBDT

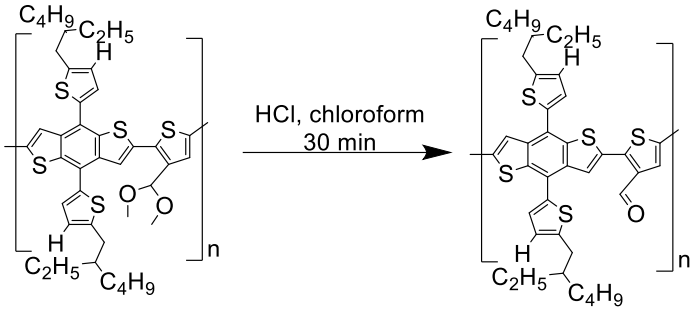

The polymer PATBDT was dissolved in chloroform (20 mg in 4 mL) and a stir bar was added. 1-2 drops of HCl were added to the solution and the solution was stirred for 30 minutes. The solution changed colours from bright red to dark purple. The solution was then worked up using water and extracted with chloroform. The chloroform was evaporated using the rotary evaporator. The polymer was stirred in 150 mL methanol with 1 mL of pyridine to neutralize the polymer for 30 minutes. The polymer was acquired by vacuum filtration, rinsed with methanol, and was dried under high vacuum. (Yield: ~100 %).

Chapter 6: Summary and Future Direction

The work in this thesis aimed to design, synthesize, and test eight novel donor polymers for OSC applications. After exploring the design ideas with DFT calculations, the opto-electrochemical properties were measured. Based on this information, an acceptable commercial small molecule NFA was selected for OPV testing in BHJ inverted solar cells. The polymers were assessed for OSC performance, SCLC mobility, and crystallinity to determine the positive attributes as well as the drawbacks of the materials contained in this thesis. The work described in this thesis targeted low-cost polymer donor materials through relatively easy synthesis routes and low-cost starting materials. Side chains were selected to target good solubility, low E_{HOMO} levels (to match with high performance NFAs like Y6), and good morphology to achieve high performing polymer donor materials. Although the ethynyl, triazole, and tetrafluorobenzene polymers were synthesized with low-cost materials, low E_{HOMO} levels, and good solubility in chloroform (excluding PBETBDT), the performance was quite low. However, PATBDT and PXTBDT achieved decent performance (PCE of 8.20 % (J_{sc} = 24.00 mA/cm^2, V_{oc} = 0.77 V, and FF = 0.46) and PCE of 9.97 % (J_{sc} = 24.20 mA/cm^2, V_{oc} = 0.84 V, and FF = 0.49), respectively), while using simple synthesis routes that require low-cost materials (e.g., methanol used as both a solvent and a reagent, HCl, NBS, etc.). This performance is expected to increase when the solar cell fabrication and testing is optimized in our lab due to improvements to the FF.

Chapter 2 focused on an ethynyl series of wide bandgap D-A polymers based on a BDT-thiophene repeat unit. The goal of this series was to extend the conjugation into the side chain perpendicular to the backbone. This provides advantages including effective polarization of the polymer, which can increase the dielectric constant, resulting in reduced exciton binding energy, and allowing for longer exciton lifetimes. This series implemented triple bonds to attach the side chain, incorporating a trimethyl silyl group (PSETBDT), a benzene ring (PBETBDT), and an alkyloxime attached to a benzene ring at the para position (POBETBDT). PSETBDT was difficult to polymerize, and the polymer had a high PDI, indicating cross-linking occurred. This polymer performed quite poorly with Y6 (1.44 %) and even worse with IT-4F (0.77 %). Cross-linking, and lamellar packing with IT-4F contributed to unbalanced mobilities, which resulted in poor performance. The polymerization of PBETBDT had a poor yield due to the side chain providing insufficient solubility in common processing solvents (chloroform and chlorobenzene),

which resulted in a low molecular weight. Therefore, preliminary electrochemical data was acquired but further testing, including OPV, was not. POBETBDT incorporated an alkyloxime side chain, which has been shown to help provide good performance by our group in the past; however, POBETBDT only achieved a best PCE of 3.65 % due to low V_{oc} and FF. This polymer had low SCLC mobility and the bulkiness and distance of the alkyloxime side chain to the backbone were suspected to negatively impact the charge transfer characteristics. Potential future work includes examining the surface roughness and domain sizes via AFM to identify issues that contributed to the low performance of this series. Additionally, exploring other applications for the ethynyl polymers such as metal complex detection is possible since there is a current market for chemical sensors in this area.

Chapter 3 examined a different method of extending the conjugation into the side chain by using triazole rings. This series reacted an azide with a carbonyl group to form a triazole ring, where an alkyl chain (PTTBDT) and a carbamate chain (PCTBDT) were added at the middle nitrogen atom in the ring. PTTBDT achieved a PCE of 5.00 %; however, low mobility and FF were limiting the performance of this material. As indicated by DFT, side chain and/or backbone twisting are suspected to negatively impact the performance of this polymer. PCTBDT achieved a worse PCE of 3.29 % due to worse J_{sc}, V_{oc}, and FF, while having exceptionally low hole mobility and unbalanced charge mobility. Twisting and the thermally removable carbamate side chain, which when removed potentially results in hole trapping, were suspected as the main reasons for low performance of this material. Potential future work includes increasing the D:A ratio in the active layer to improve mobility and performance, which is especially relevant for PTTBDT since it had the most promising performance. Furthermore, an investigation into hole trapping issues associated with the thermally removable carbamate chain can be done using OTFT mobility. Finally, the active layer must be optimized to improve the FF for these materials.

Chapter 4 studied a wide bandgap D-A polymer, where improved molecular design and ease of synthesis were the goals. A polymer with a benzene-BDT repeating unit, PFBBDT, was designed to adapt a previously reported perovskite hole transfer material (unsubstituted benzene-BDT) for OSC active layer applications. From DFT, the addition of fluorine atoms lowered the E_{HOMO} and increased the co-planarity, which was promising for good OPV performance. This material

achieved a PCE of 5.14 % due to low V_{oc} and FF. PFBBDT had strong lamellar packing interactions, likely caused by hydrogen bonding in the backbone making this polymer very co-planar and its low molecular weight. This resulted in low mobility, potentially due to morphology issues with domain sizes. Furthermore, PFBBDT had an exceptionally low molecular weight, which has been shown to negatively impact J_{sc}, FF, and V_{oc}. Therefore, future work includes optimizing the Still Coupling polymerization conditions to increase the molecular weight of this polymer. Additionally, AFM measurements on the thin film from the PFBBDT:Y6 blend can be performed to investigate aggregation associated with the strong lamellar stacking. PFBBDT should be tested as a transistor since the strong lamellar packing means that horizontal charge transfer should be high, making this a promising material for this application. Finally, a spacer molecule, such as thiophene, with a solubilizing side chain could be added to try to improve the molecular weight.

Chapter 5 described two wide bandgap D-A polymers, where improved molecular design, ease of synthesis, and opportunity for a post polymerization modification were the goals. Polymer PATBDT was designed with an acetal side chain on the thiophene unit of a thiophene-BDT based polymer with the intention of examining an acid-catalyzed post polymerization modification to yield a formaldehyde-substituted polymer. PATBDT showed a low lying E_{HOMO} and wide bandgap, which also made it a candidate for OSC applications. When paired with Y6, a PCE of 8.20 % was achieved. Low electron mobility resulted in unbalanced charge transfer and low FF. In a post polymerization modification, the acetal side chain was converted back to an aldehyde using HCl. Previously, synthesis of a polymer based on BDT and this formaldehyde substituted thiophene was attempted by our group but was unsuccessful due to solubility issues. This post polymerization modification method successfully resulted in a soluble polymer, PXTBDT, which had a quite low E_{HOMO} of -5.67 eV. This polymer worked well with Y6, achieving a decent PCE of 9.97 %, which was mainly hindered by low FF. Future optimization of our solar cell system could result in an increase in FF, and subsequently PCE. In terms of future work, polymers PATBDT and PXTBDT could be mixed with a different D:A ratio to try to improve the SCLC mobility balance by increasing the Y6 portion since the electron mobilities were less than the hole mobilities. The device stability could also be tested to determine if the performance is stable, which could provide insight into potential polymer structures that can enhance stability in OSCs. For PATBDT, halogens could be introduced to the BDT portion to

lower the E_{HOMO}, which could increase the V_{oc}. Solvent additives such as 1,8-diiodooctane and/or a different acceptor could be used to try to control the crystallinity for face-on orientation to achieve better OPV performance. Other post polymerization modifications could be explored to see the effects on the performance including conversion of the aldehyde to a sulfonyl functional group. Finally, incorporation of different D units instead of BDT, such as bithiophene and thienothiophene, could be explored to discover new polymers that can take advantage of the simple chemistry and promising performance of the acetal and aldehyde-substituted thiophene A units.

References

(1) He, K.; Kumar, P.; Yuan, Y.; Li, Y. Wide Bandgap Polymer Donors for High Efficiency Non-Fullerene Acceptor Based Organic Solar Cells. *Mater. Adv.* **2021**, *2* (1), 115–145. https://doi.org/10.1039/D0MA00790K.

(2) O'Neil, C.; Dreves, H. *Building a Solar-Powered Future*. NREL Transforming Energy. https://www.nrel.gov/news/program/2022/building-a-solar-powered-future.html (accessed 2023-01-05).

(3) Riede, M.; Spoltore, D.; Leo, K. Organic Solar Cells—The Path to Commercial Success. *Adv. Energy Mater.* **2021**, *11* (1), 2002653. https://doi.org/10.1002/aenm.202002653.

(4) Lozanova, S. *California Solar Mandate*. GreenLancer. https://www.greenlancer.com/post/california-solar-mandate (accessed 2023-01-05).

(5) Wu, J.; Gao, M.; Chai, Y.; Liu, P.; Zhang, B.; Liu, J.; Ye, L. Towards a Bright Future: The Versatile Applications of Organic Solar Cells. *Mater. Rep. Energy* **2021**, *1* (4), 100062. https://doi.org/10.1016/j.matre.2021.100062.

(6) Sharma, A.; Masoumi, S.; Gedefaw, D.; O'Shaughnessy, S.; Baran, D.; Pakdel, A. Flexible Solar and Thermal Energy Conversion Devices: Organic Photovoltaics (OPVs), Organic Thermoelectric Generators (OTEGs) and Hybrid PV-TEG Systems. *Appl. Mater. Today* **2022**, *29*, 101614. https://doi.org/10.1016/j.apmt.2022.101614.

(7) Huang, F.; Hin-Lap, Y.; Cao, Y. *Polymer Photovoltaics - Materials, Physics, and Device Engineering - Knovel*; RSC Polymer Chemistry; Royal Society of Chemistry, 2016.

(8) Tong, Y.; Xiao, Z.; Du, X.; Zuo, C.; Li, Y.; Lv, M.; Yuan, Y.; Yi, C.; Hao, F.; Hua, Y.; Lei, T.; Lin, Q.; Sun, K.; Zhao, D.; Duan, C.; Shao, X.; Li, W.; Yip, H.-L.; Xiao, Z.; Zhang, B.; Bian, Q.; Cheng, Y.; Liu, S.; Cheng, M.; Jin, Z.; Yang, S.; Ding, L. Progress of the Key Materials for Organic Solar Cells. *Sci. China Chem.* **2020**, *63* (6), 758–765. https://doi.org/10.1007/s11426-020-9726-0.

(9) Waldauf, C.; Denk, P.; Morana, M.; Brabec, C. J.; Coakley, K.; Schilinsky, P.; Choulis, S. A. Alternative Device Concepts for Future Requirements of Organic Photovoltaic Cells; Kafafi, Z. H., Lane, P. A., Eds.; San Diego, California, USA, 2006; p 63340A. https://doi.org/10.1117/12.682226.

(10) Öner, İ. V.; Yilmaz, E. Ç.; Yesilyurt, M. K.; Ömeroglu, G.; Özakin, A. N. Operational Stability and Degradation of Organic Solar Cells. *Period. Eng. Nat. Sci. PEN* **2017**, *5* (2). https://doi.org/10.21533/pen.v5i2.105.

(11) Pandikumar, A.; Ramaraj, R. *Rational Design of Solar Cells for Efficient Solar Energy Conversion*, 1st ed.; John Wiley and Sons, Inc., 2018.

(12) Ben Dkhil, S. *What is the "third generation" of photovoltaic ?* Dracula Technologies. https://dracula-technologies.com/what-is-the-third-generation-of-photovoltaic/ (accessed 2023-01-06).

(13) Honsberg, C.; Bowden, S. *Short-Circuit Current | PVEducation*. PVEducation. https://www.pveducation.org/pvcdrom/solar-cell-operation/short-circuit-current (accessed 2023-01-10).

(14) Rafique, S.; Abdullah, S. M.; Sulaiman, K.; Iwamoto, M. Fundamentals of Bulk Heterojunction Organic Solar Cells: An Overview of Stability/Degradation Issues and Strategies for Improvement. *Renew. Sustain. Energy Rev.* **2018**, *84*, 43–53. https://doi.org/10.1016/j.rser.2017.12.008.

(15) Bowden, S. Solar Cell Fill Factors: General Graph and Empirical Expressions. *Solid-State Electron.* **1981**, *24*, 788–789. https://doi.org/10.1016/0038-1101(81)90062-9.

(16) Qi, B.; Wang, J. Fill Factor in Organic Solar Cells. *Phys. Chem. Chem. Phys.* **2013**, *15* (23), 8972–8982. https://doi.org/10.1039/C3CP51383A.
(17) Armin, A.; Li, W.; Sandberg, O. J.; Xiao, Z.; Ding, L.; Nelson, J.; Neher, D.; Vandewal, K.; Shoaee, S.; Wang, T.; Ade, H.; Heumuller, T.; Brabec, C. J.; Meredith. A History and Perspective of Non-Fullerene Electron Acceptors for Organic Solar Cells. *Adv. Energy Mater.* **2021**, *11* (15). https://doi.org/10.1002/aenm.202003570.
(18) Xia, D.; Li, C.; Li, W. Crystalline Conjugated Polymers for Organic Solar Cells: From Donor, Acceptor to Single-Component. *Chem. Rec.* **2019**, *19* (6), 962–972. https://doi.org/10.1002/tcr.201800131.
(19) Zhang, G.; Zhao, J.; Chow, P. C. Y.; Jiang, K.; Zhang, J.; Zhu, Z.; Zhang, J.; Huang, F.; Yan, H. Nonfullerene Acceptor Molecules for Bulk Heterojunction Organic Solar Cells. *Chem. Rev.* **2018**, *118* (7), 3447–3507. https://doi.org/10.1021/acs.chemrev.7b00535.
(20) Genene, Z.; Mammo, W.; Wang, E.; Andersson, M. R. Recent Advances in N-Type Polymers for All-Polymer Solar Cells. *Adv. Mater.* **2019**, *31* (22), 1807275. https://doi.org/10.1002/adma.201807275.
(21) Yuan, J.; Zhang, Y.; Zhou, L.; Zhang, G.; Yip, H.-L.; Lau, T.-K.; Lu, X.; Zhu, C.; Peng, H.; Johnson, P. A.; Leclerc, M.; Cao, Y.; Ulanski, J.; Li, Y.; Zou, Y. Single-Junction Organic Solar Cell with over 15% Efficiency Using Fused-Ring Acceptor with Electron-Deficient Core. *Joule* **2019**, *3* (4), 1140–1151. https://doi.org/10.1016/j.joule.2019.01.004.
(22) Zhou, H.; Yang, L.; Stoneking, S.; You, W. A Weak Donor−Strong Acceptor Strategy to Design Ideal Polymers for Organic Solar Cells. *ACS Appl. Mater. Interfaces* **2010**, *2* (5), 1377–1383. https://doi.org/10.1021/am1000344.
(23) Dou, L.; Liu, Y.; Hong, Z.; Li, G.; Yang, Y. Low-Bandgap Near-IR Conjugated Polymers/Molecules for Organic Electronics. *Chem. Rev.* **2015**, *115* (23), 12633–12665. https://doi.org/10.1021/acs.chemrev.5b00165.
(24) Cui, C.; Wong, W.-Y. Effects of Alkylthio and Alkoxy Side Chains in Polymer Donor Materials for Organic Solar Cells. *Macromol. Rapid Commun.* **2016**, *37* (4), 287–302. https://doi.org/10.1002/marc.201500620.
(25) Sun, C.; Pan, F.; Bin, H.; Zhang, J.; Xue, L.; Qiu, B.; Wei, Z.; Zhang, Z.-G.; Li, Y. A Low Cost and High Performance Polymer Donor Material for Polymer Solar Cells. *Nat. Commun.* **2018**, *9* (1), 743. https://doi.org/10.1038/s41467-018-03207-x.
(26) Kularatne, R. S.; Magurudeniya, H. D.; Sista, P.; Biewer, M. C.; Stefan, M. C. Donor–Acceptor Semiconducting Polymers for Organic Solar Cells. *J. Polym. Sci. Part Polym. Chem.* **2013**, *51* (4), 743–768. https://doi.org/10.1002/pola.26425.
(27) Zhang, M.; Guo, X.; Ma, W.; Ade, H.; Hou, J. A Large-Bandgap Conjugated Polymer for Versatile Photovoltaic Applications with High Performance. *Adv. Mater.* **2015**, *27* (31), 4655–4660. https://doi.org/10.1002/adma.201502110.
(28) Dang, D.; Yu, D.; Wang, E. Conjugated Donor–Acceptor Terpolymers Toward High-Efficiency Polymer Solar Cells. *Adv. Mater.* **2019**, *31* (22), 1807019. https://doi.org/10.1002/adma.201807019.
(29) Ji, J.-M.; Zhou, H.; Kim, H. K. Rational Design Criteria for D–π–A Structured Organic and Porphyrin Sensitizers for Highly Efficient Dye-Sensitized Solar Cells. *J. Mater. Chem. A* **2018**, *6* (30), 14518–14545. https://doi.org/10.1039/C8TA02281J.
(30) Ahmed, E.; Ren, G.; Kim, F. S.; Hollenbeck, E. C.; Jenekhe, S. A. Design of New Electron Acceptor Materials for Organic Photovoltaics: Synthesis, Electron Transport, Photophysics,

and Photovoltaic Properties of Oligothiophene-Functionalized Naphthalene Diimides. *Chem. Mater.* **2011**, *23* (20), 4563–4577. https://doi.org/10.1021/cm2019668.
(31) Deibel, C.; Strobel, T.; Dyakonov, V. Role of the Charge Transfer State in Organic Donor–Acceptor Solar Cells. *Adv. Mater.* **2010**, *22* (37), 4097–4111. https://doi.org/10.1002/adma.201000376.
(32) Yao, H.; Chen, Y.; Qin, Y.; Yu, R.; Cui, Y.; Yang, B.; Li, S.; Zhang, K.; Hou, J. Design and Synthesis of a Low Bandgap Small Molecule Acceptor for Efficient Polymer Solar Cells. *Adv. Mater.* **2016**, *28* (37), 8283–8287. https://doi.org/10.1002/adma.201602642.
(33) Kim, G.-W.; Kim, J.; Lee, G.-Y.; Kang, G.; Lee, J.; Park, T. A Strategy to Design a Donor–π–Acceptor Polymeric Hole Conductor for an Efficient Perovskite Solar Cell. *Adv. Energy Mater.* **2015**, *5* (14), 1500471. https://doi.org/10.1002/aenm.201500471.
(34) Falck, D.; Niessen, W. M. A. Solution-Phase Electrochemistry-Nuclear Magnetic Resonance of Small Organic Molecules. *TrAC Trends Anal. Chem.* **2015**, *70*, 31–39. https://doi.org/10.1016/j.trac.2015.03.010.
(35) Naito, A.; Asakura, T.; Shimada, I.; Takegoshi, K.; Yamamoto, Y. *Experimental Approaches of NMR Spectroscopy*; Springer Nature Singapore Pte Ltd., 2018.
(36) Yang, R. *Analytical Methods for Polymer Characterization*; CRC Press: Boca Raton, 2018. https://doi.org/10.1201/9781351213158.
(37) *Polymer Characterisation*; Hunt, B. J., James, M. I., Eds.; Springer Netherlands: Dordrecht, 1993. https://doi.org/10.1007/978-94-011-2160-6.
(38) Gevorg, D. S. *NMR Chemical Shift Values Table*. Chemistry Steps. https://www.chemistrysteps.com/nmr-chemical-shift-values-table/ (accessed 2023-01-12).
(39) Fair, R. A.; Xie, R.; Lee, Y.; Colby, R. H.; Gomez, E. D. Molecular Weight Characterization of Conjugated Polymers Through Gel Permeation Chromatography and Static Light Scattering. *ACS Appl. Polym. Mater.* **2021**, *3* (9), 4572–4578. https://doi.org/10.1021/acsapm.1c00647.
(40) Gruendken, M.; Blume, A. Network Formation of Low Molecular Weight 'Liquid' Polymers Studied by Gel Permeation Chromatography and Stress-Strain Analysis According to Mooney-Rivlin. *Polym. Test.* **2023**, *118*, 107897. https://doi.org/10.1016/j.polymertesting.2022.107897.
(41) Schick, C. Differential Scanning Calorimetry (DSC) of Semicrystalline Polymers. *Anal. Bioanal. Chem.* **2009**, *395* (6), 1589. https://doi.org/10.1007/s00216-009-3169-y.
(42) Qian, Z.; Galuska, L.; McNutt, W. W.; Ocheje, M. U.; He, Y.; Cao, Z.; Zhang, S.; Xu, J.; Hong, K.; Goodman, R. B.; Rondeau-Gagné, S.; Mei, J.; Gu, X. Challenge and Solution of Characterizing Glass Transition Temperature for Conjugated Polymers by Differential Scanning Calorimetry. *J. Polym. Sci. Part B Polym. Phys.* **2019**, *57* (23), 1635–1644. https://doi.org/10.1002/polb.24889.
(43) Zhao, X.; Sun, P.; Zhao, K. The Relationship between the Concentration of Conjugated Polymer of an Aggregation Status and Absorbance of UV–Vis Absorption Spectra during the Aggregation Process of Conjugated Polymer Solutions. *Polym. Bull.* **2022**, *79* (10), 9159–9178. https://doi.org/10.1007/s00289-022-04314-y.
(44) Song, C. K.; Eckstein, B. J.; Tam, T. L. D.; Trahey, L.; Marks, T. J. Conjugated Polymer Energy Level Shifts in Lithium-Ion Battery Electrolytes. *ACS Appl. Mater. Interfaces* **2014**, *6* (21), 19347–19354. https://doi.org/10.1021/am505416m.
(45) Royakkers, J.; Guo, K.; Toolan, D. T. W.; Feng, L.-W.; Minotto, A.; Congrave, D. G.; Danowska, M.; Zeng, W.; Bond, A. D.; Al-Hashimi, M.; Marks, T. J.; Facchetti, A.;

Cacialli, F.; Bronstein, H. Molecular Encapsulation of Naphthalene Diimide (NDI) Based π-Conjugated Polymers: A Tool for Understanding Photoluminescence. *Angew. Chem. Int. Ed.* **2021**, *60* (47), 25005–25012. https://doi.org/10.1002/anie.202110139.
(46) Freychet, G.; Gann, E.; Zhernenkov, M.; McNeill, C. R. Anisotropic Resonant X-Ray Diffraction of a Conjugated Polymer at the Sulfur K-Edge. *J. Phys. Chem. Lett.* **2021**, *12* (15), 3762–3766. https://doi.org/10.1021/acs.jpclett.1c00532.
(47) Lee, Y.; Mongare, A.; Plant, A.; Ryu, D. Strain–Microstructure–Optoelectronic Inter-Relationship toward Engineering Mechano-Optoelectronic Conjugated Polymer Thin Films. *Polymers* **2021**, *13* (6), 935. https://doi.org/10.3390/polym13060935.
(48) Walther, F.; Heckl, W. M.; Stark, R. W. Evaluation of Nanoscale Roughness Measurements on a Plasma Treated SU-8 Polymer Surface by Atomic Force Microscopy. *Appl. Surf. Sci.* **2008**, *254* (22), 7290–7295. https://doi.org/10.1016/j.apsusc.2008.05.323.
(49) Stone, V. W.; Jonas, A. M.; Nysten, B.; Legras, R. Roughness of Free Surfaces of Bulk Amorphous Polymers as Studied by X-Ray Surface Scattering and Atomic Force Microscopy. *Phys. Rev. B* **1999**, *60* (8), 5883–5894. https://doi.org/10.1103/PhysRevB.60.5883.
(50) Atomic Force Microscopy. *Wikipedia*; 2022.
(51) He, K.; Li, X.; Liu, H.; Zhang, Z.; Kumar, P.; Ngai, J. H. L.; Wang, J.; Li, Y. D-A Polymer with a Donor Backbone - Acceptor-Side-Chain Structure for Organic Solar Cells. *Asian J. Org. Chem.* **2020**, *9* (9), 1301–1308. https://doi.org/10.1002/ajoc.202000172.
(52) Yuan, Y.; Kumar, P.; Ngai, J. H. L.; Gao, X.; Li, X.; Liu, H.; Wang, J.; Li, Y. Wide Bandgap Polymer Donor with Acrylate Side Chains for Non-Fullerene Acceptor-Based Organic Solar Cells. *Macromol. Rapid Commun.* **2022**, *43* (20), 2200325. https://doi.org/10.1002/marc.202200325.
(53) Jiang, Y.; Liu, H.; Li, X.; Yuan, Y.; Wang, J.; Cui, B.; Li, Y. Alkyloxime-Substituted Thiophene-Based Wide-Band-Gap Polymer Donor Achieving a High Short Circuit Current Density of 30 MA Cm–2 in Organic Solar Cells. *Chem. Mater.* **2022**, *34* (9), 4232–4241. https://doi.org/10.1021/acs.chemmater.2c00929.
(54) Liu, Y.; Lu, Y.; Ding, L.; Pan, C.-K.; Xu, Y.-C.; Wang, T.-Y.; Wang, J.-Y.; Pei, J. Fine-Tuning the Backbone Conformation of Conjugated Polymers and the Influence on Solution Aggregation and Optoelectronic Properties. *J. Polym. Sci.* **2023**. https://doi.org/10.1002/pol.20220634.
(55) Zhang, F.; Yao, Z.; Guo, Y.; Li, Y.; Bergstrand, J.; Brett, C. J.; Cai, B.; Hajian, A.; Guo, Y.; Yang, X.; Gardner, J. M.; Widengren, J.; Roth, S. V.; Kloo, L.; Sun, L. Polymeric, Cost-Effective, Dopant-Free Hole Transport Materials for Efficient and Stable Perovskite Solar Cells. *J. Am. Chem. Soc.* **2019**, *141* (50), 19700–19707. https://doi.org/10.1021/jacs.9b08424.
(56) Pammer, F.; Guo, F.; Lalancette, R. A.; Jäkle, F. Synthesis, Structures, and Hydroboration of Oligo- and Poly(3-Alkynylthiophene)s. *Macromolecules* **2012**, *45* (16), 6333–6343. https://doi.org/10.1021/ma3010718.
(57) Rydholm, A. E.; Held, N. L.; Bowman, C. N.; Anseth, K. S. Gel Permeation Chromatography Characterization of the Chain Length Distributions in Thiol-Acrylate Photopolymer Networks. *Macromolecules* **2006**, *39* (23), 7882–7888. https://doi.org/10.1021/ma060858u.
(58) Masarudin, M. J.; Cutts, S. M.; Evison, B. J.; Phillips, D. R.; Pigram, P. J. Factors Determining the Stability, Size Distribution, and Cellular Accumulation of Small,

Monodisperse Chitosan Nanoparticles as Candidate Vectors for Anticancer Drug Delivery: Application to the Passive Encapsulation of [14C]-Doxorubicin. *Nanotechnol. Sci. Appl.* **2015**, *8*, 67–80. https://doi.org/10.2147/NSA.S91785.

(59) Chiu, H.-C.; Tonks, I. A. Trimethylsilyl-Protected Alkynes as Selective Cross Coupling Partners in Ti-Catalyzed [2+2+1] Pyrrole Synthesis. *Angew. Chem. Int. Ed Engl.* **2018**, *57* (21), 6090–6094. https://doi.org/10.1002/anie.201800595.

(60) Yau, C. P.; Wang, S.; Treat, N. D.; Fei, Z.; Tremolet de Villers, B. J.; Chabinyc, M. L.; Heeney, M. Investigation of Radical and Cationic Cross-Linking in High-Efficiency, Low Band Gap Solar Cell Polymers. *Adv. Energy Mater.* **2015**, *5* (5), 1401228. https://doi.org/10.1002/aenm.201401228.

(61) Zeng, A.; Ma, X.; Pan, M.; Chen, Y.; Ma, R.; Zhao, H.; Zhang, J.; Kim, H. K.; Shang, A.; Luo, S.; Angunawela, I. C.; Chang, Y.; Qi, Z.; Sun, H.; Lai, J. Y. L.; Ade, H.; Ma, W.; Zhang, F.; Yan, H. A Chlorinated Donor Polymer Achieving High-Performance Organic Solar Cells with a Wide Range of Polymer Molecular Weight. *Adv. Funct. Mater.* **2021**, *31* (33), 2102413. https://doi.org/10.1002/adfm.202102413.

(62) Hoefler, S. F.; Rath, T.; Pastukhova, N.; Pavlica, E.; Scheunemann, D.; Wilken, S.; Kunert, B.; Resel, R.; Hobisch, M.; Xiao, S.; Bratina, G.; Trimmel, G. The Effect of Polymer Molecular Weight on the Performance of PTB7-Th:O-IDTBR Non-Fullerene Organic Solar Cells. *J. Mater. Chem. A* **2018**, *6* (20), 9506–9516. https://doi.org/10.1039/C8TA02467G.

(63) Tran, D. K.; Robitaille, A.; Hai, I. J.; Ding, X.; Kuzuhara, D.; Koganezawa, T.; Chiu, Y.-C.; Leclerc, M.; Jenekhe, S. A. Elucidating the Impact of Molecular Weight on Morphology, Charge Transport, Photophysics and Performance of All-Polymer Solar Cells. *J. Mater. Chem. A* **2020**, *8* (40), 21070–21083. https://doi.org/10.1039/D0TA08195G.

(64) Kang, H.; Uddin, M. A.; Lee, C.; Kim, K.-H.; Nguyen, T. L.; Lee, W.; Li, Y.; Wang, C.; Woo, H. Y.; Kim, B. J. Determining the Role of Polymer Molecular Weight for High-Performance All-Polymer Solar Cells: Its Effect on Polymer Aggregation and Phase Separation. *J. Am. Chem. Soc.* **2015**, *137* (6), 2359–2365. https://doi.org/10.1021/ja5123182.

(65) Qi, B.; Wang, J. Open-Circuit Voltage in Organic Solar Cells. *J. Mater. Chem.* **2012**, *22* (46), 24315–24325. https://doi.org/10.1039/C2JM33719C.

(66) Le Corre, V. M.; Duijnstee, E. A.; El Tambouli, O.; Ball, J. M.; Snaith, H. J.; Lim, J.; Koster, L. J. A. Revealing Charge Carrier Mobility and Defect Densities in Metal Halide Perovskites via Space-Charge-Limited Current Measurements. *ACS Energy Lett.* **2021**, *6* (3), 1087–1094. https://doi.org/10.1021/acsenergylett.0c02599.

(67) Shekar, S.; Subramanian, S.; Ramamurthy, P. C. Design and Fabrication of a Solid-State Chemiresistive Sensor for the Detection of Hexavalent Chromium. In *2022 IEEE International Conference on Flexible and Printable Sensors and Systems (FLEPS)*; 2022; pp 1–4. https://doi.org/10.1109/FLEPS53764.2022.9781516.

(68) Onge, P. B. J. S.; Chen, T.-C.; Langlois, A.; Younus, A.; Hai, I. J.; Lin, B.-H.; Chiu, Y.-C.; Rondeau-Gagné, S. Iron-Coordinating π-Conjugated Semiconducting Polymer: Morphology and Charge Transport in Organic Field-Effect Transistors. *J. Mater. Chem. C* **2020**, *8* (24), 8213–8223. https://doi.org/10.1039/D0TC01536A.

(69) Yuan, Y.; Michinobu, T. Energy Level Tuning of Polythiophene Derivative by Click Chemistry-Type Postfunctionalization of Side-Chain Alkynes. *J. Polym. Sci. Part Polym. Chem.* **2011**, *49* (1), 225–233. https://doi.org/10.1002/pola.24443.

(70) Dubost, E.; Fossey, C.; Cailly, T.; Rault, S.; Fabis, F. Selective Ortho-Bromination of Substituted Benzaldoximes Using Pd-Catalyzed C–H Activation: Application to the Synthesis of Substituted 2-Bromobenzaldehydes. *J. Org. Chem.* **2011**, *76* (15), 6414–6420. https://doi.org/10.1021/jo200853j.
(71) Kolb, H. C.; Finn, M. G.; Sharpless, K. B. Click Chemistry: Diverse Chemical Function from a Few Good Reactions. *Angew. Chem. Int. Ed.* **2001**, *40* (11), 2004–2021. https://doi.org/10.1002/1521-3773(20010601)40:11<2004::AID-ANIE2004>3.0.CO;2-5.
(72) Michinobu, T. Click Functionalization of Aromatic Polymers for Organic Electronic Device Applications. *Macromol. Chem. Phys.* **2015**, *216* (13), 1387–1395. https://doi.org/10.1002/macp.201500086.
(73) Schulze, B.; Brown, D. G.; Robson, K. C. D.; Friebe, C.; Jäger, M.; Birckner, E.; Berlinguette, C. P.; Schubert, U. S. Cyclometalated Ruthenium(II) Complexes Featuring Tridentate Click-Derived Ligands for Dye-Sensitized Solar Cell Applications. *Chem. – Eur. J.* **2013**, *19* (42), 14171–14180. https://doi.org/10.1002/chem.201301440.
(74) Park, J. S.; Kim, Y. H.; Song, M.; Kim, C.-H.; Karim, Md. A.; Lee, J. W.; Gal, Y.-S.; Kumar, P.; Kang, S.-W.; Jin, S.-H. Synthesis and Photovoltaic Properties of Side-Chain Liquid-Crystal Click Polymers for Dye-Sensitized Solar-Cells Application. *Macromol. Chem. Phys.* **2010**, *211* (23), 2464–2473. https://doi.org/10.1002/macp.201000264.
(75) Ngai, J. H. L.; Polena, J.; Afzal, D.; Gao, X.; Kapadia, M.; Li, Y. Green Solvent-Processed Hemi-Isoindigo Polymers for Stable Temperature Sensors. *Adv. Funct. Mater.* **2022**, *32* (17), 2110995. https://doi.org/10.1002/adfm.202110995.
(76) Hui, R.; Zhao, M.; Chen, M.; Ren, Z.; Guan, Z. One-Pot Synthesis of 4-Aryl-NH-1,2,3-Triazoles through Three-Component Reaction of Aldehydes, Nitroalkanes and NaN3. *Chin. J. Chem.* **2017**, *35* (12), 1808–1812. https://doi.org/10.1002/cjoc.201700367.
(77) Boelke, A.; Lork, E.; Nachtsheim, B. J. N-Heterocycle-Stabilized Iodanes: From Structure to Reactivity. *Chem. – Eur. J.* **2018**, *24* (70), 18653–18657. https://doi.org/10.1002/chem.201804957.
(78) Wang, G.; Kumar, P.; Zhang, Z.; Hendsbee, A. D.; Liu, H.; Li, X.; Wang, J.; Li, Y. Facile Synthesis of a Semiconducting Bithiophene-Azine Polymer and Its Application for Organic Thin Film Transistors and Organic Photovoltaics. *RSC Adv.* **2020**, *10* (22), 12876–12882. https://doi.org/10.1039/D0RA01211D.
(79) Qiu, D.; Adil, M. A.; Lu, K.; Wei, Z. The Crystallinity Control of Polymer Donor Materials for High-Performance Organic Solar Cells. *Front. Chem.* **2020**, *8*.
(80) Jeffrey, G. A. *An Introduction to Hydrogen Bonding*; Oxford University Press, 1998.
(81) Katsouras, A.; Gasparini, N.; Koulogiannis, C.; Spanos, M.; Ameri, T.; Brabec, C. J.; Chochos, C. L.; Avgeropoulos, A. Systematic Analysis of Polymer Molecular Weight Influence on the Organic Photovoltaic Performance. *Macromol. Rapid Commun.* **2015**, *36* (20), 1778–1797. https://doi.org/10.1002/marc.201500398.
(82) Ding, Z.; Kettle, J.; Horie, M.; W. Chang, S.; C. Smith, G.; I. Shames, A.; A. Katz, E. Efficient Solar Cells Are More Stable: The Impact of Polymer Molecular Weight on Performance of Organic Photovoltaics. *J. Mater. Chem. A* **2016**, *4* (19), 7274–7280. https://doi.org/10.1039/C6TA00721J.
(83) Li, S.; Zhan, L.; Sun, C.; Zhu, H.; Zhou, G.; Yang, W.; Shi, M.; Li, C.-Z.; Hou, J.; Li, Y.; Chen, H. Highly Efficient Fullerene-Free Organic Solar Cells Operate at Near Zero Highest Occupied Molecular Orbital Offsets. *J. Am. Chem. Soc.* **2019**, *141* (7), 3073–3082. https://doi.org/10.1021/jacs.8b12126.

(84) Chen, S.; Wang, Y.; Zhang, L.; Zhao, J.; Chen, Y.; Zhu, D.; Yao, H.; Zhang, G.; Ma, W.; Friend, R. H.; Chow, P. C. Y.; Gao, F.; Yan, H. Efficient Nonfullerene Organic Solar Cells with Small Driving Forces for Both Hole and Electron Transfer. *Adv. Mater.* **2018**, *30* (45), 1804215. https://doi.org/10.1002/adma.201804215.
(85) Elumalai, N. K.; Uddin, A. Open Circuit Voltage of Organic Solar Cells: An in-Depth Review. *Energy Environ. Sci.* **2016**, *9* (2), 391–410. https://doi.org/10.1039/C5EE02871J.
(86) Iyobe, A.; Uchida, M.; Kamata, K.; Hotei, Y.; Kusama, H.; Harada, H. ChemInform Abstract: Studies on New Platelet Aggregation Inhibitors. Part 1. Synthesis of 7-Nitro-3,4-Dihydroquinoline-2(1H)-One Derivatives. *ChemInform* **2001**, *32* (52). https://doi.org/10.1002/chin.200152137.